

Electric Field Effects on Alignment of Lamellar Structures in Diblock Copolymer Thin Films Studied by Neutron Scattering

DISSERTATION

zur Erlangung des akademischen Grades

doctor rerum naturalium
(Dr. rer. nat.)
genehmigt durch

die Naturwissenschaftliche Fakultät II
Institut für Physik
der Martin-Luther-Universität
Halle-Wittenberg

vorgelegt von
Frau M. Sc. Xiuli Jiang
geboren am 15.05.1977 in Jilin, China

Gutachterin / Gutachter:

1. Prof. Dr. Thomas Thurn-Albrecht
2. Prof. Dr. Bernd Stühn
3. Prof. Dr. Christine M. Papadakis

Halle (Saale), Oktober 2006

Verteidigungsdatum: 07.12.2006

urn:nbn:de:gbv:3-000011227

[<http://nbn-resolving.de/urn/resolver.pl?urn=nbn%3Ade%3Agbv%3A3-000011227>]

Abstract

We investigated the lamellar orientation in thin films of a diblock copolymer P(S-b-MMA), under competing effects of surface interactions and an electric field applied perpendicular to the substrate. The surface effects tend to align the lamellae parallel to the substrate while the electric field tends to align the lamellae perpendicular to the substrate. Using neutron reflectivity, neutron diffuse scattering, and neutron small-angle scattering, we achieved a quantitative analysis of the internal structure of the films. Film thickness was found to play a non-trivial role in determining the structure of the films. A complete alignment by the surface effects was observed in the thinner films by annealing. The parallel orientation remains stable even if an electric field as strong as $40 \text{ V}/\mu\text{m}$ is applied. In the thicker films, a mixed orientation with boundary layers parallel and the central part partially perpendicular to the substrate was observed after annealing. The mixed orientation becomes unstable under a small compressive stress, and will be converted into a completely parallel orientation. The parallel orientation induced by the compressive stress remains stable as long as the electric field is weaker than several ten $\text{V}/\mu\text{m}$. Only a field of about $40 \text{ V}/\mu\text{m}$ is able to stabilize the above mentioned mixed orientation. A fully perpendicular orientation was never observed in our experiments. Diffuse scattering shows a mosaic structure in the absence of an electric field, whose mosaicity will be increased by the torque exerted by an electric field. The lateral correlation length of the lamellar domains is estimated as $1\text{-}2 \mu\text{m}$. Limited by the small q_x -range we have used, a clear statement on the existence of the electric-field-induced structural undulations predicted by the Onuki's theory cannot be made from our experiments.

Kurzfassung

Wir untersuchten die Orientierung von Lamellen in dünnen Filmen eines P(S-b-MMA)-Copolymers unter dem Einfluss von Oberfläche und senkrecht zur Oberfläche angelegtem elektrischen Feld. Die Oberfläche richtet die Lamellen parallel zur Oberfläche aus, während das elektrische Feld die Lamellen senkrecht zur Oberfläche ausrichtet. Mit Neutronenreflektometrie, diffuser Neutronenstreuung, und Neutronenkleinwinkelstreuung wurde die Struktur der Filme quantitativ analysiert. Die Filmdicke hat einen grossen Einfluss auf die Struktur der Filme. Nach dem Tempern wird eine komplette Orientierung durch die Oberfläche in den dünnen Filmen beobachtet. Die parallele Orientierung bleibt auch dann stabil wenn ein elektrisches Feld mit ungefähr $40 \text{ V}/\mu\text{m}$ angelegt wird. In den dickeren Filmen wird eine uneinheitliche Orientierung nach dem Tempern beobachtet. Die Lamellen in den Grenzflächen richten sich parallel zur Oberfläche aus und die in der Mitte gelegenen senkrecht zur Oberfläche. Die uneinheitliche Orientierung wird durch Druck instabil und die Lamellen orientieren sich komplett parallel. Die durch Druck verursachte parallele Ausrichtung bleibt stabil solange das angelegte elektrische Feld schwächer als einige zehn $\text{V}/\mu\text{m}$ ist. Nur ein Feld von ungefähr $40 \text{ V}/\mu\text{m}$ kann die uneinheitliche Orientierung stabilisieren. Eine vollständige senkrechte Orientierung wurde in unseren Experimenten nie beobachtet. Diffuse Neutronenstreuung zeigt eine mosaikartige Struktur ohne elektrisches Feld, wobei der Grad der Mosaikartigkeit durch das Drehmoment aufgrund des elektrischen Feldes steigt. Die laterale Korrelationslänge der lamellaren Domänen wird auf $1\text{-}2 \mu\text{m}$ geschätzt. Der begrenzte q_x -Bereich lässt keine klare Aussage über die Existenz der durch ein elektrisches Feld induzierten strukturellen Schwankungen, die durch die Theorie von Onuki vorhergesagt werden, zu.

Contents

1	Introduction	1
2	Block copolymers	4
2.1	Microphase separation	5
2.2	Surface segregation	7
2.3	Electric-field-induced alignment	9
2.4	Electric-field-induced structural undulations	12
2.5	Competing effects	14
3	Neutron scattering	16
3.1	Basic concepts	16
3.2	Scattering from sharp interfaces	19
3.2.1	Snell's law	19
3.2.2	Reflectivity from a single interface	20
3.2.3	Reflectivity from two parallel interfaces	21
3.2.4	Reflectivity from multiple interfaces	23
3.3	Scattering from rough interfaces	26
3.3.1	Scattering from a single rough interface	26
3.3.2	Characterization of surface roughness	27
3.3.3	Types of correlation function	28
3.3.4	Scattering from multiple rough interfaces	29
3.3.5	Effect of slit collimation	32
3.4	Small-angle scattering	35
3.4.1	Ewald sphere and reciprocal space	35
3.4.2	Determination of scattering patterns	36
4	Sample preparation	39
4.1	Spin-coating	40
4.2	Thickness measurements	41
4.3	First annealing	42
4.4	Second annealing	44
5	Instruments	47
5.1	Time-of-flight reflectometer AMOR	47
5.1.1	Chopper	50
5.1.2	Frame overlap	51
5.1.3	Time offset	53
5.1.4	Normalization	55
5.1.5	Resolution	56
5.1.6	Refraction effect	59

5.2	Monochromatic reflectometer MORPHEUS	66
5.3	Small-angle scattering SANS-II	67
6	Lamellar orientation under competing external fields	69
6.1	Reflectivity	70
6.1.1	Pure silicon wafer	70
6.1.2	Parameters used in Parratt32	71
6.1.3	Effects of first annealing, upper electrode and compressive stress	72
6.1.4	Average scattering length density and partial mixing	77
6.1.5	Effects of electric fields	79
6.2	Small-angle scattering	83
6.3	Test measurements on MORPHEUS	89
6.4	Discussion	90
6.4.1	Mixed orientation	90
6.4.2	Parallel orientation	91
6.4.3	Alignment by the electric field	94
6.4.4	Effect of the film thickness	95
7	Diffuse scattering	96
7.1	Mosaicity and thermal fluctuations	96
7.2	Correlation length and power law exponent	102
7.3	Structural undulations	105
8	Conclusion	108

Chapter 1

Introduction

Block copolymers are the focus of a great deal of research activity in contemporary macromolecular science, for they are pre-eminent self-assembling materials which can be used in manufacturing particular nanostructures. The importance and advantage for studying the properties of systems consisting of block copolymers stand on the following five characters of block copolymers [1]:

- Precise control over length scale;
- Control over morphology;
- Control over domain functionality and properties;
- Quantitative prediction of equilibrium structures;
- Retention of the traditional advantages of polymeric materials.

Particularly, they show a rich variety of microphase separated equilibrium bulk morphologies (spheres, cylinders, bi-continuous double diamonds, lamellae) depending on the volume fraction of the block components. It is of great interest to control the ordering and orientation of block copolymer microdomains with these morphologies by means of external fields due to their potential use in lithography [2], nanoscale templates [3] and nanoscale manufacturing [4]. Electric fields turned out to be an especially effective tool in this context. The electric-field-induced alignment was observed and studied in bulk lamellar system [5, 6, 7, 8], films with cylindrical structures [9, 10, 11], films with lamellar structures [12, 13, 14, 15, 16], and concentrated solutions with lamellar structures [17, 18, 19, 20, 21].

Many of the previous publications dealt with the microscopic mechanisms of electric-field-induced alignment of block copolymer microdomains. Amundson and Helfand et al. [5] suggested two alignment mechanisms for bulk samples of a lamellar polystyrene-polymethylmethacrylate (PS-PMMA) diblock copolymer cooled down from a disordered state under an external electric field. They argued a nucleation center grows and re-orientates by rotation of an ordered region as a whole once its radius reaches a minimal size (~ 150 nm), or nucleation centers coalesce to form a polydomain structure with no macroscopic orientation. In the latter case, subsequent alignment would occur by movement of grain boundaries such that regions of favorable orientation grow at the expense of neighboring regions. Böker et al. [18, 19] and Zvelindovsky et al. [22] reported similar mechanisms for concentrated toluene solutions of a lamellar polystyrene-polyisoprene (PS-PI) diblock copolymer, both experimentally and by computer simulations (based on dynamic density functional theory). In addition, both the mechanism of alignment

and the kinetics of the process were found [21] strongly dependent on the initial degree of order in the system. In a highly ordered system with lamellae aligned perpendicular to the electric field, only the grain boundary migration mechanism is possible as a pathway to reorientation and the process proceeds rather slowly. In a less ordered system, grain rotation becomes possible as an alternative pathway, and the process proceeds considerably faster.

The situation of block copolymer films confined in between a free surface and a solid substrate might be different from the cases of bulk systems or concentrated solutions, due to the strong surface interactions taking part in the alignment process. The effects of surface interactions are in competition with the effects of an electric field applied perpendicular to the film substrate, in the sense that the surface interactions and the electric field favor different orientations of the microdomains. While the surface interactions (preferential wetting) tend to align the microdomains parallel to the substrate, the electric field tends to align the microdomains parallel to the field, i.e., perpendicular to the substrate. As in the cases of bulk systems, the microdomains which are aligned initially parallel to the substrate by the surface effects can be reoriented perpendicular to the substrate by a perpendicularly applied electric field. Although the mechanism of this reorientation process is not yet clearly known, it was believed that the electric field induces structural undulations which lead to a disruption of the original structure and facilitate the alignment to set in. Xu et al. [11] observed a disruption of the cylinders in thin films of asymmetric PS-PMMA diblock copolymers using 3D TEM (three-dimensional transmission electron microscopy). The cylinders were disrupted into ellipsoid-shaped microdomains with a wavelength comparable to the center-to-center distance between the cylinders, and connected into cylindrical microdomains oriented in the field direction. DeRouchey et al. [12] also reported an intermediate state with substantially reduced long-range order of the lamellae in films of a symmetric PS-PI diblock copolymer. Thurn-Albrecht et al. investigated the electric-field-induced alignment in films of asymmetric PS-PMMA diblock copolymers. Starting from a disordered state, they observed [9] a full alignment by the electric field if the applied field overwhelms a threshold field strength E_t . The threshold field strength was found independent of the film thickness for films of about 10-30 μm thick, and was shown to be determined by the difference in interfacial energies of the components. Starting from a microphase-separated state, they observed [10] domains with both parallel and perpendicular orientations to the surfaces. But the parallel orientation was not important since their films were thick. Recently, Xu et al. [11] investigated the electric-field-induced alignment of the cylinders in thin films of asymmetric PS-PMMA diblock copolymers. Their results were consistent with those obtained from the thick films, showing that starting from an ordered state a field of about 40 V/ μm was not able to induce a full alignment of the cylinders parallel to the field. For block copolymer thin films with lamellar microdomains, a complete alignment of the lamellae by an electric field can only be achieved [13] if the interfacial interactions are balanced by modifying [23] the substrate with random copolymer brushes. If the effects of surface interactions are relatively strong, the effects of electric fields have to be enlarged in order to achieve a complete alignment by the electric field. The electric fields effects were found [16] to be significantly enhanced by adding lithium chloride (LiCl) into a lamellar PS-PMMA diblock copolymer.

In our study, we investigated the lamellar orientation in thin films of a symmetric PS-PMMA diblock copolymer, under competing effects of surface interactions and an electric field applied perpendicular to the film substrate. The thicknesses of the films are below 1 μm , i.e., 0.26 μm and 0.86 μm , respectively, corresponding to about 8 and

27 lamellar periods with the period d_p determined from the experiments as 32 nm. The lamellar orientation in the films is then the result of competition between surface effects and electric field effects. Since the surface effects are typically limited within several layers [15] and become less important away from the surfaces, we would expect different orientation behaviors in the films with different thicknesses. In order to achieve a quantitative analysis of the internal structure of the films, neutron reflectivity, neutron diffuse scattering and neutron small-angle scattering methods were employed. The neutron scattering technique (as well as x-ray scattering) has proved to be a marvelous non-destructive probe for the study of structure and morphology of thin films and interfaces. In our experiments, neutron reflectivity and neutron small-angle scattering are complementary to each other. While reflectivity is sensitive to lamellae aligned parallel to the substrate, small-angle scattering in transmission is sensitive to lamellae aligned perpendicular to the substrate. Measurements at different angles of incidence allow the determination of orientation distribution of the lamellae. Longitudinal diffuse scattering near the specular reflection provide us information about the lateral structure of lamellae oriented parallel to the substrate. The neutron scattering experiments were performed at the spallation neutron source of the Paul-Scherrer-Institute. Reflectivity and diffuse scattering were measured by the time-of-flight reflectometer AMOR. Small-angle scattering was measured by the instrument SANS-II. It should be mentioned that the time-of-flight mode was newly established on the reflectometer AMOR in the beginning of our study. Much efforts have been done to optimize the instrumental settings and to achieve a better understanding of the new mode, the details of which will be shown in chapter 5.

The organization of this thesis is as follows. In chapter 2, a basic knowledge about block copolymers including the microphase separation during which microphase separated structures are formed, the surface-induced alignment and the electric-field-induced alignment of these microphase separated structures, will be introduced. In chapter 3, a theoretical background of the neutron scattering technique will be given. The reflectivity and diffuse scattering functions will be calculated theoretically for different model systems. It will be shown how to determine the small-angle scattering patterns with the help of the concepts of Ewald sphere and reciprocal lattice. In chapters 4 and 5, the experimental parts including the sample preparation and the instruments will be described. In chapter 6, the combined results of reflectivity and small-angle scattering will be shown and discussed. In chapter 7, the results of diffuse scattering will be shown and discussed. Finally, the conclusion remarks will be given in chapter 8.

Chapter 2

Block copolymers

In this thesis, the lamellar orientation in thin films of a symmetric diblock copolymer polystyrene-polymethylmethacrylate P(S-b-MMA) under competing effects of surface interactions and an electric field applied perpendicular to the surfaces will be studied. First of all, a basic knowledge about block copolymers should be introduced. A polymer (also called macromolecule) is a very long molecule consisting of repeating structural units (called monomer) connected by covalent chemical bonds. The repeating units of a polymer can be identical, as in the case of a homopolymer, or have distinct chemical constituents, as in the case of a copolymer. A block copolymer is a copolymer consisting of two or more homogeneous sequences in one molecule. According to the number of sequences, a block copolymer is called di-, tri- or multi- block copolymer (Fig. 2.1). The most characteristic feature of a block copolymer is the strong repulsion between unlike sequences even if the repulsion between unlike monomers is relatively weak [24]. As a result the sequences tend to segregate, but as they are chemically bonded even the complete segregation cannot lead to a macroscopic phase separation as in a polymer blend (a mixture of two or more homopolymers). Instead, a microphase separation occurs on the level of molecular dimensions (radius of gyration). Ordered structures such as spheres, cylinders, bi-continuous double diamonds and lamellae are formed during the microphase separation of a block copolymer depending on the volume fraction of the block components. In thin films of block copolymers, these ordered microdomains can be aligned parallel to the film substrate by the effects of surface interactions. They can also be aligned by an external electric field to be parallel to the field where the surface effects are not dominant. An interesting situation arises if an electric field is applied perpendicular to the substrate, in which the alignment by the surface effects is in competition with the alignment by the electric field. This is exactly the case we will investigate in this study.



Figure 2.1: Schematic drawings of (a) a homopolymer; (b) an AB di- block copolymer; and (c) an ABA tri- block copolymer. The lighter and darker colors indicate different species of monomers A and B, respectively.

2.1 Microphase separation

In this section, the theory of microphase separation of block copolymers will be introduced, in comparison with that for a simpler case, a polymer blend. The phase behavior of a polymer blend can be described by the Flory-Huggins lattice theory. Here we consider a mixture of polymers A and B with a polymerization index N_A and N_B , respectively. The volume fraction of component A in the blend is ϕ . The free energy of mixing is given by

$$\frac{\Delta F_{mix}}{k_B T} = \frac{1}{N_A} \phi \ln \phi + \frac{1}{N_B} (1 - \phi) \ln(1 - \phi) + \chi \phi (1 - \phi) \quad (2.1)$$

where k_B is the Boltzmann constant, T is the absolute temperature and χ is the Flory-Huggins interaction parameter characterizing the effective interaction of monomers A and B. Fig. 2.2 shows a typical phase diagram calculated from the Flory-Huggins theory for a symmetric system ($N_A = N_B = N$). The binodal line is the phase equilibrium line

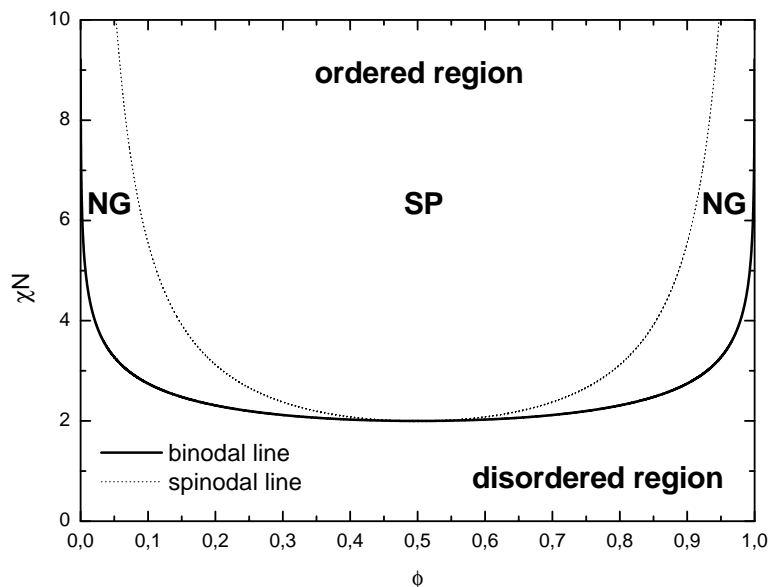


Figure 2.2: Typical phase diagram calculated from the Flory-Huggins lattice theory for a symmetric polymer blend ($N_A = N_B = N$). The critical point occurs at $\phi_c = 0.5$, $(\chi N)_c = 2$.

separating the disordered and ordered regions in the phase diagram. The spinodal line separates the ordered region into the meta-stable region and the unstable region. In the meta-stable region, the phase separation proceeds via the nucleation and growth (NG) mechanism. In the unstable region, the phase separation proceeds via the spinodal decomposition (SD) mechanism.

The Flory-Huggins theory is unsuitable to study the microphase separation of a block copolymer. In this context, Bates and Fredrickson [25] have given a representative review of the experimental and theoretical developments in block copolymer thermodynamics. In the strong segregation limit, the experimental results show the various phase equilibrium morphologies, depicted in Fig. 2.3 depending on the volume fraction of the block components. Most of these equilibrium morphologies (spherical, cylindrical and lamellar morphologies) are in close agreement with theoretical predictions [26], based on the self-consistent-field theory proposed by Helfand [28]. In order to investigate the order-disorder transition (ODT), Leibler [24] constructed a Landau expansion of the

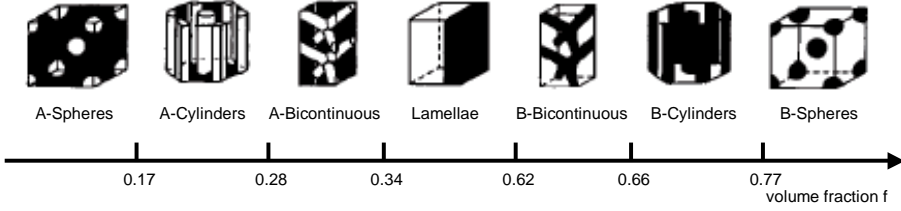


Figure 2.3: Equilibrium morphologies for an AB diblock copolymer in the strong segregation limit, where f is the volume fraction of the component A. Figure taken from [25].

free energy to the fourth order of a compositional order parameter. By using a random phase approximation [29], Leibler was able to locate the microphase separation transition (MST), at which a homogeneous block copolymer melt first orders. For the sake of simplicity, he considered an AB diblock copolymer with all the chains having the same index of polymerization $N = N_A + N_B$ (N_A and N_B denote the number of monomers of type A and B, respectively) and the same composition $f = N_A/N$. In the Leibler's mean-field theory, only two quantities turned out to be relevant parameters for the characterization of phase equilibria in a block copolymer melt: the composition f and the product χN . The phase diagram calculated from the Leibler's theory is shown in Fig. 2.4. A qualitative prediction can be made from this phase diagram for a fixed

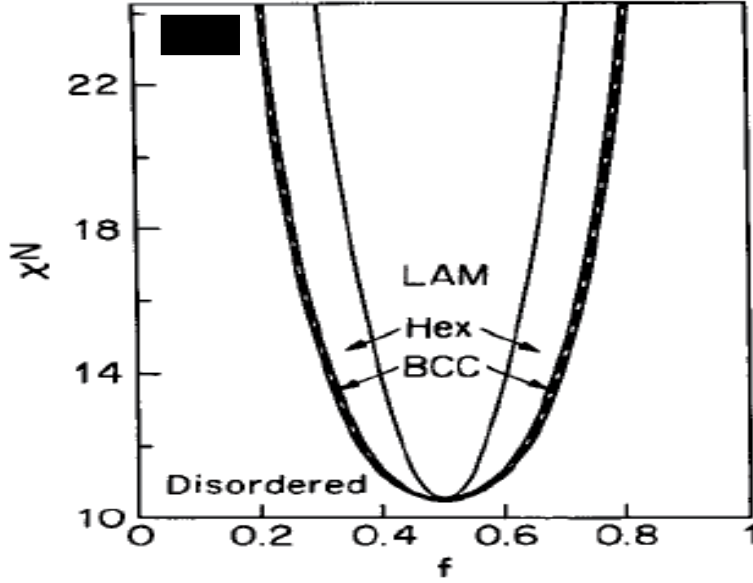


Figure 2.4: Phase diagram calculated from the Leibler's mean-field theory for a diblock copolymer with all the chains having the same index of polymerization $N = N_A + N_B$ and the same composition $f = N_A/N$. The critical point occurs at $f_c = 0.5$, $(\chi N)_c = 10.495$. Figure taken from [25].

χN . The phase diagram shows that by increasing f one should observe, respectively, a body-centered-cubic (BCC), a hexagonal (HEX), a lamellar (LAM), an inverted HEX, and an inverted BCC microphase structure. This prediction is in agreement with the experimental results as schematically shown in Fig. 2.3.

For our sample of P(S-b-MMA) with a symmetric volume fraction $f = 0.5$, ordered lamellar structures will be formed during the microphase separation. Ordered lamellae can be achieved by annealing the sample at a temperature below the order-disorder transition temperature (T_{ODT}). A polymer, which is viscoelastic in nature, presents properties like a glass or a rubber depending on the temperature. The transition tem-

perature between the glassy state and the rubber state is defined as the glass transition temperature T_g . Below the glass transition temperature, the polymer presents a glassy state and the molecules or the segments (usually consisted of several monomers) of the polymer are kinetically frozen. In this state, the molecules of block copolymers cannot self-assemble into various morphologies due to the very low mobility of the chains. Therefore, the annealing temperature is necessary to be well above the T_g s of the block components, in order to achieve ordered microphase structures in the sample.

2.2 Surface segregation

In thin films of block copolymers, ordered microphase structures (e.g., lamellae) formed during the microphase separation of the copolymer can be aligned by the confining surfaces of the film. The films can be confined in between two solid surfaces, or a free surface (e.g., air) and a solid substrate (e.g., silicon). Because of the chemically distinct nature of each block, the different interactions of each block at a surface give rise to a preferential segregation of one block to the surface [30]. The enrichment of one block component at the surface induces a parallel orientation of the lamellae, and this parallel orientation propagates into the middle of the film. In most cases, both confining surfaces have preferential wetting effects, and a parallel orientation will be induced [(Fig. 2.5 (a))]. If both confining surfaces are non-preferential (or neutral) to

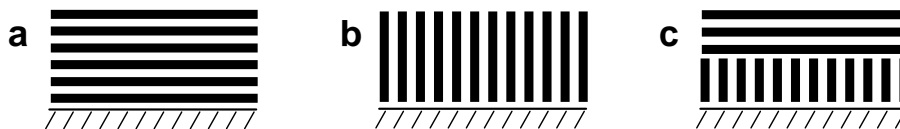


Figure 2.5: Orientation of the lamellae in a thin film of symmetric diblock copolymers confined in between a free surface (e.g., air) and a solid substrate (e.g., silicon). A parallel, a perpendicular and a mixed orientation of the lamellae will be induced in cases of (a) two wetting surfaces, (b) two neutral surfaces and (c) a wetting free surface and a neutral substrate. The black and white regions in the film denote the two blocks of the copolymer, respectively.

the block components, a perpendicular orientation of the lamellae will be induced [(Fig. 2.5 (b))]. If the confining surfaces prefer different orientations, e.g., a wetting air surface and a neutral substrate coexist, a mixed orientation with parallel lamellae at the air surface and perpendicular lamellae at the neutral substrate will be induced [(Fig. 2.5 (c))].

As the surface effects become less and less dominant away from the surfaces [15], a parallel orientation throughout the film [shown in 2.5 (a)] can only be achieved if the film is thin enough. In this case, the total film thickness depends on whether symmetric or antisymmetric wetting effects occur at the surfaces. In a symmetric wetting case [Fig. 2.6 (a)], component A (depicted in the lighter color) tends to segregate to both surfaces, forming a layer A of thickness $d_p/4$ at each surface. The film thickness is therefore equal to integer of the lamellar period d_p of the copolymer. In an antisymmetric wetting case [Fig. 2.6 (b)], component A tends to segregate to the free surface while component B tends to segregate to the solid substrate, forming a layer A or layer B of thickness $d_p/4$ at the corresponding surface. The film thickness is therefore equal to half-integer of the lamellar period d_p of the copolymer. Commensurability of the film thickness with the lamellar period also plays a central role in the film structure. Films having

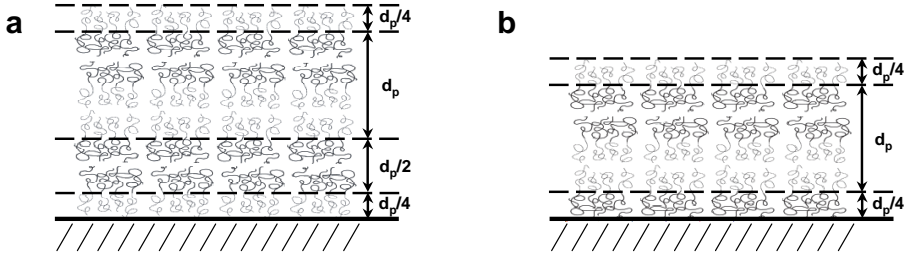


Figure 2.6: Symmetric (a) and antisymmetric (b) wetting effects in a film with a parallel orientation of the lamellae throughout the film. The film thickness corresponds to integer or half-integer of the lamellar period (denoted as d_p) for the symmetric and antisymmetric wetting cases, respectively. The lighter and darker color indicate block components A and B of the copolymer, respectively.

thicknesses that are incommensurate with the lamellar period undergo quantization of the film thickness to discrete integer or half-integer values of the lamellar period for symmetric and antisymmetric wetting cases, respectively [31]. The quantization of the film thickness results in the generation of terraces or islands and holes structures at the free surface. Fig. 2.7 (a) and (b) show the atomic force microscopy (AFM) images of such islands and holes structures observed by Papadakis et al. [32]. These islands and holes structures are in turn, an evidence for a parallel orientation throughout the film. This is because in a fully or partially perpendicularly oriented structure [as shown in 2.5 (b) and (c)], the incommensurability of the film thickness with the lamellar period can be accommodated by either increasing or decreasing the thickness of the region with perpendicular orientation, and the lamellar period can be maintained without the formation of islands and holes. Fig. 2.7 (c) and (d) show the surface structures with a perpendicular orientation of the lamellae. Note that the orientation of the lamellae in the plane of the film is however random.

The effects of surface interactions can be quantitatively described by the difference in surface energies of the components. The contribution to the free energy over an area A due to surface interactions is given by [9]

$$F_{surf} = \int_A \sigma(\parallel, \perp) dA \quad (2.2)$$

where $\sigma(\parallel, \perp)$ is the surface energy for parallel and perpendicular orientations, respectively. A full alignment by a perpendicularly applied electric field can occur only if the effects of the electric field overcomes those of surface interactions. Therefore a fully perpendicular orientation will occur either in a system with weak surface interactions or with a strong electric field. For our system of P(S-b-MMA), the surface energies of PS and PMMA were reported [33] as 40.7 dyn/cm (or 40.7×10^{-3} J/m²) and 41.1 dyn/cm (or 41.1×10^{-3} J/m²) at 20 °C, respectively. The difference in surface energies of the two components drives the PS block to segregate to the air surface. On the substrate side, where we used polished silicon wafers as substrate, the PMMA segregates preferentially due to the favorable interactions between PMMA and the native SiO₂ layer formed on the substrate. Because both confining surfaces have preferential wetting effects, the surface effects might be relatively strong in this system. The threshold field E_t above which a fully perpendicular orientation will be induced is beyond our observations, even if a field as strong as ~ 40 V/ μ m is applied.

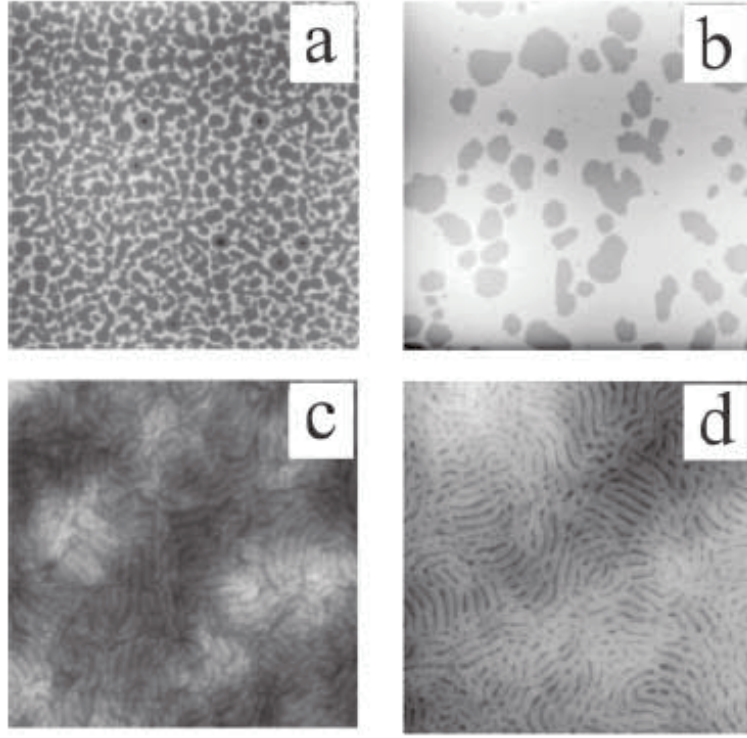


Figure 2.7: AFM images of surface morphologies of thin films of symmetric diblock copolymers P(S-b-B), taken from [32]. The sizes of the pictures are: (a) $50 \times 50 \mu\text{m}^2$; (b) $100 \times 100 \mu\text{m}^2$; (c) $3 \times 3 \mu\text{m}^2$; (d) $3 \times 3 \mu\text{m}^2$.

2.3 Electric-field-induced alignment

As mentioned in the introduction of the thesis, the electric-field-induced alignment of ordered microdomains in block copolymers were observed in bulk, thin films and concentrated solutions for both cylindrical and lamellar microphase structures. The driving force for the alignment is the orientation dependent polarization in a material having domains that are anisotropic in shape.

Consider a single lamellar domain with a dielectric constant ε placed in an external electric field \mathbf{E}_0 (Fig. 2.8), the polarization \mathbf{P} which is given by

$$\mathbf{P} = \varepsilon_0 \chi \mathbf{E} = \varepsilon_0 (\varepsilon - 1) \mathbf{E} \quad (2.3)$$

will be orientation dependent. The constant $\varepsilon_0 = 8.8542 \times 10^{-12} \text{C}^2 \cdot \text{N}^{-1} \cdot \text{m}^{-2}$ is the permittivity of vacuum or the absolute permittivity. The difference in polarization between the lamella and the surroundings will induce charges on the surface of the lamella, which give rise to a depolarization field \mathbf{E}_P superposed on the external field \mathbf{E}_0 . The total electric field \mathbf{E} is given by

$$\mathbf{E} = \mathbf{E}_0 + \mathbf{E}_P \quad (2.4)$$

The depolarization field \mathbf{E}_P is also orientation dependent. Let P_z and P_x (or P_y) be the components of the polarization \mathbf{P} in the directions normal and lateral to the lamellar surface, the components of the depolarization field \mathbf{E}_P in the corresponding direction can be written as [34]

$$E_{pz} = -\frac{N_z P_z}{\varepsilon_0}, \quad E_{px} = -\frac{N_x P_x}{\varepsilon_0}, \quad E_{py} = -\frac{N_y P_y}{\varepsilon_0} \quad (2.5)$$

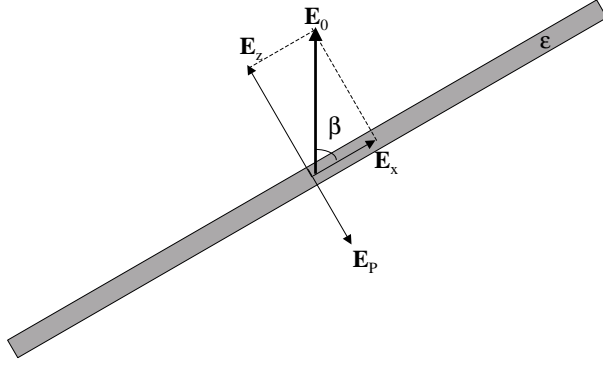


Figure 2.8: A single lamella domain with a dielectric constant ε having a large lateral size placed in an external electric field \mathbf{E}_0 . The depolarization field \mathbf{E}_P is always perpendicular to the lamellar surface for orientations with different angles β .

where N_x, N_y, N_z are the depolarizing factors whose values depend on the ratios of the sizes of the lamella in different dimensions. The N values are positive and satisfy the sum rule $N_x + N_y + N_z = 1$ in SI-system. From eqs. (2.3) - (2.5), the components of polarization can be calculated as

$$P_z = \frac{\varepsilon_0 \chi E_{0z}}{1 + N_z \chi}, \quad P_x = \frac{\varepsilon_0 \chi E_{0x}}{1 + N_x \chi}, \quad P_y = \frac{\varepsilon_0 \chi E_{0y}}{1 + N_y \chi} \quad (2.6)$$

If the lateral size of the lamella is much larger than the thickness of the lamella, the depolarization factors are given by [35]

$$N_z \approx 1, \quad N_x = N_y \approx 0 \quad (2.7)$$

Therefore eq. (2.5) becomes

$$E_{pz} = -\frac{P_z}{\varepsilon_0}, \quad E_{px} = E_{py} = 0 \quad (2.8)$$

showing that the depolarization field is only induced in the direction normal to the lamellar surface, and the polarization P_z in the normal direction is

$$P_z = \frac{\varepsilon_0 \chi E_{0z}}{1 + \chi} \quad (2.9)$$

Comparison of eq. (2.9) with eq. (2.3) yields

$$E_{pz} = \frac{E_{0z}}{1 + \chi} = \frac{E_{0z}}{\varepsilon} \quad (2.10)$$

The free energy of a dielectric body with a volume V in an external electric field \mathbf{E}_0 is given by [12]

$$F = F_0 + F_{el} = F_0 - \frac{1}{2} \int_V \mathbf{E}_0 \cdot \mathbf{P} \, dV \quad (2.11)$$

where F_0 contains all the contributions to the free energy independent of the external field, and F_{el} is the orientation dependent electrical contribution to the free energy. The free energy for the case of a single lamella having a large lateral size (shown in Fig. 2.8) can be calculated as

$$F = F_0 - \frac{1}{2} \int_V \mathbf{E}_0 \cdot \mathbf{P} \, dV$$

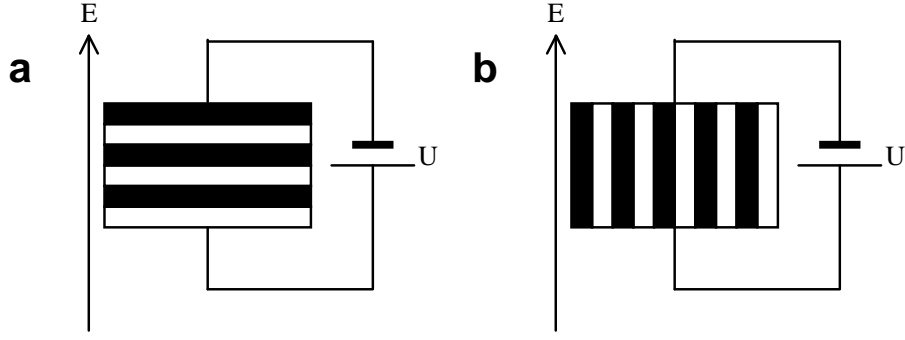


Figure 2.9: Capacitor analog for an ordered thin film of a symmetric AB diblock copolymer with the lamellae perpendicular (a) and parallel (b) to an external electric field. The capacitors filled with dielectric components A or B are in series and in parallel in the cases (a) and (b), respectively.

$$\begin{aligned}
&= F_0 - \frac{1}{2}\varepsilon_0(\varepsilon - 1)[\mathbf{E}_0 \cdot (\mathbf{E}_z + \mathbf{E}_x + \mathbf{E}_P)] V \\
&= F_0 - \frac{1}{2}\varepsilon_0(\varepsilon - 1)[\mathbf{E}_0 \cdot (\mathbf{E}_z + \mathbf{E}_P) + \mathbf{E}_0 \cdot \mathbf{E}_x] V \\
&= F_0 - \frac{1}{2}\varepsilon_0(\varepsilon - 1)[E_0 \frac{E_0 \sin \beta}{\varepsilon} \cos(\frac{\pi}{2} - \beta) + E_0 E_0 \cos \beta \cos \beta] V \\
&= F_0 - \frac{1}{2}\varepsilon_0(\varepsilon - 1)E_0^2(\frac{\sin^2 \beta}{\varepsilon} + \cos^2 \beta) V
\end{aligned} \tag{2.12}$$

where β is the angle between the lamellar surface and the external field \mathbf{E}_0 . The free energy is minimized when $\beta = 0$, i.e., when the lamellar surface is parallel to the external field. The difference in the free energy between lamellar orientations parallel and perpendicular to the applied field is obtained as

$$\Delta F = F_{\parallel} - F_{\perp} = -\frac{1}{2}\varepsilon_0 \frac{(\varepsilon - 1)^2}{\varepsilon} E_0^2 V \tag{2.13}$$

For an ordered thin film of a symmetric AB diblock copolymer with a parallel or perpendicular orientation to the surfaces, the free energy of the system can be obtained by using a capacitor analog [36]. If the lamellae are oriented perpendicular to the external electric field [Fig. 2.9 (a)], the film can be regarded as capacitors in series, filled with dielectric components A and B, respectively. If the lamellae are oriented parallel to the external field [Fig. 2.9 (b)], the film can be regarded as capacitors in parallel. If the components A and B have dielectric constants ε_A and ε_B , respectively, the whole capacitors C_{\perp} for the case (a) and C_{\parallel} for the case (b) can be shown as

$$C_{\perp} \sim \frac{2\varepsilon_A \varepsilon_B}{\varepsilon_A + \varepsilon_B} \tag{2.14}$$

and

$$C_{\parallel} \sim \frac{\varepsilon_A + \varepsilon_B}{2} \tag{2.15}$$

respectively, where the sign \sim denotes that the quantity on the left is proportional to the quantity on the right. The difference in the free energy between lamellar orientations parallel and perpendicular to the applied field can be written as

$$\Delta F = F_{\parallel} - F_{\perp} = -\frac{1}{2}(C_{\parallel} - C_{\perp})U^2 \sim -\frac{1}{2} \left[\frac{(\varepsilon_A - \varepsilon_B)^2}{2(\varepsilon_A + \varepsilon_B)} \right] \tag{2.16}$$

under the condition of a constant potential U . Comparison of eq. (2.16) with eq. (2.13) yields

$$\Delta F = F_{\parallel} - F_{\perp} = -\frac{1}{2}\varepsilon_0 \left[\frac{(\varepsilon_A - \varepsilon_B)^2}{2(\varepsilon_A + \varepsilon_B)} \right] E_0^2 V \quad (2.17)$$

showing that the free energy difference between the two orientations depends on the difference between the dielectric constants of the two components. Therefore the electric-field-induced alignment occurs only if the two components of the copolymer have different dielectric constants, and the effect will be larger if the difference $\Delta\varepsilon$ becomes larger.

2.4 Electric-field-induced structural undulations

In well aligned copolymer films with a parallel orientation to the substrate [shown in 2.5 (a)], the electric-field-induced lamellar reorientation perpendicular to the substrate is not feasible via a rotation of the whole lamellar domain by 90° . A more plausible pathway is to induce structural undulations which lead to a disruption of the original structure and facilitate the alignment to set in. The inducement of structural undulations will however increase the interfacial area between the lamellae, and also necessitate the stretching and compression of the chains since the substrate is flat [13]. These structural undulations are similar to the Helfrich-Hurault instability [37] in smectic liquid crystals, with the two fundamental long-wavelength modes [38] (longitudinal and transverse) shown in Fig. 2.10. Onuki and Fukuda [39, 40] investigated these

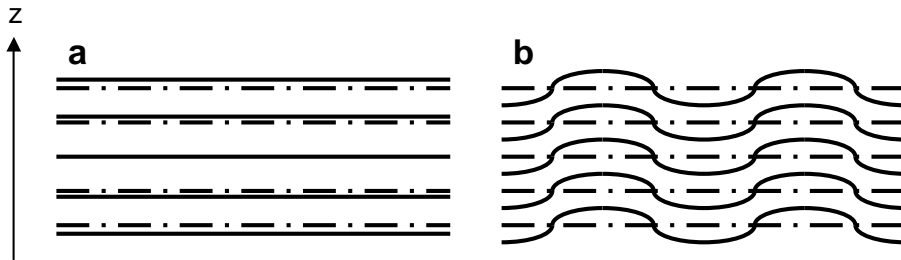


Figure 2.10: Two fundamental long-wavelength modes of electric-field-induced structural undulations in well aligned copolymer films, (a) longitudinal and (b) transverse, in analogy to the smectic-A phase liquid crystals.

electric-field-induced structural undulations at the soft, deformable lamellar interfaces in block copolymers by assuming an induced dipolar interaction among the composition fluctuations. The composition variation along the z axis (normal to the interfaces) can be expressed approximately as [40]

$$\phi(\mathbf{r}) = A \cos[q^*z - q^*u(\mathbf{r})] \quad (2.18)$$

where A is the amplitude of the structural undulations, q^* is the momentum transfer characterizing the lamellar period $d_p = 2\pi/q^*$ of the structure, and $u(\mathbf{r})$ is the displacement which can be expressed as [37]

$$u(x, z) = u_0(z) \cos(q_x x) \quad (2.19)$$

where u_0 depends on z , because the displacement must vanish at both surfaces. For small amplitude distortions (just above threshold) $u_0(z)$ can be taken as a sine wave, vanishing both for $z = 0$ and $z = d$ with d being the film thickness, such that

$$u_0(z) = u_0 \sin(q_z z) \quad (2.20)$$

where $q_z = \pi/d$. The elastic free energy due to the structural undulations can be written as [37]

$$F_u = \frac{1}{2} \int d\mathbf{r} \left[B \left(\frac{\partial u}{\partial z} \right)^2 + K_1 \left(\frac{\partial^2 u}{\partial x^2} + \frac{\partial^2 u}{\partial y^2} \right)^2 \right] \quad (2.21)$$

where B is the layer compressibility and K_1 is the elastic splay constant. The electrostatic energy due to the composition fluctuations of lamellae is given (in cgs units) by [7]

$$F_e = -\frac{1}{8\pi} \int_V d^3\mathbf{r} \varepsilon(\mathbf{r}) |\mathbf{E}(\mathbf{r})|^2 \quad (2.22)$$

where $\varepsilon(\mathbf{r})$ is the local dielectric constant and $\mathbf{E}(\mathbf{r})$ is the external electric field. The electric field obeys the Maxwell equation $\nabla \cdot [\varepsilon(\mathbf{r})\mathbf{E}(\mathbf{r})] = 0$, the solving result of which is given by [7]

$$F_e = -\frac{1}{2} g_e A^2 \int d\mathbf{r} |\nabla_{\perp} u(\mathbf{r})|^2 \quad (2.23)$$

with the coefficient g_e defined by

$$g_e = \frac{1}{4\pi\bar{\varepsilon}} \left(\frac{\partial \varepsilon}{\partial \phi} \right)^2 \bar{E}^2 \quad (2.24)$$

where $\bar{\varepsilon}$ is the average dielectric constant, and $\bar{E} = |\bar{\mathbf{E}}|$ is the average strength of the electric field. The total free energy can be expressed in the Fourier space in the form [40]

$$F = F_0 + F_u + F_e = \frac{1}{2} \left(\frac{1}{2\pi} \right)^3 \int d\mathbf{q} C_{\mathbf{q}} |u(\mathbf{q})|^2 \quad (2.25)$$

where F_0 contains all the contributions to the free energy independent of the electric field and the structural undulations. The coefficient $C_{\mathbf{q}}$ is written as

$$C_{\mathbf{q}} = B[q_z^2 + \lambda_1^2 q_{\perp}^2 (q_{\perp}^2 - q_e^2)] \quad (2.26)$$

where λ_1 is a natural length scale given by the two distortion coefficients as

$$\lambda_1 = \sqrt{\frac{K_1}{B}} \quad (2.27)$$

which is usually comparable to the lamellar period d_p . The wave number q_e is defined as

$$q_e = A \sqrt{\frac{g_e}{K_1}} \quad (2.28)$$

Amundson et al. have introduced an electric length scale ξ in (4.13) of ref. [8], which is just the inverse of q_e . The undulations will grow if the electrostatic energy in eq. (2.25) overcomes the elastic free energy of the induced undulations, i.e., $C_{\mathbf{q}}$ expressed in eq. (2.26) is negative. Therefore

$$q_z^2/q_{\perp}^2 + \lambda_1^2 q_{\perp}^2 < \lambda_1^2 q_e^2 \quad (2.29)$$

Because the minimum wave number in the z direction is

$$q_z = \pi/d \quad (2.30)$$

due to the limit that the displacement vanishes at both surfaces, the left hand side of eq. (2.29) is minimized at

$$q_{\perp} = \sqrt{\frac{q_z}{\lambda_1}} = \sqrt{\frac{\pi}{d\lambda_1}} \quad (2.31)$$

The criterion of the linear instability is thus given by

$$q_e > \sqrt{\frac{2\pi}{d\lambda_1}} \quad (2.32)$$

2.5 Competing effects

The alignment of the lamellae by the surface effects and the electric fields effects have been discussed in the previous sections. An interesting situation arises if an electric field is applied perpendicular to the lamellar interfaces which are original aligned parallel to the substrate by the surface effects. In this situation the alignment by the electric field is in competition with the alignment by the surface effects. Tsori and Andelman [41, 42] studied this situation in the weak and strong segregation limits of block copolymers. In the weak segregation limit, surface interactions stabilize the lamellar orientation parallel to the substrate below a critical field E_c , and the morphology is a superposition of parallel and perpendicular lamellae above the critical field. For diblock copolymers in the strong segregation limit, a mixed orientation with boundary layers parallel and the lamellae in the middle of the film perpendicular to the substrate was found if the surface effects are strong enough or the film is thick enough. “T”-junction morphologies as shown in Fig. 2.11 will exist at the boundary of regions with the parallel and perpendicular orientations. A dimensionless parameter δ measuring the difference in

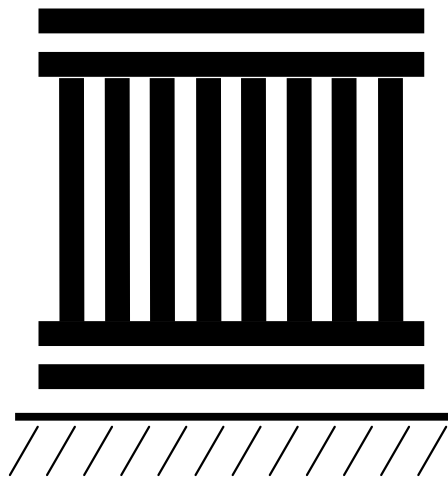


Figure 2.11: Schematic drawing of “T”-junction defect structures.

A- and B- surface interactions is defined as [42]

$$\delta \equiv \frac{\sigma}{\gamma_T} = \frac{\sigma_{AS} - \sigma_{BS}}{\gamma_T} \quad (2.33)$$

where σ is the difference in the A- and B- block surface interactions, and γ_T is the energy penalty per unit area associated with the “T”-junction defects. In the case of strong surface effects, i.e., δ is larger than a threshold value δ^* , two critical fields E_1 and $E_2 > E_1$ were found. As the field is increased from zero to E_1 , the parallel orientation is favored. If the field is increased above E_1 , the region in the middle of the film develops an orientation perpendicular to the surfaces, while the surface regions still have parallel lamellae. If the field is increased above E_2 , the perpendicular alignment spans the whole film. In the case of weak surface effects, i.e., $\delta < \delta^*$, only one critical field E_3 was found and the transition from parallel to perpendicular orientation is direct. A mixed

orientation only occurs if $\delta > \delta^*$, or alternatively if $d > d^*$ for a given δ , where d is the film thickness and d^* is a critical film thickness.

Chapter 3

Neutron scattering

3.1 Basic concepts

A neutron is an uncharged elementary particle, possessing a mass $m = 1.675 \times 10^{-27}$ kg and spin 1/2. Neutrons exhibit wave-like behavior with the wavelength λ given by the relation

$$\lambda = \frac{h}{p} = \frac{h}{mv} \quad (3.1)$$

where $h = 6.626 \times 10^{-34}$ Js is the Planck's constant. p and v are the momentum and the velocity of the neutron particle, respectively. The neutron wavelength used for the study of structure of materials are typically on the order of \AA , which is of the same order of magnitude as most interatomic distances of interest in condensed matters. As a result, neutrons can be very useful tool for investigating the structures of materials.

Suppose an incident neutron beam irradiates a sample, from which the neutrons are scattered in all directions based on the interaction between the material and the neutrons. A neutron scattering experiment measures the scattering intensity as a function of scattering direction and interpreting the data gives information about the structure of the sample. The flux of incidence is often a plane wave J_0 , whereas the scattered beam is a spherical wave J which is expressed by the amount of energy transmitted per second through a unit solid angle rather than a unit area (Fig. 3.1). In this way the measured flux becomes independent of the distance from the source to the point of observation. The ratio of J/J_0 is defined as the **differential scattering cross section**

$$\frac{d\sigma}{d\Omega} \equiv \frac{J}{J_0} \quad (3.2)$$

which has dimension of area per solid angle. Integrating the differential scattering cross

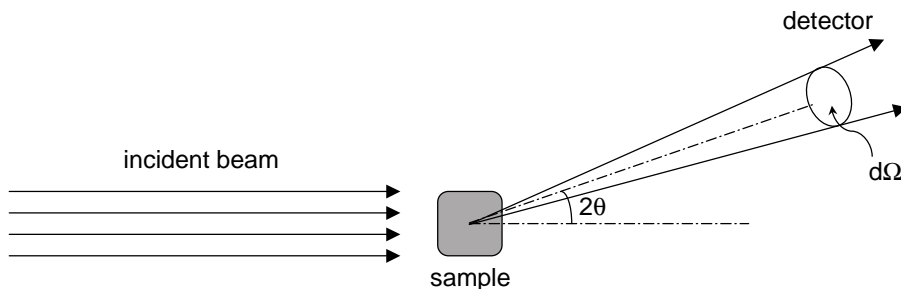


Figure 3.1: Basic geometry of scattering involving the incident plane wave, the sample, the scattered spherical wave and the detector.

section throughout the solid angle Ω gives the **total scattering cross section**

$$\sigma_{tot} = \int_{\text{all directions}} \left(\frac{d\sigma}{d\Omega} \right) d\Omega \quad (3.3)$$

which has therefore dimension of area, as the word cross section implies. The total scattering cross section of a nucleus is related to the **scattering length** b of the nucleus through [43]

$$\sigma_{tot} = \int \left(\frac{d\sigma}{d\Omega} \right) d\Omega = b^2 \quad (3.4)$$

The scattering length b has dimension of length. The neutron, with spin $1/2$, interacts with a nucleus of spin i to give a total number of $4i + 2$ states. Among these spin states, $2i + 2$ of them have the total spin $i + 1/2$ and the scattering length b^+ , and $2i$ of them have the total spin $i - 1/2$ and the scattering length b^- . Each spin state has the same probability if the neutron beam is unpolarized so that the nuclear spin is randomly oriented. The consequence of such a random variability in the scattering lengths, resulting either from the presence of isotopes or from nonzero nuclear spin, is that the scattering intensity contains not only a component that reflects the structure of the sample, but also another component that arises simply from this randomness and has nothing to do with the structure. These two components of the scattering intensity are characterized by the **coherent** and **incoherent scattering lengths**, b_{coh} and b_{inc} , respectively. The coherent and incoherent scattering lengths are defined as

$$b_{coh} = \langle b \rangle \quad (3.5)$$

and

$$b_{inc} = \sqrt{\langle b^2 \rangle - \langle b \rangle^2} \quad (3.6)$$

where $\langle \dots \rangle$ denotes the average over all nucleus in the sample. Since the incoherent scattering does not give information about the structure of the sample, we will only use the coherent scattering length b_{coh} in our discussion, and will omit the subscript in the later text. The **scattering length density** ρ is defined as

$$\rho = b \frac{N}{V} \quad (3.7)$$

where N is the average number of the nuclei in a volume V . The dimension of the scattering length density is therefore length^{-2} .

The scattering length density of a material is related to the refractive index n of the material [43]

$$n = 1 - \delta + i\beta \quad (3.8)$$

through

$$\delta = \frac{\lambda^2}{2\pi} \rho \quad (3.9)$$

and

$$\beta = \frac{\lambda}{4\pi} \rho_{abs} \quad (3.10)$$

where ρ and ρ_{abs} are the scattering length density and the absorption cross-section density, respectively. For neutrons the absorption is sufficiently small such that β can be neglected in most cases.

In many ways the properties of neutrons and their scattering behavior are similar to those exhibited by x-rays. Both of them are non-destructive probe for studying structure

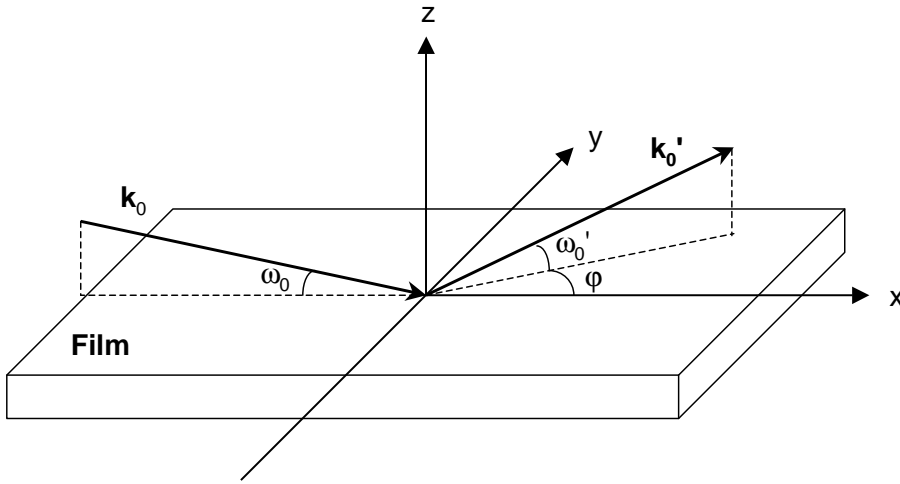


Figure 3.2: Geometry of specular and off-specular scattering from a film surface. \mathbf{k}_0 and \mathbf{k}'_0 are the incident and scattered wave vectors, respectively.

and morphology of interfaces in thin films. However, their scattering lengths (the quantity to measure the ability of materials to scatter the x-ray or neutron beams) are complementary to each other. Although the x-ray scattering length depends primarily on the number of electrons an atom contains and therefore increases linearly with atomic number, the neutron scattering length can vary greatly between elements neighboring in terms of atomic number and even between isotopes of the same element. For example, the two isotopes, hydrogen ^1H and deuterium ^2D , have coherent neutron scattering lengths that are very different from each other. If some or all of the hydrogens in polymer molecules are replaced by deuterium, the cross section for scattering neutrons will be greatly modified, with all the other physical properties of the molecules remaining essentially unaltered. This is referred to the deuterium labeling technique for studying polymers. A second advantage of neutron scattering is that most materials (except for the elements Li, B, Cd, Sm, Gd, which have a relatively large absorbance [44]) are transparent to neutrons. Therefore the intensity of the incident beam will not be reduced significantly even after the beam traverses a considerable distance away from the sample surface. This allows to detect the inner structure, in addition to the surface structure of the sample. Based on these reasons, we choose neutron scattering as a tool for our study. Basically, three types of neutron scattering methods were used in our experiments, namely, specular, off-specular and small-angle neutron scattering. We will discuss them one by one in the following sections.

As shown in Fig. 3.2, the plane containing z (normal to the surface) and the incident wave vector \mathbf{k}_0 is defined as the plane of incidence. The reflected wave vector \mathbf{k}'_0 is not necessarily in the plane of incidence. If the reflected beam is in the plane of incidence and the reflected angle ω'_0 is equal to the incident angle ω_0 , the reflection is termed **specular**. The scattering vector $\mathbf{q} = \mathbf{k}'_0 - \mathbf{k}_0$ for such a specular reflection is normal to the surface, and its x and y components are both equal to zero. If the surface is perfectly flat, and there is no variation in the scattering length density in the x and y directions, only a specular reflection will occur. The **reflectivity**, the ratio of the reflected beam energy to the incident beam energy, is then measured as a function of the magnitude of \mathbf{q} while its direction is kept normal to the surface. The result of a reflectivity measurement gives information about the variation in the scattering length density $\rho(z)$, in the material as a function of depth z from the surface. If the surface is not perfectly flat or if the material near the surface contains some inhomogeneities in

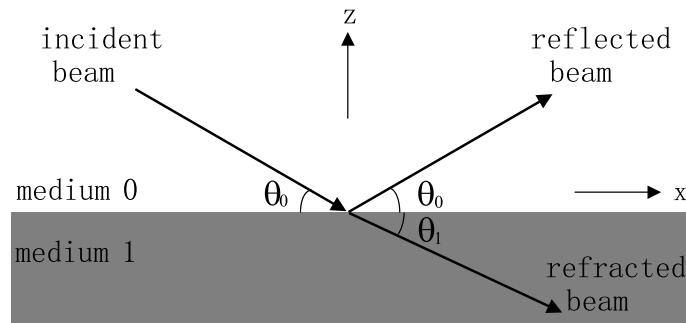


Figure 3.3: Geometry of reflection and refraction.

the x or y direction, the scattering intensity may be measured in both the specular and nonspecular directions (any other directions different from specular). The scattering in the nonspecular directions (usually vanishes within a few degrees of it) is referred to as *off-specular* or *diffuse scattering*. The scattering vector \mathbf{q} in such a diffuse scattering measurement contains a finite q_x or q_y component. The diffuse scattering intensity gives then information about the surface topology or the scattering length density inhomogeneity in the x or y direction.

3.2 Scattering from sharp interfaces

In this section, we will discuss the scattering from perfectly flat (or sharp) interfaces, and there is no variation in the scattering length density in the lateral directions. As mentioned before, only specular reflection (or reflectivity) will occur at such interfaces.

3.2.1 Snell's law

A neutron beam incident on an interface will undergo refraction and reflection provided the refractive indices of the media on the two sides of the interface are different (Fig. 3.3). The refractive indices of the two media determine the angle at which the neutron beam is refracted, according to the Snell's law

$$n_0 \cos \theta_0 = n_1 \cos \theta_1 \quad (3.11)$$

where n_0 and n_1 are the refractive indices for the media 0 and 1, respectively. The medium 0 is usually air with a refractive index $n_0 = 1$. Since n_1 is generally less than 1, the refraction angle θ_1 is smaller than the incident angle θ_0 . Consequently, there exists a critical angle of incidence in medium 0 below which the neutron beam is totally reflected back into medium 0. The critical angle θ_c is given by

$$\cos \theta_c = n_1 \quad (3.12)$$

From eq. (3.11) we can write

$$n_0^2(1 - \sin^2 \theta_0) = n_1^2(1 - \sin^2 \theta_1) \quad (3.13)$$

Similarly, from eq. (3.12) we can write

$$n_0^2(1 - \sin^2 \theta_c) = n_1^2 \quad (3.14)$$

with $n_0 = 1$. Taking the difference between eqs. (3.14) and (3.13) leads to

$$n_0^2 \sin^2 \theta_0 - n_0^2 \sin^2 \theta_c = n_1^2 \sin^2 \theta_1 \quad (3.15)$$

which can be written as

$$k_{z,0}^2 - k_{c,0}^2 = k_{z,1}^2 \quad (3.16)$$

and equivalently

$$k_{z,1} = \sqrt{k_{z,0}^2 - k_{c,0}^2} \quad (3.17)$$

where $k_{z,0}$ and $k_{z,1}$ are the z -components of the wave vectors of the incident and the refracted beams, and $k_{c,0}$ is the value of $k_{z,0}$ when θ_0 is equal to the critical angle θ_c , i.e.,

$$k_{c,0} = \frac{2\pi}{\lambda} \sin \theta_c \quad (3.18)$$

3.2.2 Reflectivity from a single interface

In this section, we will follow the method shown in the book by Roe [43]. For a single interface between two homogeneous media, taking the origin of z at the interface and consider only the z -component of the wave amplitude, we can represent the incident wave at height z as $A(z) = \exp(ik_{z,0}z)$. If r and t ($= 1 - r$) are the fractions of amplitudes of the wave reflected and transmitted at the interface respectively, the wave amplitudes in media 0 and 1 are given by

$$A_0(z) = \exp(ik_{z,0}z) + r \exp(-ik_{z,0}z) \quad (3.19)$$

and

$$A_1(z) = t \exp(ik_{z,1}z) \quad (3.20)$$

respectively. The wave must be continuous and smoothly varying across the interface, i.e., the values of $A(z)$ and $dA(z)/dz$ on either side of the interface must be the same. These two requirements can be expressed as

$$\exp(ik_{z,0}z) + r \exp(-ik_{z,0}z) = (1 - r) \exp(ik_{z,1}z) \quad (3.21)$$

and

$$ik_{z,0} \exp(ik_{z,0}z) - ik_{z,0}r \exp(-ik_{z,0}z) = ik_{z,1}(1 - r) \exp(ik_{z,1}z) \quad (3.22)$$

respectively. Subtraction of eq. (3.22) from eq. (3.21) multiplied by $ik_{z,1}$ leads to

$$i(k_{z,1} - k_{z,0}) \exp(ik_{z,0}z) + \frac{i(k_{z,1} + k_{z,0})r}{\exp(ik_{z,0}z)} = 0 \quad (3.23)$$

At $z = 0$, $\exp(ik_{z,0}z) = 1$, thus the reflectance or the reflection coefficient r is calculated as

$$r = \frac{k_{z,0} - k_{z,1}}{k_{z,0} + k_{z,1}} \quad (3.24)$$

The reflectivity R is the absolute square of r and is given by

$$R = |r|^2 = rr^* \quad (3.25)$$

In the case of a single interface, the reflectivity is called the **Fresnel reflectivity** R_F and is given by

$$R_F = \left| \frac{k_{z,0} - k_{z,1}}{k_{z,0} + k_{z,1}} \right|^2 \quad (3.26)$$

Substituting eq. (3.17) into eq. (3.26), we obtain

$$R_F = \left| \frac{k_{z,0} - \sqrt{k_{z,0}^2 - k_{c,0}^2}}{k_{z,0} + \sqrt{k_{z,0}^2 - k_{c,0}^2}} \right|^2 = \left| \frac{1 - \sqrt{1 - (k_{c,0}/k_{z,0})^2}}{1 + \sqrt{1 - (k_{c,0}/k_{z,0})^2}} \right|^2 \quad (3.27)$$

For $k_{z,0} \gg k_{c,0}$, $\sqrt{1 - (k_{c,0}/k_{z,0})^2} \approx 1 - \frac{1}{2}(k_{c,0}/k_{z,0})^2$, and R_F is approximated by

$$R_F \approx \left| \frac{1 - [1 - \frac{1}{2}(k_{c,0}/k_{z,0})^2]}{1 + [1 - \frac{1}{2}(k_{c,0}/k_{z,0})^2]} \right|^2 \approx \frac{1}{16} \left(\frac{k_{c,0}}{k_{z,0}} \right)^4 \quad (3.28)$$

showing that the tail of the reflectivity curve decays as q_z^{-4} , as in the Porod's law.

3.2.3 Reflectivity from two parallel interfaces

In this section, we will again follow the method shown in the book by Roe [43]. An example of a system with two parallel interfaces is shown in Fig. 3.4. The reflected

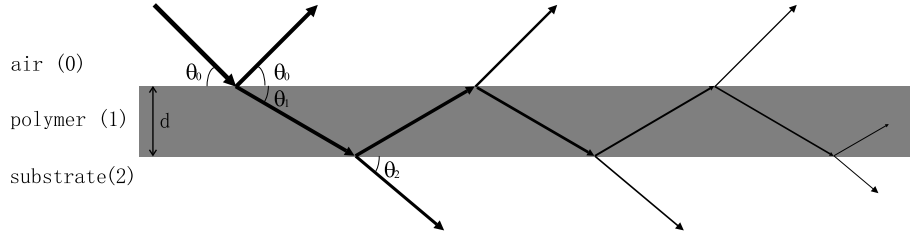


Figure 3.4: An example of a system with two parallel interfaces: a polymer film of thickness d deposited on a thick, flat substrate. The air, the polymer film, and the substrate are denoted as medium 0, 1, and 2, respectively.

neutron beam that is observed for such a system will consist not only of beams reflected at the 0-1 interface, but also of beams transmitted from medium 1 to medium 0 after having been reflected at the 1-2 interface once, twice, etc. Consider, e.g., one particular beam emerging from the 0-1 interface has been reflected twice at the 1-2 interface. If the amplitude of the beam incident on the 0-1 interface has a magnitude 1, each time the beam encounters an interface, its amplitude is reduced by a factor equal to either the reflectance or the transmission coefficient, as shown in Fig. 3.5. When the beam

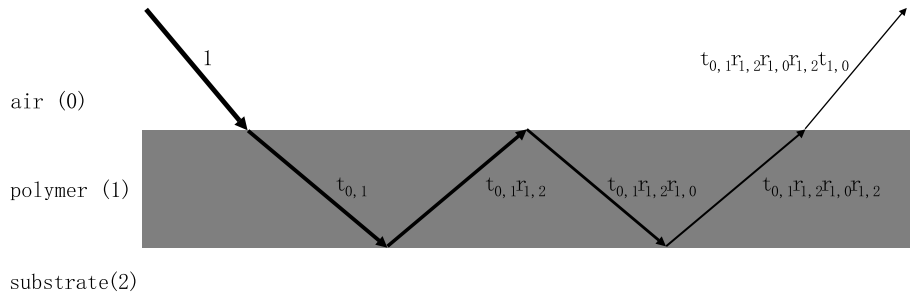


Figure 3.5: Illustration of the successive change in the magnitude of the amplitude of a ray, as it is either reflected or refracted on encountering an interface.

finally emerges from the 0-1 interface, its amplitude is reduced to $t_{0,1}r_{1,2}r_{1,0}r_{1,2}t_{1,0}$. In addition, the beam suffers a phase shift equal to $4\phi_1$ compared with the beam reflected directly at the 0-1 interface, where ϕ_1 is given by

$$\phi_1 = k_{z,1}d \quad (3.29)$$

The overall reflectance r is the sum of amplitudes of all the beams emerging from the 0-1 interface, and is given by

$$r = r_{0,1} + t_{0,1}r_{1,2}t_{1,0} \exp(-i2k_{z,1}d) + \cdots + t_{0,1}r_{1,2}(r_{1,0}r_{1,2})^{m-1}t_{1,0} \exp(-i2mk_{z,1}d) + \cdots \quad (3.30)$$

where $m = 1, \dots, \infty$ is the number of times the beam has been reflected at the 1-2 interface before emerging into medium 0. Eq. (3.30) can be summed to give

$$r = r_{0,1} + \frac{t_{0,1}t_{1,0}r_{1,2} \exp(-i2k_{z,1}d)}{1 - r_{1,0}r_{1,2} \exp(-i2k_{z,1}d)} \quad (3.31)$$

For a sharp interface between two homogeneous media denoted as j and $j + 1$, the reflectance $r_{j,j+1}$ is generalized from eq. (3.24) to be

$$r_{j,j+1} = \frac{k_{z,j} - k_{z,j+1}}{k_{z,j} + k_{z,j+1}} \quad (3.32)$$

where $k_{z,j}$ and $k_{z,j+1}$ are the z -component of the wave vector in media j and $j + 1$, respectively. And the transmission coefficient $t_{j,j+1}$ is

$$t_{j,j+1} = \frac{2k_{z,j+1}}{k_{z,j} + k_{z,j+1}} \quad (3.33)$$

From eqs. (3.32) and (3.33) we know that

$$r_{1,0} = -r_{0,1} \quad (3.34)$$

and

$$t_{0,1}t_{1,0} = 1 - r_{0,1}^2 \quad (3.35)$$

Eq. (3.31) is therefore rewritten as

$$r = \frac{r_{0,1} + r_{1,2} \exp(-i2k_{z,1}d)}{1 + r_{0,1}r_{1,2} \exp(-i2k_{z,1}d)} \quad (3.36)$$

The reflectivity R is then

$$R = \left| \frac{r_{0,1} + r_{1,2} \exp(-i2k_{z,1}d)}{1 + r_{0,1}r_{1,2} \exp(-i2k_{z,1}d)} \right|^2 = \frac{r_{0,1}^2 + r_{1,2}^2 + 2r_{0,1}r_{1,2} \cos(2k_{z,1}d)}{1 + r_{0,1}^2r_{1,2}^2 + 2r_{0,1}r_{1,2} \cos(2k_{z,1}d)} \quad (3.37)$$

The calculated reflectivity profile for a system involving a film with a thickness of 500 Å on a thick, flat substrate is shown in Fig. 3.6. As can be seen, the reflectivity profile contains a series of maxima or minima, from which the film thickness d can be calculated as

$$d = \frac{\pi}{\Delta k_z} = \frac{2\pi}{\Delta q_z} \quad (3.38)$$

where Δk_z and Δq_z are the interval in k_z and q_z between successive maxima or minima, respectively.

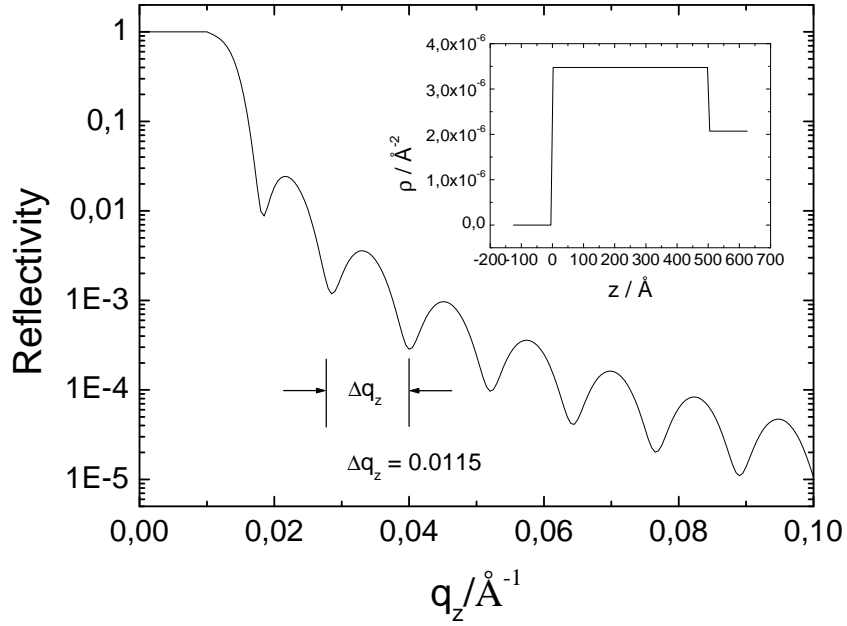


Figure 3.6: Calculated reflectivity profile for a film of thickness 500 Å on a thick, flat substrate. The reflectivity profile is calculated from the density profile (inset) by the software package Parratt32 .

3.2.4 Reflectivity from multiple interfaces

Exact method: Parratt algorithm

The above method can be extended to a multilayer system with $(n + 1)$ media and n interfaces. The reflectance and reflectivity calculated in this way is exact. However, the calculation becomes too complicated as soon as the number of layers involved exceeds four or five. Another exact recursive method was suggested by Parratt [45]. An easier understandable description to this method can be found in the book [46]. Consider a multilayer system with each layer j ($j = 0, \dots, n$) having a refractive index $n_j = 1 - \delta_j + i\beta_j$ and being of thickness d_j . The z direction is normal to the interfaces and the x direction is the lateral direction, as shown in Fig. 3.3. The total wave vector k_j in medium j is determined by $k_j = n_j k_0$ ($n_0 = 1$ for air), and the x -component of the wave vector is conserved through all layers so that $k_{x,j} = k_{x,0}$ for all j . The z -component of the wave vector is found to be

$$\begin{aligned} k_{z,j} &= \sqrt{k_j^2 - k_{x,j}^2} = \sqrt{(n_j k_0)^2 - k_{x,0}^2} \\ &= \sqrt{(1 - \delta_j + i\beta_j)^2 k_0^2 - k_{x,0}^2} \approx \sqrt{k_{z,0}^2 - 2\delta_j k_0^2 + i2\beta_j k_0^2} \end{aligned} \quad (3.39)$$

The first step is to calculate the reflectance $r_{n-1,n}$ at the interface between the substrate (denoted as medium n) and the layer closest to the substrate (denoted as medium $n-1$). As the substrate is infinitely thick there are no multiple reflections. The reflectance $r_{n-1,n}$ at this interface can be calculated exactly from eq. (3.32) as

$$r_{n-1,n} = \frac{k_{z,n-1} - k_{z,n}}{k_{z,n-1} + k_{z,n}} \quad (3.40)$$

The reflectance $r_{n-2,n-1}$ at the interface between the $(n-2)$ th and $(n-1)$ th layers is then calculated from eq. (3.36) as

$$r_{n-2,n-1} = \frac{r_{n-2,n-1} + r_{n-1,n} \exp(-i2k_{z,n-1}d_{n-1})}{1 + r_{n-2,n-1}r_{n-1,n} \exp(-i2k_{z,n-1}d_{n-1})} \quad (3.41)$$

which allows for the multiple scattering and refraction from the $(n - 1)$ th layer. It follows that the reflectance at the next interface up is

$$r_{n-3,n-2} = \frac{r_{n-3,n-2} + r_{n-2,n-1} \exp(-i2k_{z,n-2}d_{n-2})}{1 + r_{n-3,n-2}r_{n-2,n-1} \exp(-i2k_{z,n-2}d_{n-2})} \quad (3.42)$$

and it is clear that the process can be continued recursively until the total reflectance $r_{0,1}$ at the interface between the air and the 1st layer is obtained.

The Parratt exact recursive method is used for calculating the reflectivity from systems with discrete layers, which is suitable for our layered diblock copolymer system. This method has been developed into a software package Parratt32¹, and was used as the main tool for analyzing the reflectivity data obtained from our experiments. The procedure to use this software involves assuming a model of density profile, calculating the reflectivity profile from the assumed model and comparing with the measured one. Discrepancies between the measured and the calculated profiles can be minimized by an iterative process where the variables used in the assumed model are systematically varied. In general, this method of fitting the observed data is time consuming. Additional knowledge of the system, obtained from other independent methods of study, is therefore usually indispensable to serve to reduce the number of variables used in the assumed model.

Approximate method: kinematic approximation

The method described in the previous section is exact, but being entirely numerical, does not easily provide insight into the relationship between the scattering length density profile assumed and the reflectivity profile calculated. An approximate method, called the kinematic (or first Born) approximation, will however provide us such a link between the density profile and the reflectivity profile. The kinematic approximation is only valid when the scattering is weak so that the scattering occurs only once within the sample and the multiple reflections can be neglected. The condition is fulfilled when the incident angle is much larger than the critical angle θ_c . The resulting reflectivity R calculated from the kinematic approximation (for details, see for example [43], [44]) for $k_{z,0} \gg k_{c,0}$ is

$$\frac{R}{R_F} = \left| \int \rho'(z) \exp(-i2k_{z,0}z) dz \right|^2 \quad (3.43)$$

where R_F is the ideal Fresnel reflectivity given by eq. (3.28). Eq. (3.43) shows that the reflectivity R is governed by the Fourier transform of the scattering length density gradient $\rho'(z)$ in the z direction normal to the surface.

The insight provided by the kinematic approximation method into the relationship between the scattering length density profile and the corresponding reflectivity profile is shown in Fig. 3.7. In the case of a single interface, the density gradient is a delta function, and the reflectivity is the Fresnel reflectivity. In the case of two parallel interfaces, e.g., a polymer film with a thickness d on an infinitely thick substrate, the density gradient consists of two delta functions. The second delta function produces a periodic oscillation (the Kiessig fringes) superposed on the Fresnel reflectivity. The film thickness can be calculated from the separation distance of the Kiessig fringes. Finally, in the case of a periodic multilayer system, e.g., in a symmetric diblock copolymer film where the two components form an -AB-AB-AB- layered structure, two series of periodic oscillations appear in the reflectivity. The Bragg peaks with the larger amplitude and

¹This software package was developed at the Hahn-Meitner-Institute, Berlin, Germany.

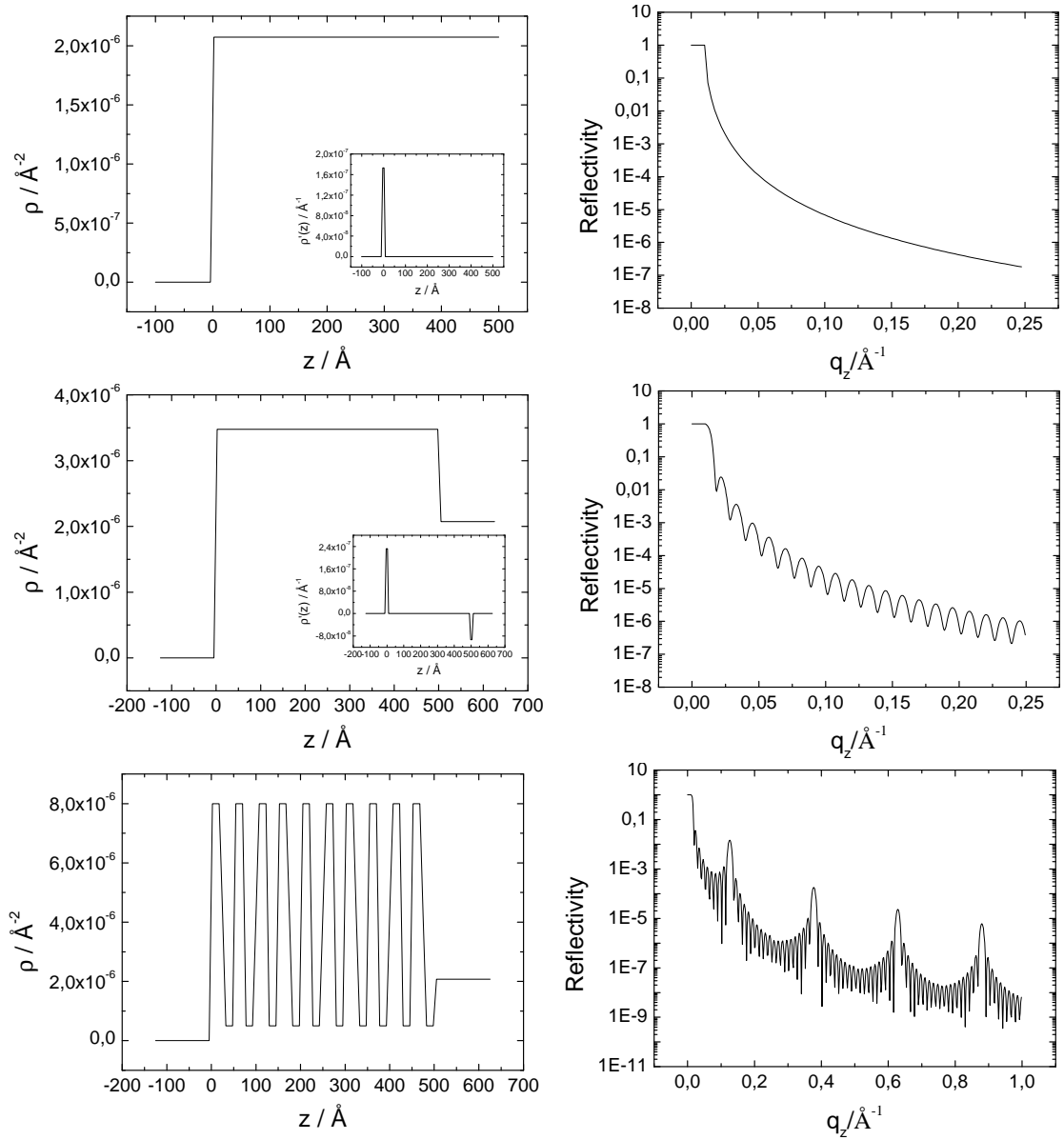


Figure 3.7: Relationship between the density profiles and the corresponding reflectivity profiles for systems involving a single interface (upper part), two parallel interfaces (middle part) and multiple interfaces with periodical structures (lower part), respectively. The insets in the first two cases show the density gradients calculated from the corresponding density profiles. Although the figure is used to show the insight provided by the kinematic approximation method, the reflectivity profiles shown here are all calculated using the software package Parratt32.

lower frequency characterizing the lamellar period d_p , are superposed on the Kiessig fringes with the smaller amplitude and higher frequency which characterizes the film thickness d .

3.3 Scattering from rough interfaces

3.3.1 Scattering from a single rough interface

If the interface is not perfectly flat (or sharp), which is the usual case in reality, both specular reflectivity and off-specular diffuse scattering will occur at the interface. The scattering function $S(\mathbf{q})$ for a single rough interface is given by [47]

$$S(\mathbf{q}) = \frac{A(\Delta\rho)^2}{q_z^2} e^{-q_z^2\sigma^2} \int \int dx dy e^{q_z^2 C(\mathbf{R})} e^{-i(q_x x + q_y y)} \quad (3.44)$$

where \mathbf{q} is the scattering vector, A is the illuminated area, $\Delta\rho$ is the scattering length density contrast between the media on either side of the interface, and σ is the root-mean-square (rms) roughness of the interface. $C(\mathbf{R})$ is the height-height correlation function $C(\mathbf{R}) = \langle \delta z(0) \delta z(\mathbf{R}) \rangle$. Eq. (3.44) is only valid if the scattering vector q is not too small to approach the critical edge so that we can use the Born Approximation. In addition, it is reasonable to assume the media have no internal structure except at the interfaces for $q^{-1} \gg$ typical atomic length scales in the media. Since $C(\mathbf{R}) \rightarrow 0$ as $\mathbf{R} \rightarrow \infty$, the integral in eq. (3.44) contains a delta-function part in (q_x, q_y) which corresponds to the specular reflectivity and can be explicitly separated out by subtracting 1 from the integrand. Thus we have [47]

$$S_{\text{specular}}(\mathbf{q}) = \frac{A(\Delta\rho)^2}{q_z^2} e^{-q_z^2\sigma^2} 4\pi^2 \delta(q_x) \delta(q_y) \quad (3.45)$$

which can be shown [48] to reduce to the formula for the specular reflectivity for a single rough interface

$$R(\mathbf{q}_z) = \frac{16\pi^2(\Delta\rho)^2}{q_z^4} \exp(-q_z^2\sigma^2) \quad (3.46)$$

Another way to obtain eq. (3.46) is as follows. The scattering length density contrast for a rough interface can be considered as the convolution of that for a sharp interface $\Delta\rho(z)$ with a smearing function $g(z)$, i.e.,

$$\Delta\rho_{\text{rough}}(z) = \Delta\rho(z) * g(z) \quad (3.47)$$

where $g(z)$ is usually a Gaussian function

$$g(z) = \frac{1}{\sqrt{2\pi\sigma^2}} \exp\left(-\frac{z^2}{2\sigma^2}\right) \quad (3.48)$$

The resulting reflectivity calculated from the kinematic approximation is

$$R(\mathbf{q}_z) = \frac{16\pi^2(\Delta\rho)^2}{q_z^4} \exp(-q_z^2\sigma^2) = R_F \exp(-q_z^2\sigma^2) \quad (3.49)$$

where R_F is the Fresnel reflectivity expected from a sharp interface. This result shows that the reflectivity falls off more rapidly with a rough interface than it does with a sharp interface. Apart from the reflectivity, the diffuse scattering function for a single

rough interface can be obtained from the difference between eqs. (3.44) and (3.45) as [47]

$$S_{diffuse}(\mathbf{q}) = \frac{A(\Delta\rho)^2}{q_z^2} e^{-q_z^2\sigma^2} \int \int dx dy [e^{q_z^2 C(\mathbf{R})} - 1] e^{-i(q_x x + q_y y)} \quad (3.50)$$

Before discussing the scattering from multiple rough interfaces (as in our cases), basic concepts for rough interfaces such as the correlation function and the types of correlation function, will be firstly introduced. The reflectivity and diffuse scattering from multiple rough interfaces will be calculated theoretically. The effect of slit collimation (integrating the intensity over one lateral direction) will be discussed. And finally the formula to calculate the interfacial roughness from the diffuse scattering of the system will be given.

3.3.2 Characterization of surface roughness

For simplicity we assume that the height profile of a given surface is a single valued function $z(\mathbf{R})$ at lateral position \mathbf{R} in the (x, y) plane. The height fluctuation is

$$\delta z(\mathbf{R}) = z(\mathbf{R}) - \langle z(\mathbf{R}) \rangle \quad (3.51)$$

where $\langle z(\mathbf{R}) \rangle$ denotes the average of the height $z(\mathbf{R})$. The rms roughness σ is defined to characterize the roughness of the surface as

$$\sigma = \sqrt{\frac{1}{A} \int [\delta z(\mathbf{R})]^2 d\mathbf{R}} \quad (3.52)$$

where A is the area of the surface over which the integral is taken. Obviously, the rms roughness is far from enough to describe the roughness of a surface, and the height distribution function $H(\mathbf{R})$ gives then more information about the surface. The height distribution function is a characteristic property of a given surface, while it is usually a good choice for the height distribution function to be a Gaussian function

$$H(\mathbf{R}) = \frac{1}{\sqrt{2\pi\sigma^2}} \exp\left(-\frac{\mathbf{R}^2}{2\sigma^2}\right) \quad (3.53)$$

However, the height distribution function only gives information about the statistics at individual positions \mathbf{R} , but does not reflect correlations between two different points \mathbf{R}_1 and \mathbf{R}_2 . Different rough surfaces can have the same rms roughness and height distribution functions, but different height fluctuation frequencies. To account for these properties we introduce the height-height correlation function $C(\mathbf{R})$ as

$$C(\mathbf{R}) = \langle \delta z(\mathbf{R}_1) \delta z(\mathbf{R}_2) \rangle = \langle \delta z(\mathbf{0}) \delta z(\mathbf{R}) \rangle \quad (3.54)$$

where $\mathbf{R} = |\mathbf{R}_1 - \mathbf{R}_2|$ and the ensemble average is taken over all pairs of points on the surface whose distance in the (x, y) plane is R . Then the rms roughness and the height-height correlation function are connected by

$$C(\mathbf{0}) = \langle [\delta z(\mathbf{0})]^2 \rangle = \sigma^2 \quad (3.55)$$

The rms roughness, the height distribution function and the height-height correlation function are known as the zero-, first- and second- order statistics [49]. The height-difference correlation function for real-valued height profiles is also introduced as

$$g(\mathbf{R}) = \langle [\delta z(\mathbf{0}) - \delta z(\mathbf{R})]^2 \rangle \quad (3.56)$$

fulfilling

$$g(\mathbf{0}) = 0 \quad (3.57)$$

and is connected with the height-height correlation function by

$$g(\mathbf{R}) = 2[\sigma^2 - C(\mathbf{R})] \quad (3.58)$$

In the literature the height-height correlation function is sometimes normalized by a factor σ^2 , such that $C(\mathbf{0}) = 1$ is referred to as the autocorrelation function and the height-difference correlation function as the height-height correlation function.

3.3.3 Types of correlation function

Three ideal correlation functions are usually used. They are exponential, Gaussian and self-affine, as listed in table 3.1. An important parameter ξ arises from the fit of the

	$C(R)$
Exponential	$C(R) = \sigma^2 \exp(-\frac{R}{\xi})$
Gaussian	$C(R) = \sigma^2 \exp(-\frac{R^2}{\xi^2})$
Self-affine	$C(R) = \sigma^2 \exp[-(\frac{R}{\xi})^{2h}]$

Table 3.1: Different ideal correlation functions, where the rms roughness σ , the correlation length ξ and the roughness exponent h are fit parameters.

correlation function, as the correlation length, which describes the characteristic length scale at which two points cannot be considered correlated any more. The roughness exponent h in the self-affine correlation function, normally ranging from 0 to 1, describes the degree of the surface roughness. Note that $h = 1$ coincides with the Gaussian profile and $h = 0.5$ would indicate exponentially rough surfaces. There is a paradox whether larger or smaller values of this exponent correspond to rougher surfaces [50]. Fig. 3.8 shows three self-affine surface profiles in (a)-(c) with similar macroscopic roughness characterized by $\sigma = 1.1 \pm 0.1$. In this case the profile with the largest roughness exponent has the smoothest texture. However, that larger exponents correspond to smoother surfaces is only valid if the surfaces are fractal and have similar macroscopic roughness. A nonfractally rough surface as depicted in Fig. 3.8 (d) would give a fitted value, $h \approx 1$. A planar surface as depicted in Fig. 3.8 (e) cannot be fitted by any value of h , implying the self-affine analysis approach is inappropriate for this kind of surfaces. The influences of the correlation length and the roughness exponent are examined in Fig. 3.9 and Fig. 3.10, respectively. As we know, a larger correlation length would mean stronger correlations between different points on the surface, thus a smoother surface. An infinitely smooth surface, corresponding to the planar surface in Fig. 3.8 would have a correlation length approaching infinity, and the correlation function in Fig. 3.9 would be a horizontal line $C(\mathbf{R}) = 1$. On the other hand, if the correlation length is fixed, as shown in Fig. 3.10, larger roughness exponents correspond to smoother surfaces if the length scale is smaller than the correlation length, and the roughness exponent rather describes the degree of roughness at small length scales, i.e., local roughness or microscopic roughness. In this range, Gaussian surfaces with $h = 1$ are the smoothest surfaces. As long as the length scale investigated becomes larger than the correlation length, smaller roughness exponents would correspond to smoother surfaces. Therefore, the paradox is resolved by taking different length scales, whether smaller or larger than the macroscopic correlation length ξ . The former is

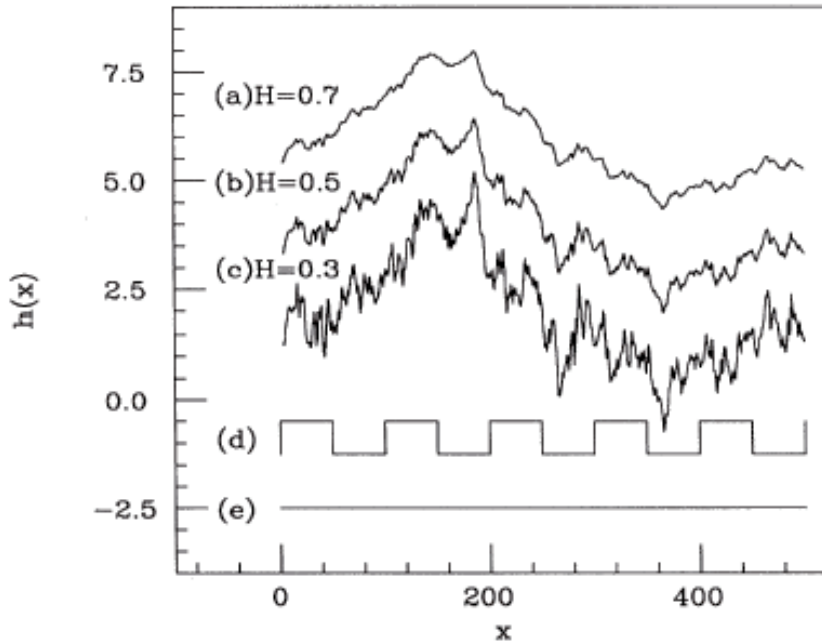


Figure 3.8: Surface profiles (a), (b) and (c) are self-affine with roughness exponents H (the same as h in our case). The self-affine profiles all have the same rms roughness $\sigma = 1.1 \pm 0.1$. (d) is a nonfractally rough surface, and (e) is a planar surface. Figure taken from ref [51].

more associated with local atomic rearrangements which can occur on the surfaces of solid materials, while the latter is more natural to capillary-wave and other phenomena associated with liquid-gas interfaces [50]. Computer simulation [52] showed that the apparent surface statistics alters from exponential to Gaussian as the surface sampling interval is varied. A surface with exponential correlations may be misrepresented as a surface with Gaussian correlations when the sampling interval is around two thirds of the correlation length. This arises because the short-range fluctuations, characteristic of the exponential surface, are not sampled. The full exponential nature of a surface will only be measured if the sampling interval is less than about one tenth of the correlation length. For sampling intervals between these two limits the surface correlation function will appear neither exponential nor Gaussian. Clearly sampling must be over many correlation lengths for the random nature of the surface to be apparent. It is therefore the ratio of the surface extent to the correlation length which determines the effective statistical sample size. In general a larger ratio is required for Gaussian surfaces than for exponential surfaces. This is because the fine-scale short-range roughness of the exponential surface ensures a reasonable statistical sample taken over a relatively small area. As will be shown in section 3.3.5, we assume the scattering function to follow the Guinier's law at small q_ρ ($= \sqrt{q_x^2 + q_y^2}$), resulting in a correlation function of Gaussian type.

3.3.4 Scattering from multiple rough interfaces

The scattering function for a single rough interface is given in eq. (3.44), which can be split into the reflectivity and diffuse scattering parts expressed in eqs. (3.45) and (3.50), respectively. Turning now to multiple interfaces, we recognize that a degree of conformal roughness implies a non-vanishing value of the correlation function [47]

$$C_{ij}(\mathbf{R}) = \langle \delta z_i(\mathbf{0}) \delta z_j(\mathbf{R}) \rangle \quad (3.59)$$

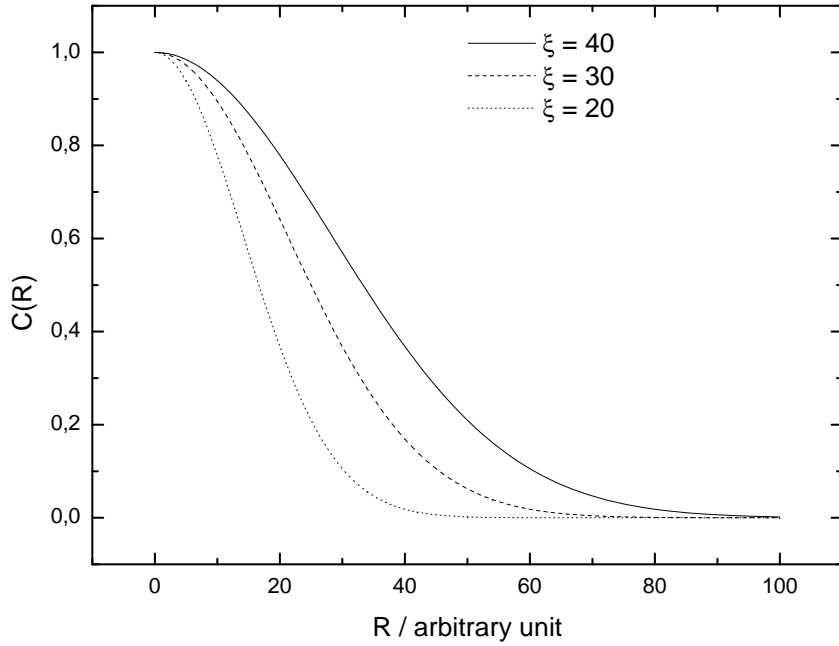


Figure 3.9: Effect of the correlation length ξ on the correlation function of Gaussian type, $C(R) = \sigma^2 \exp(-\frac{R^2}{\xi^2})$, i.e., at a fixed $h = 1$. The correlation function shown in the figure is normalized by a factor σ^2 .

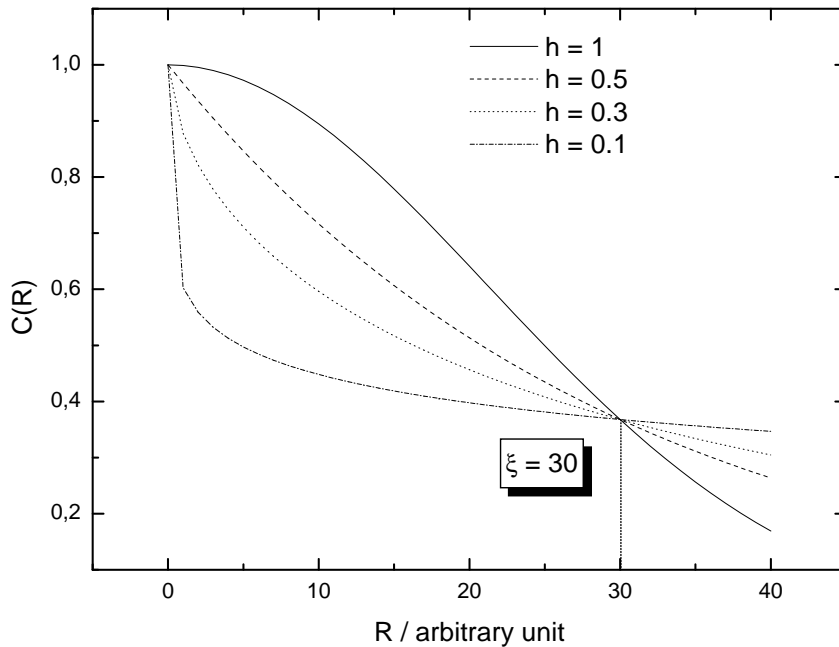


Figure 3.10: Effect of the roughness exponent h on the correlation function of self-affine type, $C(R) = \sigma^2 \exp[-(\frac{R}{\xi})^{2h}]$, at a fixed correlation length $\xi = 30$ arbitrary unit. The correlation function shown in the figure is normalized by a factor σ^2 .

which is a generalization of eq. (3.54). $\delta z_i(\mathbf{0})$ and $\delta z_j(\mathbf{R})$ are now the height fluctuations of the i -th and j -th interfaces. This effect yields the generalization of eq. (3.44) to the following form

$$S(\mathbf{q}) = \frac{A}{q_z^2} \sum_{i,j=1}^N e^{-\frac{1}{2}q_z^2(\sigma_i^2 + \sigma_j^2)} \Delta\rho_i \Delta\rho_j^* e^{iq_z(z_i - z_j)} \varepsilon_{ij}(\mathbf{q}) \quad (3.60)$$

where

$$\varepsilon_{ij}(\mathbf{q}) = \int \int dx dy e^{q_z^2 C_{ij}(\mathbf{R})} e^{-i(q_x x + q_y y)} \quad (3.61)$$

with σ_i the rms roughness of the i -th interface, $\Delta\rho_i$ the scattering contrast across it and z_i its average height. Similarly, the reflectivity from multiple rough interfaces can be separated out by subtracting 1 from the integrand of eq. (3.60), and the remaining part is the diffuse scattering function for a system composed of multiple interfaces. Note that there is usually a degree of conformality to the roughness (i.e., a correlation of the height fluctuations between different interfaces) [47]. However, we assume a perfect conformality where

$$\sigma_i = \sigma_j = \sigma \quad (3.62)$$

$$|\Delta\rho_i| = |\Delta\rho_j| = \Delta\rho \quad (3.63)$$

$$C_{ij}(\mathbf{R}) \equiv C(\mathbf{R}) \quad (3.64)$$

for our system. This assumption is justified due to the small thicknesses of the films we have used. The generalized reflectivity and diffuse scattering function for multiple interfaces with a perfect conformality can be written as

$$R(\mathbf{q}_z) = \frac{16\pi^2(\Delta\rho)^2}{q_z^4} \sum_{i,j=1}^N e^{iq_z(z_i - z_j)} \exp(-q_z^2 \sigma^2) \quad (3.65)$$

and

$$S(\mathbf{q}_\rho) = \frac{A(\Delta\rho)^2}{q_z^2} e^{-q_z^2 \sigma^2} \sum_{i,j=1}^N e^{iq_z(z_i - z_j)} \int \int dx dy [e^{q_z^2 C(\mathbf{R})} - 1] e^{-i(q_x x + q_y y)} \quad (3.66)$$

respectively. Eqs. (3.65) and (3.66) are otherwise identical to eqs. (3.45) and (3.50), except for the summation term. In the case of diffuse scattering, the scattering function shows that the q_ρ dependence of the scattering is exactly the same as that for a single rough interface, as indicated by the perfect conformality. The summation term has maxima at $q_z = 2m\pi/d_p$ ($m = \pm 1, \pm 2, \dots$) since $|z_i - z_j| = nd_p$, where d_p is the lamellar period of the structure. These maxima correspond to the Bragg peaks in reflectivity or diffuse scattering derived from the diffraction and interference between the scattered neutron beams at the multiple interfaces. The Bragg peaks extend from the case of specular reflectivity (Fig. 3.11) to the case of diffuse scattering at fixed q_z s (more precisely, the internal vector $q_{z,i}$, see section 5.1.6). The positions of the Bragg peaks fall therefore on a series of parallel planes in reciprocal space, which are called the Bragg sheets. In our experiments, we measured the reflectivity and diffuse scattering using the time-of-flight mode (see section 5.1). The reflectivity measurements correspond to the specular scan indicated by the red line with arrow in the figure. The diffuse scattering was measured at a fixed scattering angle $2\theta = 1^\circ$ with an angle of incidence ω off from the specular angle by $\Delta\omega$. These diffuse scattering measurements correspond to the longitudinal scans indicated by the blue lines with arrow. As will be shown in section 3.3.5, the scattering intensity was integrated over the y direction due to the slit geometry of our experiments. Therefore the diffuse scattering was only measured in

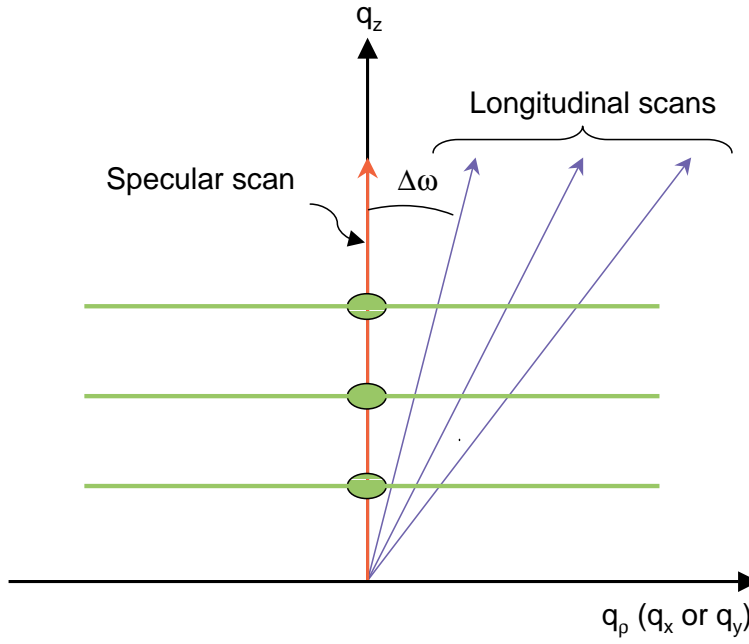


Figure 3.11: Specular and longitudinal scans used in our experiments. The horizontal green lines indicate the positions of the Bragg sheets.

the plane of incidence defined as the plane containing z and the incident wave vector \mathbf{k}_0 (Fig. 3.2). Provided the interfacial roughness is relatively small compared to the lamellar period, i.e., $q_z\sigma \ll 1$, eq. (3.66) becomes

$$S(\mathbf{q}_\rho) = A(\Delta\rho)^2 e^{-q_z^2\sigma^2} \sum_{i,j=1}^N e^{iq_z(z_i-z_j)} \iint dx dy C(\mathbf{R}) e^{-i(q_x x + q_y y)} \quad (3.67)$$

showing that the correlation function $C(\mathbf{R})$ is the inverse Fourier transform of the diffuse scattering function $S(\mathbf{q}_\rho)$ at a certain q_z .

3.3.5 Effect of slit collimation

The geometry of the slit collimation used in our experiments is shown in Fig. 3.12. The

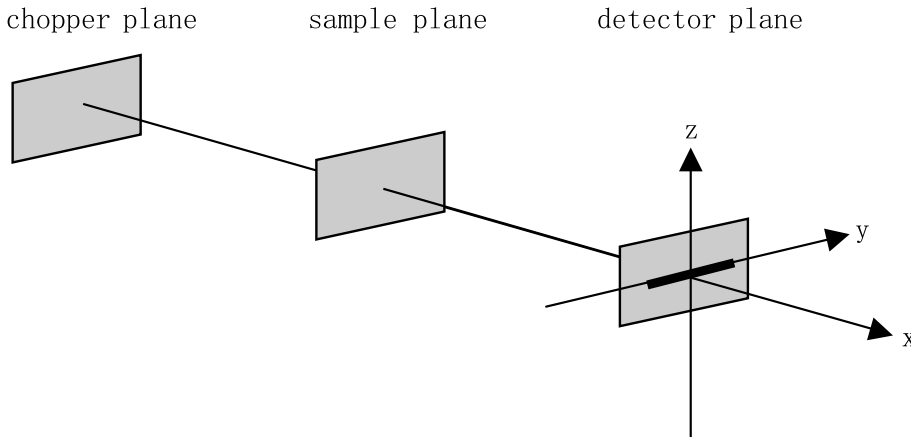


Figure 3.12: Geometry of the slit collimation system used in our neutron scattering experiments.

scattering intensity was integrated over the y direction such as

$$S^{int}(\mathbf{q}) = \int dq_y S(\mathbf{q} = (q_x, q_y, q_z)) \quad (3.68)$$

with $S(\mathbf{q})$ expressed in eq. (3.44) for a single interface or in eq. (3.60) for multiple interfaces, respectively. The measured scattering intensity is thus a function of q_z and q_x . The diffuse scattering at a fixed q_z (e.g., around the first order Bragg peak where $q_z = 2\pi/d_p$) becomes a function of q_x . The diffuse scattering function given by eq. (3.50) for a single interface will become [47]

$$S(q_x) = \frac{2\pi A (\Delta\rho)^2}{q_z^2} e^{-q_z^2\sigma^2} \int dx [e^{q_z^2 C(x)} - 1] e^{-iq_x x} \quad (3.69)$$

with

$$C(x) = \langle \delta z(0) \delta z(x) \rangle \quad (3.70)$$

Similarly, the diffuse scattering function given by eq. (3.66) for multiple interfaces with a perfect conformality will become

$$S(q_x) = \frac{2\pi A (\Delta\rho)^2}{q_z^2} e^{-q_z^2\sigma^2} \sum_{i,j=1}^N e^{iq_z(z_i - z_j)} \int dx [e^{q_z^2 C(x)} - 1] e^{-iq_x x} \quad (3.71)$$

with

$$C_{ij}(x) \equiv C(x) = \langle \delta z(0) \delta z(x) \rangle \quad (3.72)$$

The effect of the slit geometry at the small and large q_ρ limit will be discussed in the following text.

Guinier's law at small \mathbf{q}

At small q_ρ , the scattering function is assumed to follow the Guinier's law as

$$S(q_\rho) = I_0 \exp(-\xi^2 q_\rho^2) = I_0 \exp[-\xi^2 (q_x^2 + q_y^2)] \quad (3.73)$$

where ξ is the correlation length and I_0 is the extrapolated intensity to $q_\rho = 0$. Now rewrite eq. (3.67) in the following form

$$S(\mathbf{q}_\rho) = C_0 \iint dx dy C(\mathbf{R}) e^{-i(q_x x + q_y y)} \quad (3.74)$$

with

$$C_0 = A(\Delta\rho)^2 e^{-q_z^2\sigma^2} \sum_{i,j=1}^N e^{iq_z(z_i - z_j)} \quad (3.75)$$

Eqs. (3.73) and (3.74) should be equal at $q_\rho = 0$, thus we have

$$I_0 = C_0 \iint dx dy C(\mathbf{R}) \sim C_0 \sigma^2 \xi^2 \quad (3.76)$$

At small q_ρ , the scattering function can also be reduced to the Ornstein-Zernicke form as

$$S(q_\rho) \approx I_0 (1 - \xi^2 q_\rho^2) \approx \frac{I_0}{1 + \xi^2 q_\rho^2} = \frac{I_0}{1 + \xi^2 (q_x^2 + q_y^2)} \quad (3.77)$$

Performing the inverse Fourier transformation of eq. (3.74) using $S(q_\rho)$ expressed in eq. (3.73), the correlation function $C(\mathbf{R})$ can be obtained as

$$\begin{aligned}
C(\mathbf{R}) &= \frac{I_0}{(2\pi)^2 C_0} \int \int dq_x dq_y \exp[-\xi^2(q_x^2 + q_y^2)] \exp[i(q_x x + q_y y)] \\
&= \frac{I_0}{4\pi^2 C_0} \int dq_x \exp(-\xi^2 q_x^2 + i q_x x) \int dq_y \exp(-\xi^2 q_y^2 + i q_y y) \\
&= \frac{I_0}{4\pi^2 C_0} \frac{\pi}{\xi^2} \exp[-(x^2 + y^2)/4\xi^2] \\
&= \frac{I_0}{4\pi C_0 \xi^2} \exp(-R^2/4\xi^2)
\end{aligned} \tag{3.78}$$

Substitution of eq. (3.76) for I_0 in eq. (3.78) yields

$$C(\mathbf{R}) \sim \sigma^2 \exp(-R^2/4\xi^2) \tag{3.79}$$

showing that the correlation function is a Gaussian one.

Taking the effect of slit collimation into account, after integrating $S(q_\rho)$ expressed in eq. (3.73) with respect to q_y , we obtain the scattering function as

$$\begin{aligned}
S(q_x) &= \int dq_y I_0 \exp[-\xi^2(q_x^2 + q_y^2)] \\
&= I_0 \exp(-\xi^2 q_x^2) \int dq_y \exp(-\xi^2 q_y^2) \\
&= \frac{\sqrt{\pi} I_0}{\xi} \exp(-\xi^2 q_x^2)
\end{aligned} \tag{3.80}$$

showing that the correlation length enters into the prefactor of the function, and the exponent is still proportional to the square of the correlation length. Two important parameters, namely, the correlation length ξ and the extrapolated intensity I_0 , can be obtained by fitting the experimental data to eq. (3.80). The one-dimensional correlation function $C(x)$ is then calculated as

$$\begin{aligned}
C(x) &= \frac{1}{(2\pi)^2 C_0} \int dq_x S(q_x) \exp(i q_x x) \\
&= \frac{\sqrt{\pi} I_0}{(2\pi)^2 C_0 \xi} \int dq_x \exp(-\xi^2 q_x^2) \exp(i q_x x) \\
&= \frac{I_0}{4\pi C_0 \xi^2} \exp(-x^2/4\xi^2) \\
&\sim \sigma^2 \exp(-x^2/4\xi^2)
\end{aligned} \tag{3.81}$$

which is also a Gaussian function with the same roughness and correlation length as those for the two-dimensional correlation function given in eq. (3.79). From eq. (3.55) and by setting $x = 0$ in eq. (3.81), the mean square roughness σ^2 can be calculated as

$$\sigma^2 = C(0) = \frac{1}{(2\pi)^2 C_0} \int dq_x S(q_x) \tag{3.82}$$

with C_0 expressed in eq. (3.75). Eq. (3.82) shows qualitatively an increase in the interfacial roughness will lead to an increase in the diffuse scattering intensity.

Power law at large \mathbf{q}

At large q_ρ , the scattering intensity is assumed to obey a power law which has the form of

$$S(q_\rho) = I_1 q_\rho^{-\alpha} = I_1 (\sqrt{q_x^2 + q_y^2})^{-\alpha} \quad (3.83)$$

with I_1 the prefactor and α the power law exponent. If in the integral formula [53]

$$\int_{-\infty}^{+\infty} \frac{dx}{(x^2 + a^2)^n} = \frac{(2n - 3)!!}{2 \cdot (2n - 2)!!} \cdot \frac{\pi}{a^{2n-1}} \quad (3.84)$$

x and a represent q_y and q_x respectively, the scattering intensity integrated with respect to q_y will become

$$S(q_x) = \int dq_y S(q_\rho) = \int dq_y I_1 (\sqrt{q_x^2 + q_y^2})^{-\alpha} \sim \pi I_1 q_x^{-(\alpha-1)} \quad (3.85)$$

showing that the effect of slit collimation is to decrease the absolute value of α by 1, compared with that obtained from a pinhole geometry.

3.4 Small-angle scattering

The small-angle scattering technique is used to study structures of size on the order of 10 \AA or larger, by using small scattering angles, typically 2θ less than 2° . In addition to reflectivity measurements which are sensitive to structures aligned parallel to the substrate, small-angle scattering in transmission detects the structures aligned perpendicular or tilted to the substrate. Measurements at different angles of incidence allow the determination of the orientation distribution of these structures. In this section, the principle of determination of small-angle scattering patterns expected from different structures of the sample will be discussed.

3.4.1 Ewald sphere and reciprocal space

The construction of the Ewald sphere is very useful in interpreting the effect of various geometric arrangements of scattering experiments. As shown in Fig. 3.13, suppose the sample is placed at the origin O with the incident beam directed along MO, and the scattering intensity is measured in the direction OX. The corresponding scattering vector \mathbf{q} is pointing to P, if the length of MO and OX is $2\pi/\lambda$. As we change the direction OX in which the scattering intensity is measured, \mathbf{q} moves along the surface of a sphere of radius $2\pi/\lambda$ centered on M. This sphere is called the **Ewald sphere**. Measuring the intensity in all possible directions OX is in effect determining the intensity as a function of \mathbf{q} over the Ewald sphere. If the direction MO of the incident beam is changed, the Ewald sphere is rotated to a new position around the origin O. With different directions of incidence, one can determine the intensity for all \mathbf{q} within the **limiting sphere** of radius $4\pi/\lambda$ shown in Fig. 3.13. The scattering from a structure is associated with a lattice in reciprocal space which is the Fourier transform of the real space lattice characterizing the structure. In a scattering experiment, the scattering intensity will be observed only if the scattering vector \mathbf{q} coincides with one of the reciprocal lattice vectors (in the case of crystals which have well-defined reciprocal lattices). In practice, the determination of scattering patterns is to find out the intersection of the Ewald sphere and the reciprocal lattice in reciprocal space. Examples of determining the scattering patterns in our experiments will be shown in the following section.

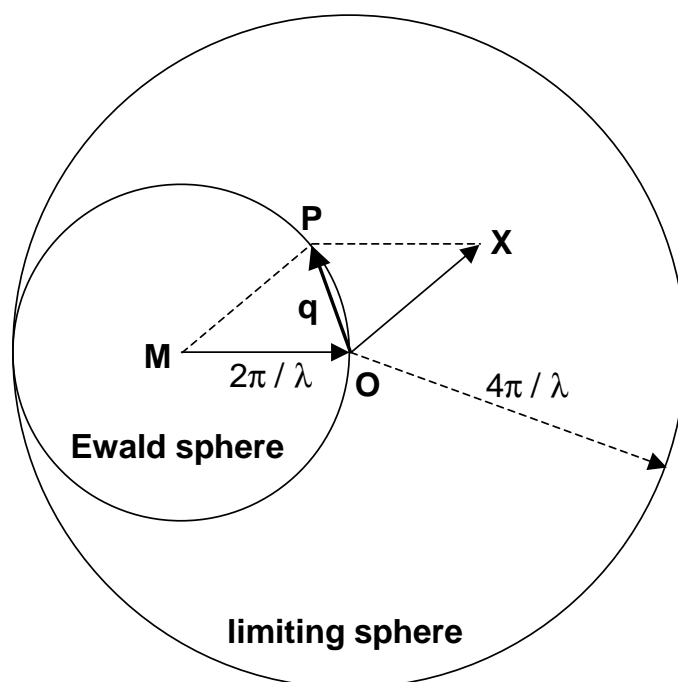


Figure 3.13: Construction of the Ewald sphere.

3.4.2 Determination of scattering patterns

The incident angle α in our small-angle scattering experiments, defined as the angle between the incident beam and the substrate normal [Fig. 3.14 (a)], can be changed from 0° to about 60° . The upper limit of the incident angle is set by the fact that the

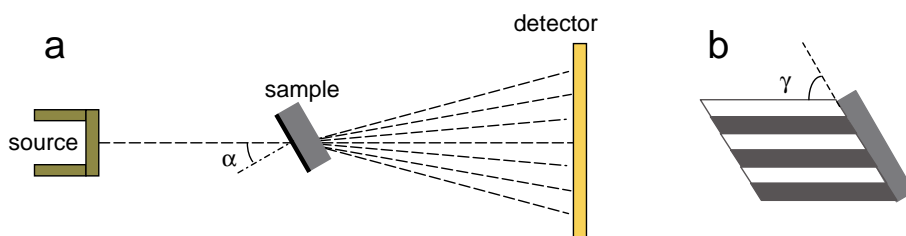


Figure 3.14: (a) Top view of the scattering geometry of our small-angle scattering experiments. (b) Schematic drawing of lamellae aligned with an inclination angle γ with respect to the substrate.

size of the primary beam is usually much larger than the thickness of the copolymer film. The reflectivity measurements complement to the small-angle scattering measurements at high angles of incidence near to 90° . As shown in Fig. 3.14 (b), the orientation of the lamellae is characterized by an inclination angle γ which is defined as the angle between the lamellar interface and the substrate surface. If $\gamma = 0^\circ$, the lamellae are oriented parallel to the substrate [Fig. 3.15 (a)]. If $\gamma = 90^\circ$, the lamellae are oriented perpendicular to the substrate. Fig. 3.15 (b) shows schematically such perpendicularly oriented lamellae with only one orientation in the plane of the film considered, i.e., the orientation perpendicular to the rotation axis of the incident angle α . In Fig. 3.15 (c)-(f), the determination of expected scattering patterns from different structures of the sample is illustrated.

As shown in Fig. 3.15 (c), in the case of a parallel orientation, the Fourier transform of the real space lattice characterizing the structure are two points along the q_z axis.

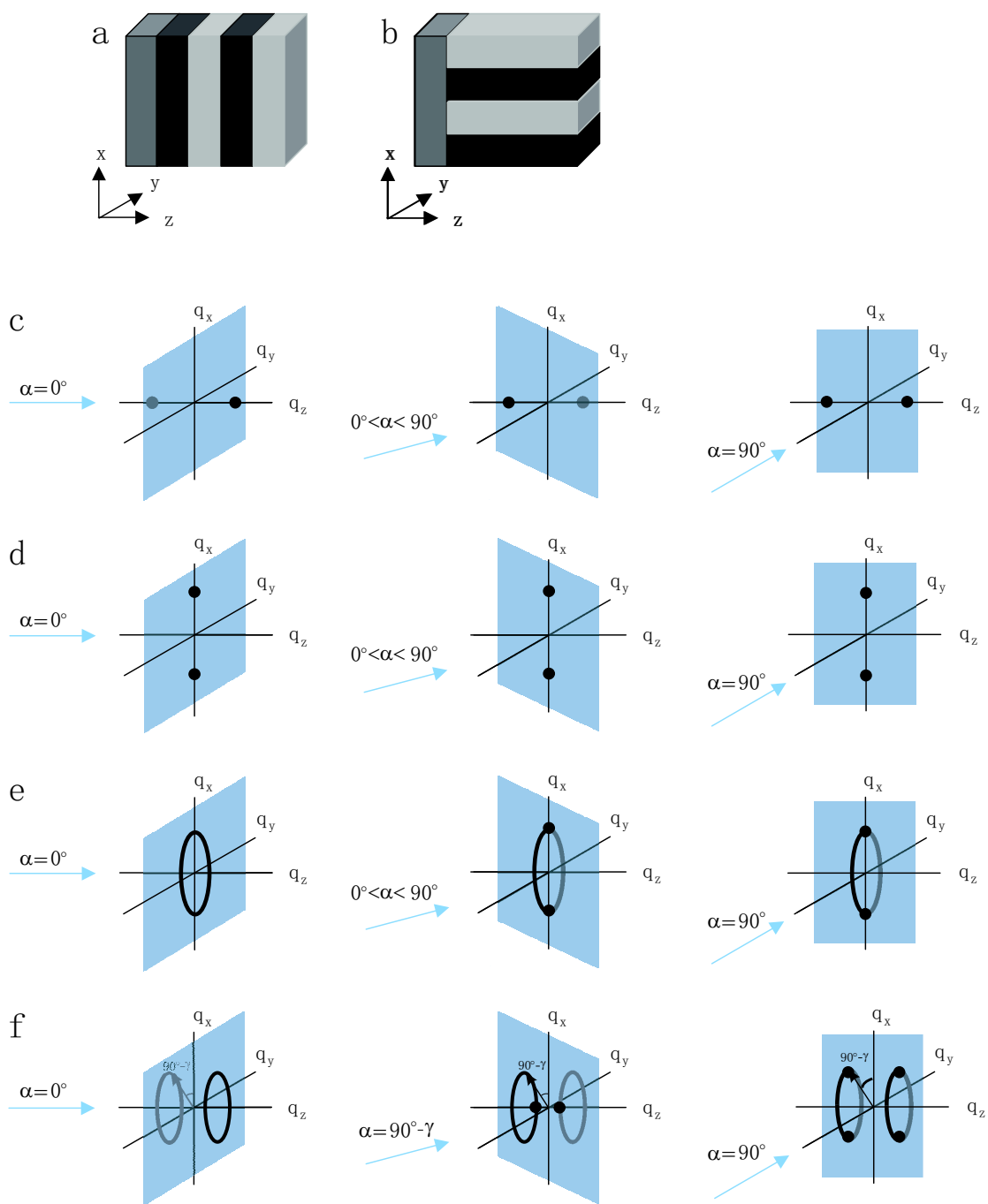


Figure 3.15: (a) and (b) are schematic drawings of lamellae oriented parallel ($\gamma = 0^\circ$) and perpendicular ($\gamma = 90^\circ$) to the substrate, respectively. In (b), only the orientation perpendicular to the rotation axis of the incident angle α is considered. (c) and (d) illustrate the determination of scattering patterns from the structures shown in (a) and (b), respectively. In (e), the scattering patterns are determined for a structure with a perpendicular orientation to the substrate but a random orientation in the plane of the film. In (f), the scattering patterns are determined for a structure with lamellae oriented at an inclination angle $0^\circ < \gamma < 90^\circ$ and randomly in the plane of the film.

The separation of each point to the origin is $|q_z| = 2\pi/d_p$, with d_p the lamellar period of the structure. In the small-angle (2θ) limit, the Ewald sphere can be regarded approximately as a flat plane through the origin, as depicted by the blue quadrangle in the figure. As the incident angle α is increased from 0° to 90° (which is unaccessible in our experiments), the intersection of the Ewald sphere and the reciprocal lattice is empty until α reaches 90° . At $\alpha = 90^\circ$, the intersection and consequently the scattering pattern will be two equatorial points.

As shown in Fig. 3.15 (d), in the case of a perpendicular orientation to the substrate and only the orientation perpendicular to the rotation axis of the incident angle α considered, the Fourier transform of the real space lattice characterizing the structure are two points along the q_x axis (the rotation axis of α). The separation of each point to the origin is $|q_x| = 2\pi/d_p$. The intersection of the Ewald sphere and the reciprocal lattice of the structure are always two meridional points.

As shown in Fig. 3.15 (e), in the case of a perpendicular orientation to the substrate and a random orientation in the plane of the film, the Fourier transform of the real space lattice can be obtained by rotating the original two points [shown in Fig. 3.15 (d)] around the origin, thus we obtain a circle of radius $\sqrt{q_x^2 + q_y^2} = 2\pi/d_p$ in the q_x - q_y plane. The intersection of the Ewald sphere and the reciprocal lattice at $\alpha = 0^\circ$ is the circle itself, resulting in a homogeneous ring in the scattering pattern. As long as α is larger than 0° , the scattering pattern will be two meridional points.

As shown in Fig. 3.15 (f), in the case of a tilted orientation with an inclination angle $0^\circ < \gamma < 90^\circ$ and randomly in the plane of the film, the Fourier transform of the real space lattice of the structure are two circles parallel to the q_x - q_y plane. No intensity is observable until α is increased to $(90^\circ - \gamma)$. At this point, the Ewald sphere hits the edges of the two circles and a scattering pattern with two equatorial points will be observed. At $(90^\circ - \gamma) < \alpha \leq 90^\circ$, a scattering pattern with four points will be observed. Therefore, structures with an inclination angle γ are only observable at an angle of incidence $\alpha \geq (90^\circ - \gamma)$. In another word, for a given α , only lamellae with inclination angles $\gamma \geq (90^\circ - \alpha)$ are observable [12].

Finally, in the case that the lamellae are oriented with a distribution around the perpendicular orientation (which is not shown in Fig. 3.15), the circle of the Fourier transform obtained in Fig. 3.15 (e) will be broadened within the scope of a sphere of radius $2\pi/d_p$ centered on the origin. The scattering pattern observed at $\alpha = 0^\circ$ will still be a homogeneous ring, while those observed at α larger than 0° will become two meridional arcs instead of two meridional points. In addition, the arcs will become shorter with increasing α . Therefore, measurements at α s allow the determination of the orientation distribution of the lamellae. As will be shown in section 6.2, the full-width at half-maximum (FWHM) of the scattering intensity plotted versus the azimuthal angle is proportional to $1/\sin \alpha$, and can be extrapolated to $\alpha = 90^\circ$ (i.e., $1/\sin \alpha = 1$). The underlying orientation distribution function (assumed Gaussian) and the orientation parameter which describes the degree of orientation can be obtained from the experiments.

Chapter 4

Sample preparation

The polystyrene-polymethylmethacrylate diblock copolymer with the PS component totally deuterated, denoted as P(dS-b-PMMA), was bought from the Polymer Standards Service GmbH ¹. The weight averaged molecular weight of the copolymer is reported as $M_w = 75000$ g/mol with a polydispersity $d = 1.08$. The weight averaged molecular weights of the PS d8 and PMMA components are both 37500 g/mol, indicating a symmetric volume fraction $f_{PS} = 0.5$. The polished silicon blocks of size 65×65 mm² and thickness 10 mm were bought from the CrysTec GmbH ². The Kapton foils of 25 μ m thick were bought from the Tricon Veredlungs GmbH ³. The Sylgard 184 silicon elastomer and curing agent were bought from the DOW CORNING ⁴.

The copolymer films were prepared by spin-coating a toluene solution of the copolymer onto the silicon substrates. All the films were then annealed in vacuum at 200 °C for 72 h. Subsequently, some of the films were annealed in a nitrogen atmosphere at the same temperature for 15 h. The purpose of the first annealing was to achieve ordered and parallel aligned lamellae in the copolymer films. The purpose of the second annealing was to apply electric fields on the samples. The experimental setup for applying an electric field is shown in Fig. 4.1. The copolymer film on a silicon substrate was covered with a Kapton foil with a thin aluminum layer coated on one side serving as the upper electrode. The silicon substrate is regarded as a conductor and can itself serve as the lower electrode. Another sheet of aluminum coated Kapton foil was attached to the other side of the silicon substrate for convenience of applying a voltage. To avoid air gaps between the upper electrode and the copolymer film, a polydimethylsiloxane (PDMS) film of about 20 μ m was introduced by spin-coating. The whole setup was kept compact under the weight of a glass plate on top. The weight of the glass plate is about 0.5 kg producing a vertical compressive stress of about 1000 Pa on the copolymer film. After each annealing step, the samples were cooled down to a temperature below the glass transition temperatures (T_{gs}) of both block components. The electric fields applied during the second annealing were switched off only after the samples were cooled down. The glass plate, the upper electrode, and the lower Kapton foil were then removed, and the copolymer films on the silicon substrates were measured by neutron scattering at the room temperature.

¹webpage: www.polymer.de

²webpage: www.crystec.de

³Address: Hausener Weg 1, 79111 Freiburg, Germany. Tel.: +49-761-49046-0

⁴webpage: www.dowcorning.com

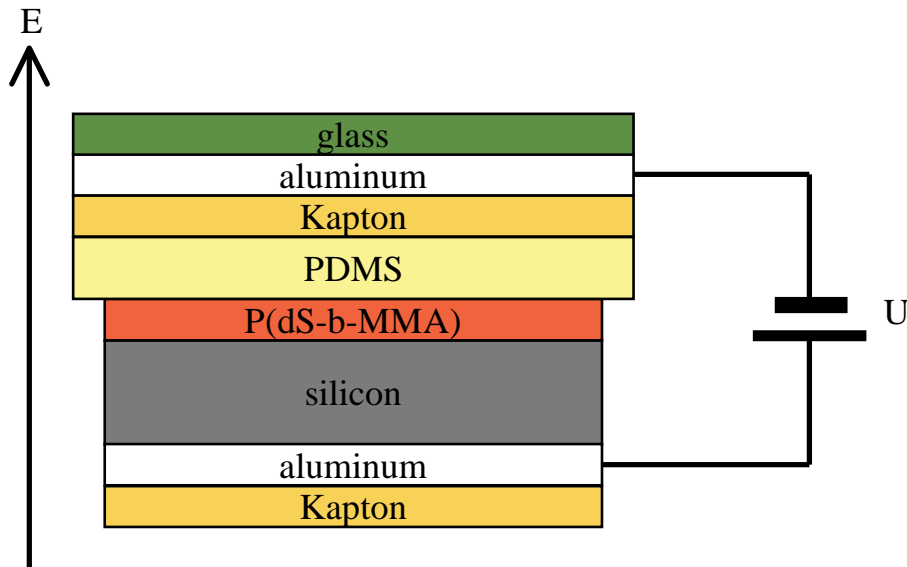


Figure 4.1: Experimental setup for applying an electric field. The glass plate on top was found necessary to keep the whole system compact and to avoid air gaps between the upper electrode and the polymer film.

4.1 Spin-coating

Toluene solutions of the block copolymer P(dS-b-MMA) were made using a mass ratio of the solute and the solvent 4% or 10%, respectively, and shaken on the shaking machine for 3 days before use. The copolymer films were then prepared by spin-coating the toluene solutions onto the silicon substrates. These substrates can be re-used after being washed using the procedure shown in Fig. 4.2. The procedure involves:

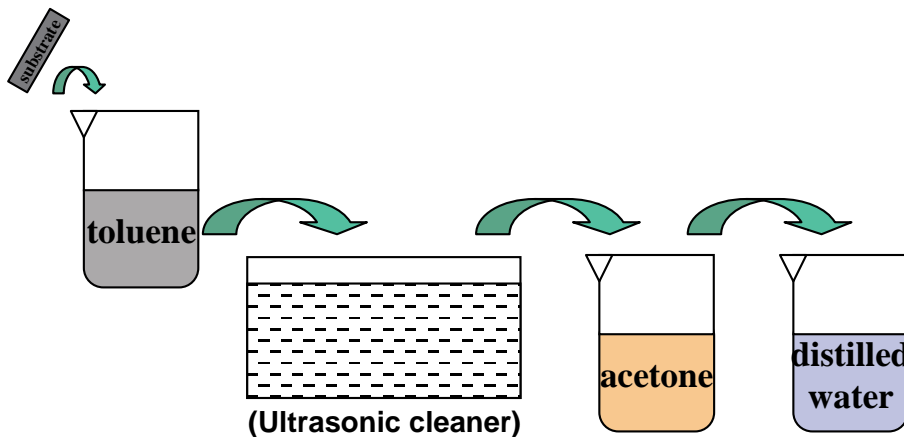


Figure 4.2: Illustration of the procedure of washing used silicon substrates.

- Put the used substrate into toluene solvent filled in a beaker and put the beaker into an ultrasonic cleaner filled with water;
- Switch on the ultrasonic cleaner to wash the substrate in the toluene solvent for 10 min;
- Take the substrate out and drip the remaining toluene onto a piece of clean paper;
- Put the substrate into acetone solvent filled in a beaker and keep it for 10 min;

- Take the substrate out of acetone and put it into distilled water filled in a beaker;
- Take the substrate out of water and clean the remaining water by snow-jet.

The silicon substrates were cleaned up by snow-jet (high-pressured CO₂ gas flux) and placed on the center of the stage of a PWM32 spin-coater bought from the Headway Research, Inc.⁵ The toluene solutions of the copolymer were then dropped onto the substrates and the copolymer films were made using a spin-speed of 750 rotations per minute (rpm) for 1 min.

The polydimethylsiloxane (PDMS) films serving as buffer layers (Fig. 4.1) were made by spin-coating a mixture of the Sylgard 184 silicon elastomer and the curing agent onto the Kapton foils. Ten shares of the silicon elastomer and one share of the curing agent (cross-linking agent) were mixed and the mixture was stirred using a magnet for 1 h. Here it requires some technical details. The mixtures must be kept very clean and without bubbles. For this reason, the magnet was cleaned by acetone, distilled water and clean paper before being put into the mixture. The rotation speed of the magnet should be set as low as possible to avoid air bubbles generated during stirring. The mixture dropped onto the Kapton foil will spread out, therefore it is enough to cover only 1/3 diameter of the foil by the mixture. Waiting for 5-10 minutes before spin-coating will effectively remove the remaining air bubbles in the mixture. The PDMS films were then made using a spin-speed of 2000 rpm for 1 min. The films directly after spin-coating (uncross-linked) need to be cured at 110 °C for 4 h to become solid (cross-linked).

4.2 Thickness measurements

The thicknesses of the copolymer films were determined using a profile meter in the Max-Planck Institute for microstructure physics⁶. The film thickness depends on the concentration of the toluene solution and the speed of spin-coating. For the speed of 750 rpm we have used, the toluene solution with a concentration of 4% or 10% yields a film thickness of 0.26 μm or 0.86 μm, respectively. The thickness of the Kapton foils was checked by a digital caliper to be 25 μm. The thicknesses of the PDMS films were also measured by the digital caliper to be 15-20 μm under the preparation conditions we have used (table 4.1).

spin-speed/rpm	spin-time/s	$d_{\text{PDMS}}/\mu\text{m}$
2000*	60	15-20
2000	180	15
5000	60	10

Table 4.1: Thicknesses of the PDMS films depending on the preparation conditions of spin-coating (speed and time). The condition denoted by the superscript * indicates the conditions we have chosen for our experiments.

Once the thicknesses of the P(dS-b-MMA) film, the PDMS film and the Kapton foil are known, the voltage needed for a certain electric field applied during the second annealing can be calculated from the thicknesses and the dielectric constants of these dielectric layers between the two electrodes (Fig. 4.1). If the layers are denoted by a

⁵webpage: www.headwayresearch.com

⁶webpage: www.mpi-halle.de

subscript i with $i = 1$ representing the copolymer film, $i = 2$ representing the PDMS film, and $i = 3$ representing the Kapton foil, we have

$$\varepsilon_i E_i = \varepsilon_j E_j \quad (4.1)$$

where E_i is the electric field in layer i with a thickness d_i and a dielectric constant ε_i . The total voltage between the electrodes is

$$U = \sum_{i=1}^3 E_i d_i \quad (4.2)$$

The strength of the electric field in the copolymer film is then given by

$$E_1 = \frac{U}{d_1 + \frac{\varepsilon_1}{\varepsilon_2} d_2 + \frac{\varepsilon_1}{\varepsilon_3} d_3} \quad (4.3)$$

Using $d_1 = 0.26 \mu\text{m}$, $d_2 = 20 \mu\text{m}$, $d_3 = 25 \mu\text{m}$, and the dielectric constants shown in table 6.9 (here for the copolymer P(dS-b-MMA) we took the average value of those for the two block components, i.e., $\varepsilon_1 = 3$), we calculate the voltage U needed for $E_1 = 1 \text{ V}/\mu\text{m}$ as ⁷

	PS	PMMA	PDMS	Kapton
dielectric constant ε	2.49-2.55 [54]	3.6 (50 Hz, 25 °C) [54]	2.75	3.4

Table 4.2: Dielectric constants of different dielectric layers between the upper and lower electrodes.

$$U_{E_1=1 \text{ V}/\mu\text{m}} = U_1 + U_2 + U_3 = 0.26 \text{ V} + 21.8 \text{ V} + 22 \text{ V} \approx 44 \text{ V} \quad (4.4)$$

Eq. (4.4) shows that the portion of the applied voltage directly falling on the copolymer film is very small. The total voltage needed for an electric field E is

$$U_{E_1=E} = U_{E_1=1 \text{ V}/\mu\text{m}} \cdot \frac{E}{1 \text{ V}/\mu\text{m}} \quad (4.5)$$

4.3 First annealing

The initial order of the microphase structures was found to play an important role on the microscopic mechanism of the electric-field-induced alignment [21]. Many previous studies [5, 6, 7, 8, 9, 10] were based on a poorly ordered initial state which can be obtained directly after spin-coating [31]. Our present study is based on an ordered and aligned initial state, which will be an interesting and complementary study to the previous ones. The purpose of the first annealing step was to induce such microphase separated lamellar structures and align these lamellae parallel to the substrate, although it turned out that a parallel orientation throughout the film can only be achieved in the thinner films of $0.26 \mu\text{m}$.

The annealing temperature should be above the glass transition temperature T_g and below the order-disorder transition temperature T_{ODT} of the block copolymer. In

⁷If the measured $\varepsilon_{\text{PMMA}}$ at $205 \text{ }^\circ\text{C}$ is used, $\varepsilon_{\text{PMMA}} = 6$ (see section 6.4.3), ε_1 becomes 4.25, and $U_{E_1=1 \text{ V}/\mu\text{m}}$ becomes $\sim 62 \text{ V}$. This indicates that the field strength is smaller with a factor ~ 1.4 than what is expected when applying a voltage calculated from eq. (4.5). However, eq. (4.5) is still used in our presentation, since $\varepsilon_{\text{PMMA}} = 3.6$ is commonly used in the literature.

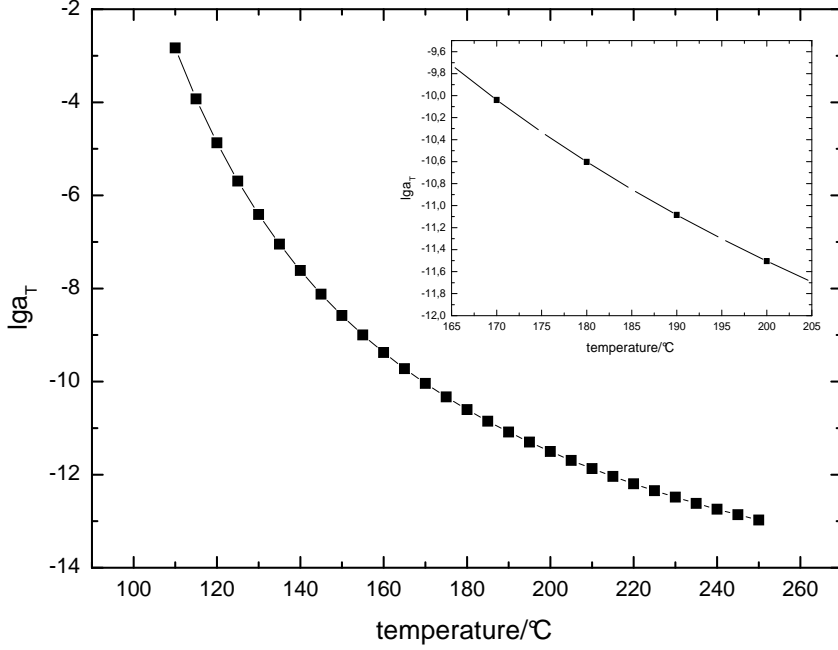


Figure 4.3: Shift factor $\log a_T$ calculated from the WLF equation plotted as a function of temperature. The inset in the figure is an enlargement of part of the main figure.

a phase separated diblock copolymer system, two T_g s which are very close to those for the corresponding homopolymers exist. The T_g s of homopolymers PS and PMMA are 373 K (or 100 °C) and 378 K (or 105 °C) [55], respectively, at a sufficiently high molecular weight. The T_{ODT} for the copolymer we used was not measured, but from those reported [56] for other symmetric PS-PMMA block copolymers with lower molecular weights, it can be inferred that the T_{ODT} for our copolymer is well above 251 °C. (For their samples with a molecular weight of 37000 g/mol and 31000 g/mol, the T_{ODT} s were 251 °C and 182 °C, respectively.) The determination of the annealing temperature should also be a compromise between shorter annealing time (requiring not too low temperature) and less degradation of the copolymer (requiring not too high temperature).

The annealing time needed for well-ordering depends on the mobility of the copolymer melt. The viscosity of a polymer melt decreases with temperature by a shift factor $\log a_T$ given by

$$\log \frac{\eta(T)}{\eta(T_g)} = \log a_T \quad (4.6)$$

where $\eta(T)$ and $\eta(T_g)$ are the viscosities at temperatures T and T_g , respectively. The shift factor $\log a_T$ can be described by the Williams-Landel-Ferry (WLF) equation

$$\log a_T = \frac{-C_1(T - T_g)}{C_2 + (T - T_g)} \quad (4.7)$$

where C_1 and C_2 are empirical constants. The shift factor $\log a_T$ calculated from eq. (4.7) is plotted in Fig. 4.3 as a function of temperature. Here we take $T_g = 100$ °C, $C_1 = 17.44$, and $C_2 = 51.6$. In the inset, it shows that the viscosity decreases by a factor 3.5 from 170 °C to 180 °C, and a factor 10 from 170 °C to 190 °C. The tendency to increase the mobility of the sample becomes less at higher temperatures. After several tests, the annealing temperature was chosen to be 200 °C. At this temperature, an annealing time of 72 h is enough for the samples to be ordered. In the films of 0.26 μm ,

a stepwise change in color (or a sharp contrast at the boundaries of regions with different colors) was observed under microscope (Fig. 4.4). This stepwise change in color is an

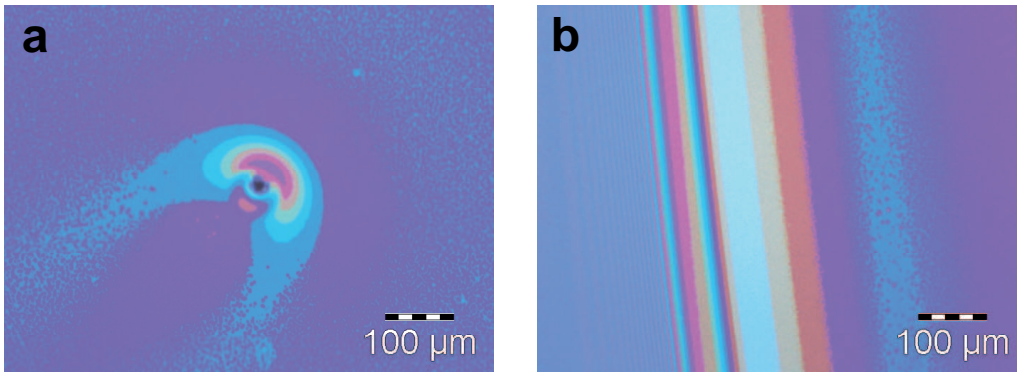


Figure 4.4: Optical micrographs taken from (a) the central part and (b) the edge of the P(dS-b-MMA) films of $0.26 \mu\text{m}$ thick, after annealed in vacuum at 200°C for 72 h. The stepwise change in color indicates a completely parallel orientation of the lamellae induced by the surface effects.

indication of a stepwise change in thickness [57] due to the request of commensurability of the film thickness with the lamellar period of the structure, therefore indicates a completely parallel orientation of the lamellae induced by the surface effects (see section 2.2).

4.4 Second annealing

The second annealing step with the application of electric fields was performed at the same temperature, i.e., 200°C , for 15 h. Here the vacuum was replaced by a nitrogen atmosphere in order to avoid an electric short circuit under high voltages. An inhomogeneous electric field will lead to the dewetting of a polymer film [58]. Although the applied voltage in our experiments was uniform, air gaps between the upper electrode and the copolymer film will lead to such an inhomogeneity in the electric field. Fig. 4.5 (a) shows the surface structure of a dewetted polystyrene film dewetted in our test experiments, while Fig. 4.5 (b) shows an example of the islands and holes structures observed in several of our copolymer films. These islands and holes structures appear-

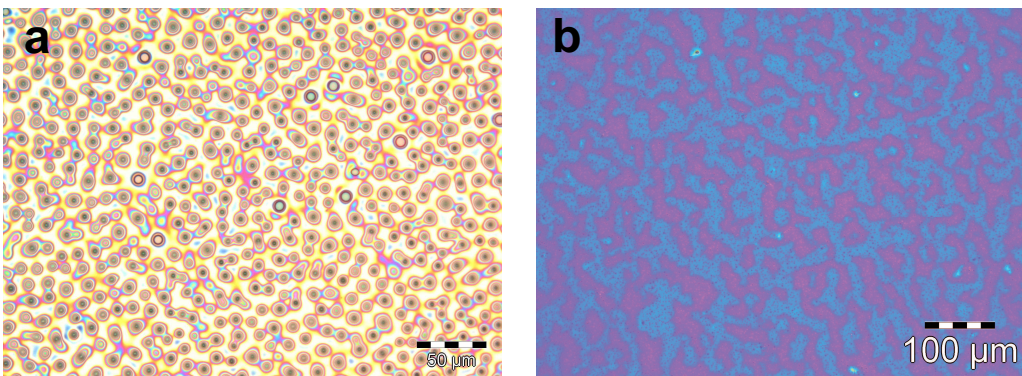


Figure 4.5: Optical micrographs for: (a) a dewetted PS film structure, and (b) islands and holes structure in P(dS-b-MMA) films.

ing either after the first annealing or after the second annealing, is an indication of

a lamellar orientation parallel to the substrate. The part of the film containing such structures appear rougher than the other part of the film. In contrast to the case shown in Fig. 4.5 (a), the film is not destroyed, and it is not necessary to avoid the islands and holes structures in the experiments.

Two reasons are responsible for the formation of air gaps between the upper electrode and the copolymer film in our sample preparation. One is the remaining solvent, air or water absorbed in the sample, which will evaporate upon pumping or heating above the boiling points of these materials. The amount of the remaining solvent should be already very small after the first annealing. The air absorbed by the sample (which is already in a gaseous state) will only expand its volume by a factor of 2-3 upon heating in the temperature range we used, while the water absorbed in the sample will undergo a transition from the liquid state to the gaseous state and therefore expands its volume by a thousand times. Consequently, the water absorbed in the sample is probably the main reason for the formation of this type of air gaps. The solution to avoid this type of air bubbles was to keep the sample in vacuum for 24 h (room temperature) so that the remaining water in the sample will be effectively removed. The other type of air gaps were formed due to the deformation of the upper electrode upon heating. The upper electrode (Kapton in material) deforms upon heating because it has a different thermal expansion coefficient from that of the film substrate (silicon in material). Small gaps are formed on the edges between them and the air (nitrogen in this case) goes inside through the gaps. A mechanical force was found effective to prevent the upper electrode from deforming upon heating. This mechanical force was achieved by placing a piece of glass with flat surface on top of the upper electrode (Fig. 4.1). The size of the glass should be larger than that of the copolymer film so that it is able to cover the whole area of the film. In our experiments, the weight of the glass plate was about 0.5 kg, exerted on an area of $65 \times 65 \text{ mm}^2$, producing a vertical compressive stress

$$P = \frac{5 \text{ N}}{(65 \times 10^{-3} \text{ m})^2} \approx 1200 \text{ Pa} \quad (4.8)$$

on the copolymer film.

In order to achieve a better contact between the upper electrode and the copolymer film, a polydimethylsiloxane (PDMS) film was introduced in between them for its good flexibility. Moreover, the contact will be much better improved if the contacting procedure is done in vacuum. This was done under the help of a self-designed contacting device ⁸ (Fig. 4.6) using the principle of magnetic forces generated from constant electric currents through electromagnetic coils. The flexible Kapton foil was supported by a thin silicon wafer with the PDMS film on the other side of the foil. A small piece of iron was pasted onto the silicon wafer to hold the latter by the magnetic force generated when the electric current was switched on. The electric current is usually around 0.2 A. The copolymer film was placed below at a small distance. The whole setup was kept in vacuum. When the electric current was switched off, the Kapton foil with the PDMS film fell down onto the copolymer film. As the contacting procedure was finished in vacuum, the upper electrode was perfectly in compliance with the surface of the copolymer film, and the contact was much better improved. The setup was taken out of the vacuum oven, and a constant voltage needed for a desired electric field E as calculated from eq. (4.5) was then applied. A high voltage power supply with the upper limit of $\sim 2000 \text{ V}$ served as this purpose. The applied electric field was checked with a multimeter, and then switched off (to avoid an electric short circuit in the following vacuum)

⁸This device was designed by Stefan Hugger, a Ph. D student who was formerly in our group and is currently in the Physics Department of University of Düsseldorf.

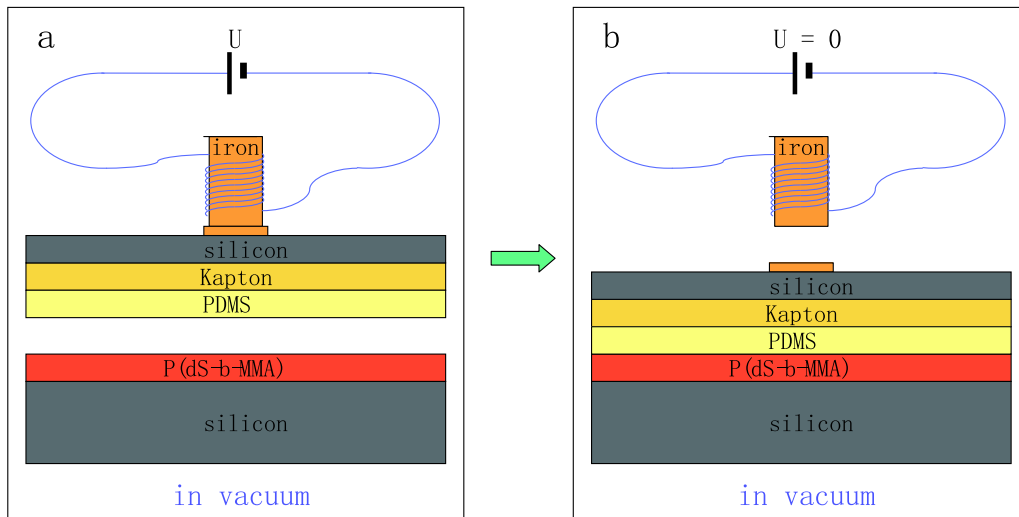


Figure 4.6: Illustration of the working principle of the self-designed contacting device. For details, see the text.

for the moment. The whole setup for applying an electric field (Fig. 4.1) was put into the oven again. A 5 min pumping led to a vacuum in the oven, and then the nitrogen was ventilated into the oven from a high-pressured bottle until the pressure in the oven was around 800 mBar. The desired electric field was switched on again. Afterwards the sample was heated up to 200 °C, and annealed at this temperature for 15 h. The electric field was switched off after the sample was cooled down to a temperature below the T_g s of both block components.

Chapter 5

Instruments

The neutron scattering experiments were performed at the Swiss Spallation Neutron Source (SINQ) ¹ in the Paul Scherrer Institute (PSI). In a spallation neutron source, neutrons are produced by a highly accelerated proton beam hitting on a heavy metal target. The present target at SINQ is an array of lead rods, hit by a proton beam with an energy of 590 MeV ². The atoms in the highly excited target release their internal energy primarily by “evaporating” neutrons. The neutrons which are released from the target at a speed of about 20000 km/s (or 2.1 MeV) is much too fast for our purpose. Cold neutrons with a speed of about 700 m/s (or 2.6×10^{-3} eV) obtained in a moderator tank filled with light water (H₂O) were used in our experiments. These cold neutrons have a wavelength on the order of Å, directed in a special super-mirror (referred to as “neutron guides”) to individual beamlines (instruments). Although they are produced by spallation, the neutrons directed by the neutron guides from the source can be considered as continuous, because the accelerator has duty cycles of 51 MHz [59].

The reflectometers AMOR and MORPHEUS, and the small-angle neutron scattering instrument SANS-II were used in our experiments in combination. The working geometries of these instruments are different and will be discussed in the following sections respectively. However, the design for the detectors is relatively the same which can be discussed together. Generally, neutron detectors are devices in which absorption of a neutron generates a short electric pulse in the associated electric circuit. By counting the rate of generation of such pulses, the flux of the neutron beam can be measured. The detector is usually filled with ³He which, upon absorbing a neutron produces high energetic particles through the nuclear reaction [43]



These energetic particles induce further secondary ionization in the gas resulting in an amplification in the electric pulse signal. For the reflectometers AMOR and MORPHEUS a ³He single detector is used, and for the instrument SANS-II a ³He area (two dimensional) position-sensitive detector is used.

5.1 Time-of-flight reflectometer AMOR

A sketch of the overall instrumental setup of the time-of-flight mode reflectometer AMOR is shown in Fig. 5.1. In a neutron scattering experiment, the scattering in-

¹website: sinq.web.psi.ch

²<http://asq.web.psi.ch/ASQ/facilities/SINQSYSTEMS.html>

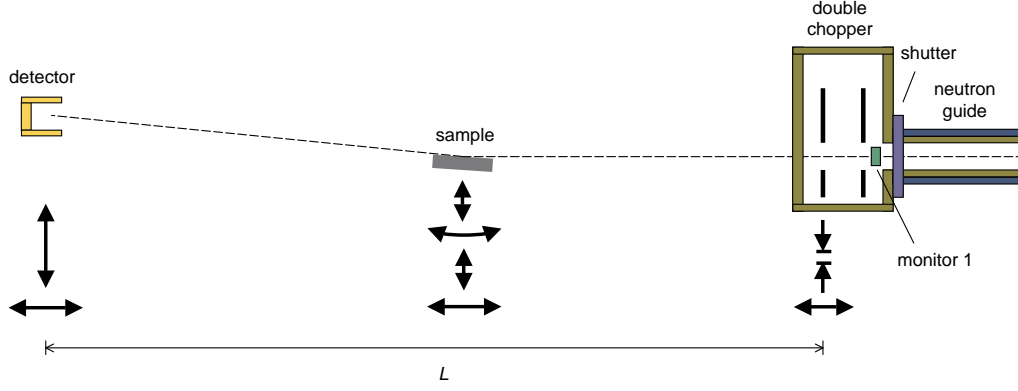


Figure 5.1: Sketch of the overall instrumental setup of the time-of-flight mode reflectometer AMOR at SINQ.

tensity is measured as a function of scattering vector q , which is given by

$$q = \frac{4\pi}{\lambda} \sin \frac{(2\theta)}{2} = \frac{4\pi}{\lambda} \sin \theta \quad (5.2)$$

where λ is the wavelength of the incident neutron beam, and 2θ is the scattering angle defined as the angle between the incident and scattered wave vectors (Fig. 3.2). The incident angle ω is equal to θ (half of 2θ) for a specular reflection, while $\omega \neq \theta$ for an off-specular diffuse scattering. Depending on the way to obtain different q -values, by varying either 2θ or λ , two common modes (the monochromatic and time-of-flight modes) are used in scattering methods. In the monochromatic mode, the wavelength of the incident beam is selected as a single wavelength by the monochromator, while the incident and scattering angles are varied simultaneously. In the time-of-flight mode, the scattering angle is fixed, while a white neutron beam with multi-wavelengths is used as the incident beam. The continuous white neutron beam is pulsed by a chopper (see section 5.1.1). The wavelength of a scattered neutron can be obtained from the time t needed by it to fly from the chopper to the detector, because neutrons with different wavelengths possess different speeds so that they arrive at the detector at different times. The detector starts to count time zero when the pulse starts, and stores the counts of neutrons arriving at different times in an electronic memory which is divided into several hundred time channels. The wavelengths of these scattered neutrons are calculated as

$$\lambda = \frac{h}{p} = \frac{h}{mv} = \frac{ht}{mL} \quad (5.3)$$

where $h = 6.626 \times 10^{-34}$ J s is the Planck's constant. p , m and v are the momentum, mass and velocity of the neutron, respectively. L is the distance from the chopper to the detector. Substituting eq. (5.3) into eq. (5.2) we obtain the scattering vector as

$$q = \frac{4\pi mL \sin \theta}{ht} \quad (5.4)$$

Fig. 5.2 shows the result of the time-of-flight mode measurement from the sample PSI08 (table 5.1). In Fig. 5.2 (a), the counts in the primary beam $N_{pr}(q)$ and the scattered beam $N_{sc}(q)$ are shown as a function of q . The reflectivity $R(q)$ can be obtained simply from the quotient

$$R(q) = \frac{N_{sc}(q)}{N_{pr}(q)} \quad (5.5)$$

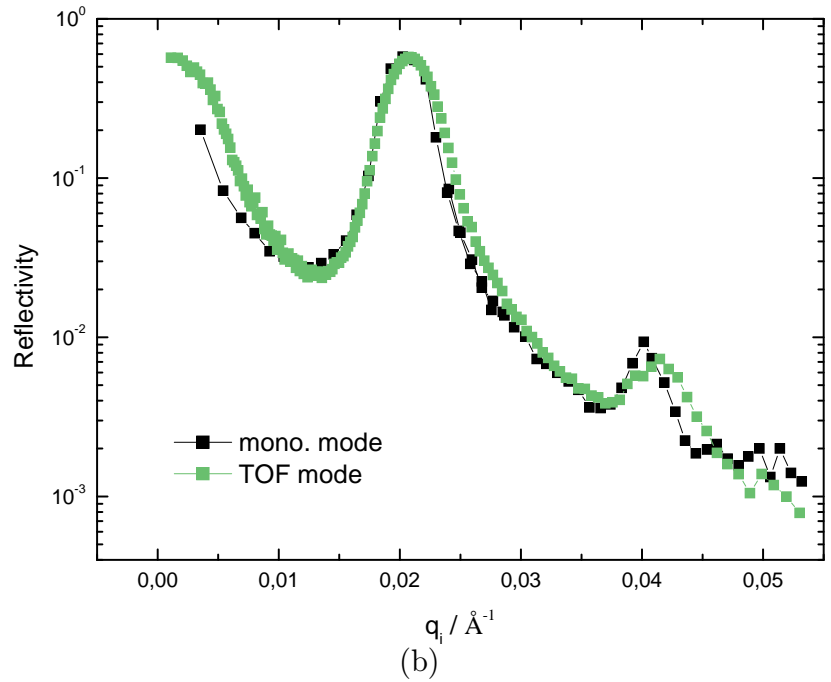
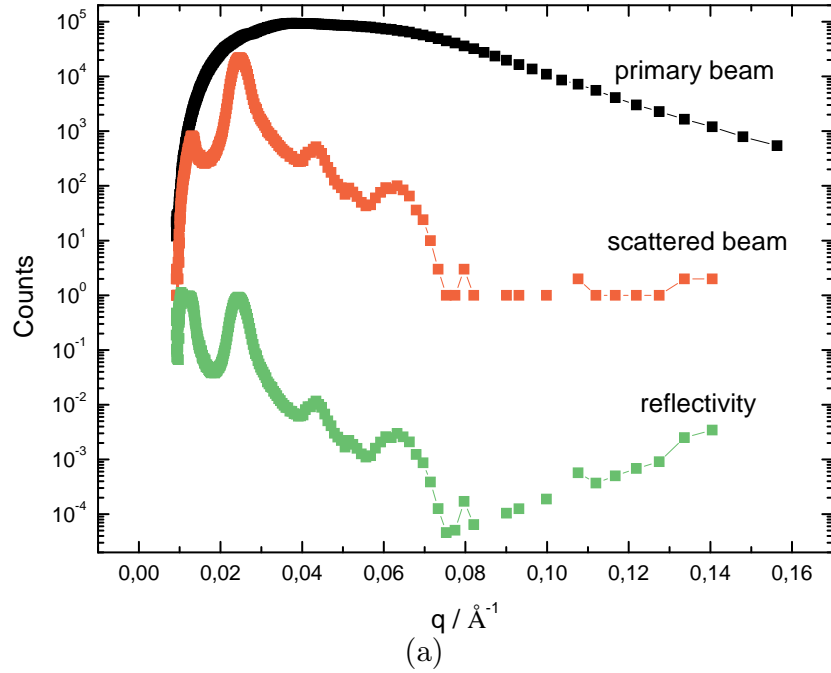


Figure 5.2: (a) Time-of-flight measurements of the primary beam and the scattered beam from the sample PSI08 ($d = 1 \mu\text{m}$, $E = 2 \text{ V}/\mu\text{m}$), measured at a chopper speed of 1000 rpm and a phase difference of $+11^\circ$ between the two chopper disks. The reflectivity is obtained from the quotient of the scattered counts by the counts in the primary beam. (b) Comparison of reflectivity obtained from the time-of-flight mode measurement with that obtained from the monochromatic mode measurement on the same sample.

sample	$d/\mu\text{m}$	annealing procedure
PSI08	1	(i) in vacuum at 200 °C for 72 h; (ii) in N ₂ at 200 °C for 15 h with $E = 2 \text{ V}/\mu\text{m}$
AUG04C	0.86	(i) in vacuum at 200 °C for 72 h; (ii) in N ₂ at 200 °C for 15 h with $E = 1 \text{ V}/\mu\text{m}$

Table 5.1: List of samples used in this chapter, with d the thickness of the sample and E the strength of the applied electric field.

The resulting reflectivity obtained from the time-of-flight measurement is compared with that obtained from the monochromatic measurement in Fig. 5.2 (b), showing an agreement with the latter in the whole q -range measured here. In the time-of-flight mode, a large portion of the neutrons initially available in the continuous source are blocked by the chopper and wasted. However, the advantages of the time-of-flight mode include: (i) a large q -range can be obtained without moving the sample or the detector; (ii) the area of the sample illuminated by the incident beam remains fixed; (iii) the whole scattering curve can be obtained simultaneously which makes the measurements feasible in reality.

5.1.1 Chopper

The chopper is an important part of the time-of-flight mode reflectometer. The chopper we used here is composed of two rotating disks as shown in Fig. 5.3. The disks are

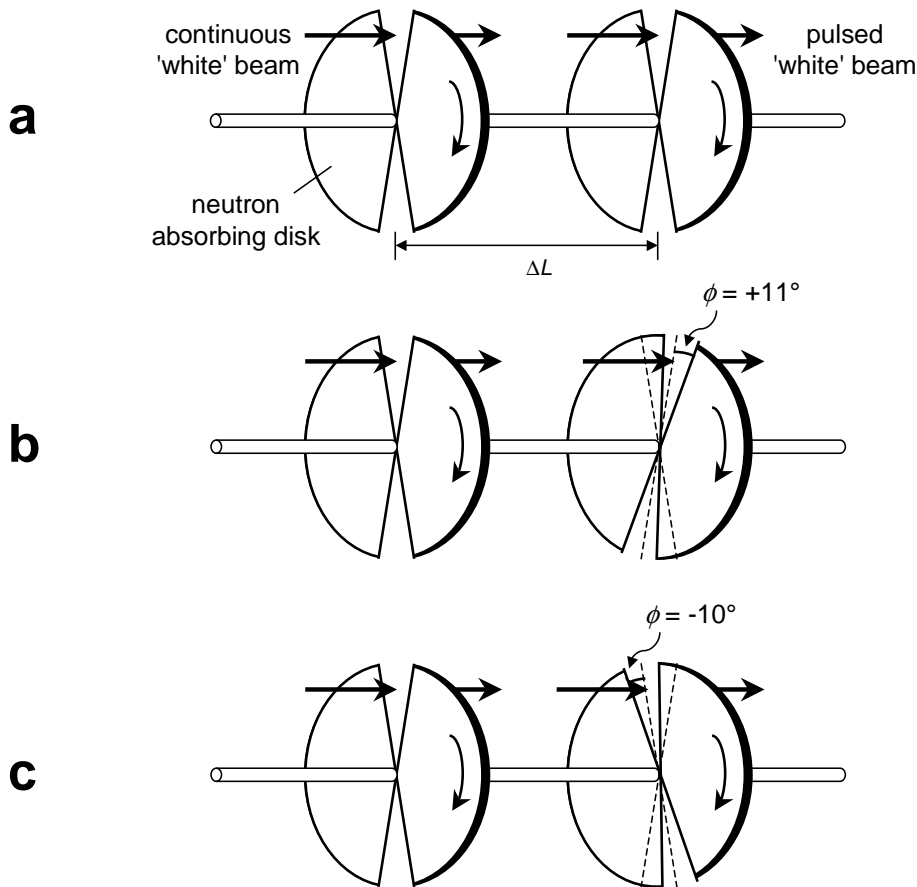


Figure 5.3: Illustration of the chopper device used to pulse a continuous white neutron beam. (a) a zero phase delay, (b) a positive phase delay, and (c) a negative phase delay.

opaque to neutrons, and rotate at the same speed around the same axis parallel to the neutron beam. The sectorial openings in the first disk periodically chops the continuous neutron beam, yielding a pulse of white neutrons. Neutrons within the pulse arrive at the second disk at different times according to their velocities. The openings in the second disk allows only neutrons of a velocity high enough to pass through the distance between the two disks within a time for the disks to rotate by an angle of the sectorial opening window. A desired variable opening time can be provided by introducing an adjustable phase delay between the two chopper disks. If we look from such a direction that the chopper is rotating clockwise, a positive phase ϕ means the second disk is rotated clockwise by an angle ϕ with respect to the first one, and a negative phase means the second disk is rotated anticlockwise.

Fig. 5.4 shows the influence of different chopper phases on the primary beam and the resulting reflectivity measurements. The primary beam [Fig. 5.4 (a)] consists of neutrons with wavelengths from $\sim 1 \text{ \AA}$ to $\sim 10 \text{ \AA}$ with a maximum flux at around 2-3 \AA . As can be seen from Fig. 5.3, slow neutrons with large wavelengths are allowed to go through in the case of a negative chopper phase, while these slow neutrons are more cut off in the case of a positive chopper phase. These slow neutrons are sometimes so slow that they arrive at the detector at the same time as that for the fast neutrons from the next pulse. Therefore the counts of these slow neutrons are added to the counts of the fast neutrons, giving rise to the intensity of fast neutrons with wavelengths smaller than 1 \AA in the spectrum of the primary beam measured at a chopper phase -11° . This so-called “frame overlap” problem will result in a high background in the reflectivity [Fig. 5.4 (b)] at large q . On the other hand, the counts of slow neutrons are significantly reduced in the case of a positive phase $+10^\circ$. The reduction of the counts of slow neutrons will result in a bad statistics in the reflectivity at small q . To compromise these two situations, a positive chopper phase $+8.8^\circ$ was used in the third case, giving rise to a reflectivity curve with compromised good statistics at small q and low background at large q .

5.1.2 Frame overlap

The criterion to avoid the “frame overlap” problem can be written as

$$t_{s,n} = t_{f,n+1} \quad (5.6)$$

where $t_{s,n}$ and $t_{f,n+1}$ denote the times-of-flight needed by the slowest neutrons from the n th pulse and the fastest neutrons from the $(n+1)$ th pulse. If the time interval between two successive pulses is t_{pul} , the criterion in eq. (5.6) becomes

$$\frac{L}{v_s} = \frac{L}{v_f} + t_{pul} \quad (5.7)$$

where L is the distance from the chopper to the detector, and v_s and v_f are the velocities of the slowest and fastest neutrons respectively. Neutrons of a velocity $v < v_s$ should be cut off to avoid the “frame overlap” problem. If ΔL is the distance between the two chopper disks, the time needed by neutrons of a velocity v_s to travel from the first to the second chopper disk can be calculated as

$$\Delta t = \frac{\Delta L}{v_s} \quad (5.8)$$

During this time Δt , the chopper will be rotated by an angle

$$\delta = 360^\circ \cdot v_r \cdot \Delta t = 360^\circ \cdot v_r \cdot \frac{\Delta L}{v_s} \quad (5.9)$$

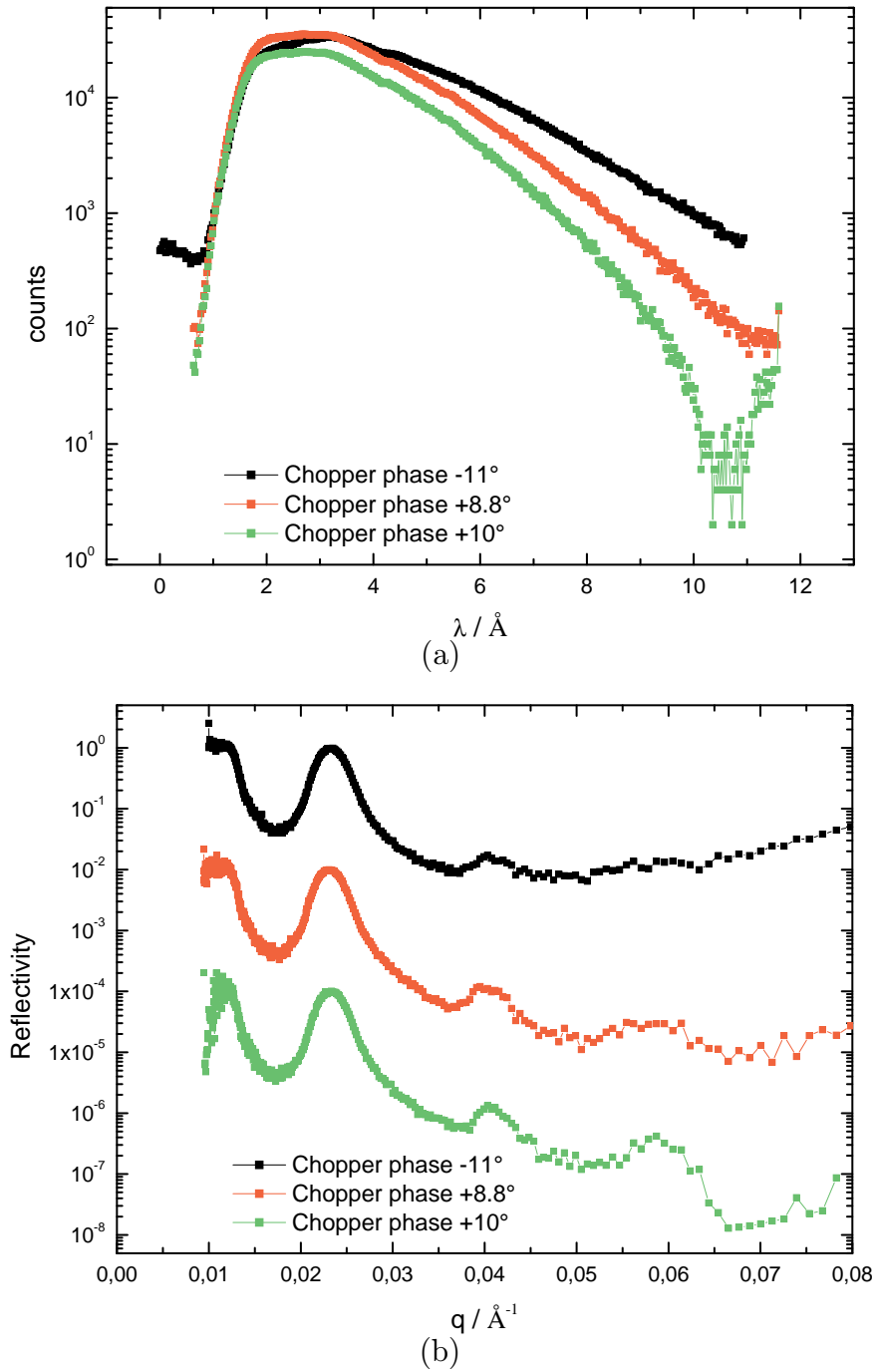


Figure 5.4: (a) Spectra of the primary beam measured at a chopper speed of 1500 rpm and different chopper phases. The intensity was normalized to a measuring time of 15 min. (b) Reflectivity data obtained from the sample PSI08 ($d = 1 \mu\text{m}$, $E = 2 \text{V}/\mu\text{m}$), measured at the corresponding chopper settings as in (a). The incident angle ω was 0.5° for each case. The data are offset for clarity.

where v_r is the rotation speed of the chopper. If the angle of each sectorial window in the chopper disks is ϕ_0 , the optimal phase difference ϕ between the two chopper disks is given by

$$\phi = \phi_0 - \delta \quad (5.10)$$

Now let us estimate the optimal phase difference ϕ for the following instrumental setting conditions: $L = 7.2$ m, $\Delta L = 0.14$ m, $v_r = 1500$ rpm (rotations per minute), and $\phi_0 = 13.8^\circ$. The time interval t_{pul} is determined by v_r as

$$t_{pul} = \frac{1}{2} \times \frac{1}{v_r} = \frac{1}{2} \times \frac{60 \text{ s}}{1500} = 0.02 \text{ s} \quad (5.11)$$

The factor $1/2$ comes from the fact that each disk involves two opening windows in the diametrical position. If the velocity v_f of the fastest neutrons is about 700 m/s (for cold neutrons), the velocity v_s of the slowest neutrons can be calculated from eq. (5.7) as

$$v_s = \frac{L}{\frac{L}{v_f} + t_{pul}} = \frac{7.2 \text{ m}}{\frac{7.2 \text{ m}}{700 \text{ m/s}} + 0.02 \text{ s}} \approx 238 \text{ m/s} \quad (5.12)$$

and the angle δ can be calculated from eq. (5.9) as

$$\delta = 360^\circ \cdot v_r \cdot \frac{\Delta L}{v_s} = 360^\circ \cdot \frac{1500}{60 \text{ s}} \cdot \frac{0.14 \text{ m}}{238 \text{ m/s}} \approx 5^\circ \quad (5.13)$$

The optimal phase difference ϕ between the two chopper disks is then given by

$$\phi = \phi_0 - \delta = 13.8^\circ - \delta \approx 8.8^\circ \quad (5.14)$$

5.1.3 Time offset

As shown in Fig. 5.4 (a), the primary beam consists of neutrons with wavelengths from $\sim 1 \text{ \AA}$ to $\sim 10 \text{ \AA}$ with a maximum flux at around $2\text{-}3 \text{ \AA}$. Seen from eq. (5.2), for a certain range of wavelength, the scattering vector q measured is proportional to the angle of incidence ω ($= \theta$) at which the reflectivity is measured. In reality, the reflectivity is measured at several angles of incidence, and superposing these data yields the whole reflectivity curve in a large q -range. In our experiments, the reflectivity was measured at $\omega = 0.25^\circ$, 0.5° and 1° . The reflectivity data obtained from the sample PSI08 (table 5.1) are shown in Fig. 5.5 (a). At $\omega = 0.25^\circ$, the maximum flux of neutrons in the primary beam gives rise to a good statistics at small q . With increasing ω , the q -range in which the measurement shows a good statistics moves to large q . Especially, in the case of $\omega = 1^\circ$, the critical edge was not measured at all. The scattering vector q is calculated from the time-of-flight t according to eq. (5.4). An offset in time will result in a shift of the curves along the q -axis. Often, it was found necessary to introduce such an offset in time in order to overlap the three reflectivity curves measured at different angles. The origin of the offset in time is that the initial phase of the chopper is not zero when the detector starts to count time. The offset t_o , either an advance or a lag in time, is constant for neutrons with all wavelengths. The true time-of-flight t_t needed by the neutrons is simply obtained by adding the offset to the measured time, i.e.,

$$t_t = t_m + t_o \quad (5.15)$$

where t_m is the measured time-of-flight, and for neutrons received in channel i it is given by

$$t_m = (i - 1) \cdot \Delta t_{tch} \quad (5.16)$$

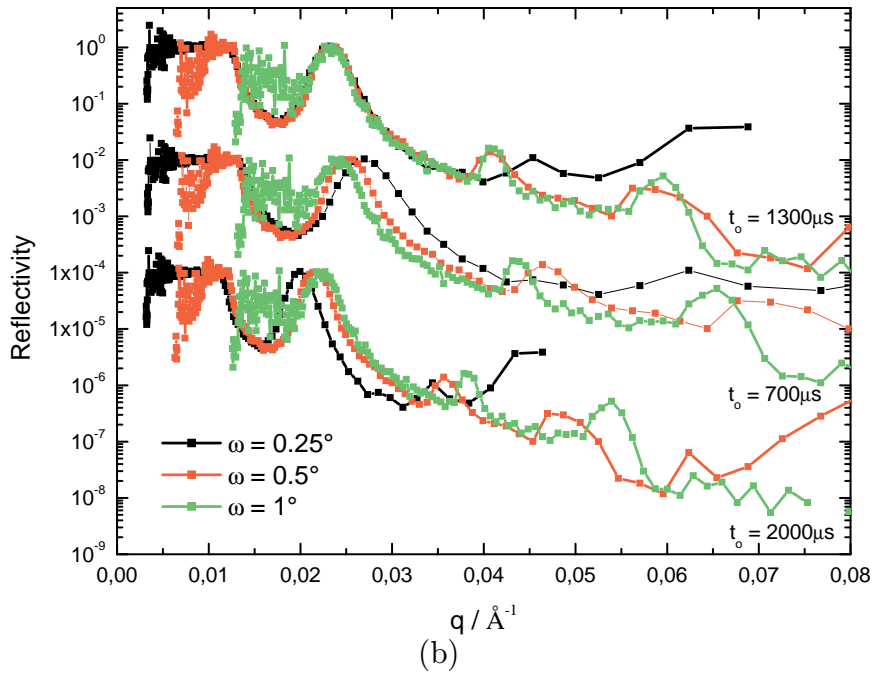
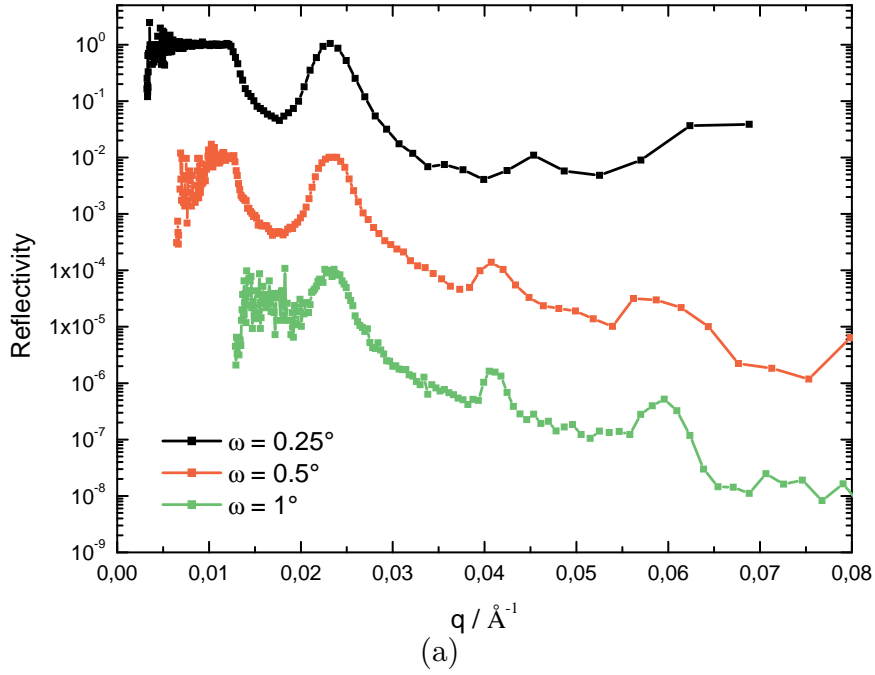


Figure 5.5: Reflectivity data obtained from the sample PSI08 ($d = 1 \mu\text{m}$, $E = 2 \text{ V}/\mu\text{m}$), measured at a chopper speed of 1000 rpm and a phase difference of $+11^\circ$ between the two chopper disks. The data are offset for clarity. In (a), the data measured at different angles of incidence are compared. In (b), these data are plotted versus q with different offsets t_o in time.

where Δt_{tch} is the time channel window of the detector. As shown in Fig. 5.5 (b), the three reflectivity curves overlap with each other only if a suitable value of t_o is selected. The value of t_o is then determined in this way.

5.1.4 Normalization

Measuring time

As shown in Fig. 5.2, the reflectivity is obtained by dividing the counts of neutrons measured during a specular scan by the counts of neutrons measured without a sample in the beam (the primary beam). The prerequisite of this method is that the measuring time of the two measurements is the same, because the total number of neutrons will be proportional to the counting time if the source is stable. In reality, it is the total number of neutrons instead of the measuring time that is counted. As shown in Fig. 5.1, a monitor 1 is installed after the neutron guides to detect the number of neutrons coming from the source. The counting time of a measurement is set by giving a counting number of neutrons detected by this monitor. For example, the command “count monitor 72E6” means the measurement will be finished only if the number of neutrons detected by monitor 1 reaches 72E6 (which corresponds to 1 h in the case of a stable source). If the beam is broken up for some reason during the measurement, the measurement will be continued after the beam comes back. In addition, in spite of the real counting time of the measurement, the total number of neutrons is fixed (or can be normalized) which insures the comparison between data from different measurements. Usually a longer measuring time is needed for a measurement with relatively lower intensity, like in the case of reflectivity measurements at higher angles of incidence. For this reason, the reflectivity at $\omega = 0.25^\circ$ was measured for 10 min (corresponding counting time), and those at $\omega = 0.5^\circ$ and 1° were measured for 30 min. The primary beam was measured for 15 min. The data should be normalized according to the measuring time, which gives the first normalization factor.

Over-illumination

As shown in Fig. 5.6, the sample is illuminated by only part of the incident beam if the incident angle ω is smaller than a critical value. This critical value ω_c is determined as

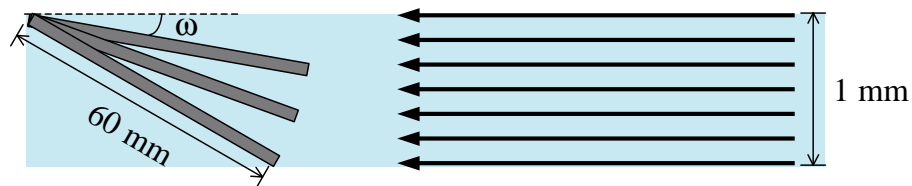


Figure 5.6: Illustration of the over-illumination phenomenon. The sample will be over-illuminated if the incident angle ω is below a critical value 1° .

$$\sin \omega_c = \frac{1 \text{ mm}}{60 \text{ mm}} \approx 1^\circ \quad (5.17)$$

where 1 mm is the vertical size of the beam and 60 mm is the size of the sample. The sample will be over-illuminated if $\omega < 1^\circ$. The reflectivity measured at $\omega = 0.25^\circ$, 0.5° , and 1° should be normalized by a factor of $\sin \omega$ which is the second normalization factor used in our data analysis.

Normalization to 1

The finally normalized reflectivity data should show the following features: (i) the reflectivity should be equal to one below the critical edge due to the total reflection; (ii) the reflectivity at the peak maximum of the first order Bragg peak should be equal to one in our case where the scattering contrast between the block components is large enough. However, the reflectivity data after being normalized by the two factors described in the previous sections are usually not finally normalized. In this case, the data should be normalized according to feature (i) if the critical edge is visible. Otherwise the normalization can be done according to feature (ii). In rare cases, the reflectivity at the peak maximum of the first order Bragg peak is not consistent with that below the critical edge. Then the data should be normalized according to the higher one because the reflectivity cannot be higher than 1.

5.1.5 Resolution

The resolution in q for a time-of-flight reflectometric experiment consists of two contributions, such as [60]

$$\frac{(\Delta q)^2}{q^2} = \frac{(\Delta\theta)^2}{\theta^2} + \frac{(\Delta t)^2}{t^2} \quad (5.18)$$

where $\Delta\theta/\theta$ is the angular resolution and $\Delta t/t$ is the TOF (time-of-flight) resolution.

The angular resolution in our experiments is defined by the two slits before the sample with a vertical size of d_1 and d_2 respectively and a distance l between the two slits (Fig. 5.7). The angular resolution is given by [60] ($\Delta\theta$ in rad)

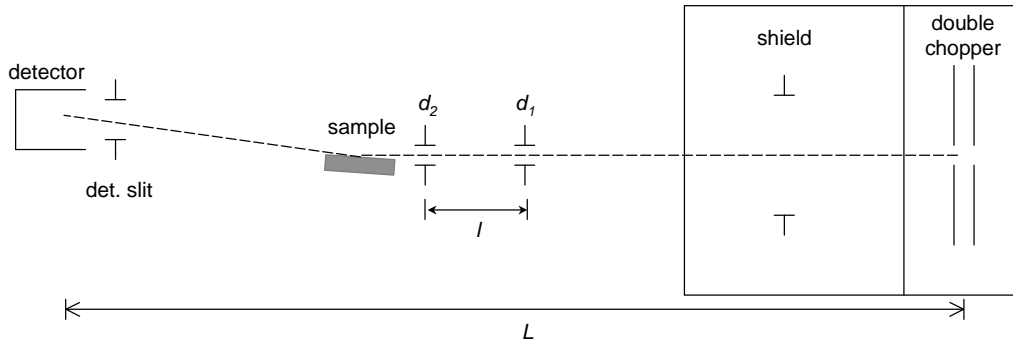


Figure 5.7: Angular resolution in our time-of-flight reflectometric experiments, defined by the two slits before the sample with a vertical size of d_1 and d_2 respectively and a distance l between the two slits.

$$\frac{(\Delta\theta)^2}{\theta^2} = 0.68^2 \left(\frac{d_1^2 + d_2^2}{l^2} \right) \frac{1}{\theta^2} \quad (5.19)$$

where the factor 0.68 comes from the convolution of a rectangularly distributed variable with a Gaussian resolution function, which is often done in data interpretation softwares.

The TOF resolution is given by [59]

$$\frac{(\Delta t)^2}{t^2} = \frac{(\Delta t_{pul})^2 + (\Delta t_{tch})^2}{t^2} \quad (5.20)$$

where Δt_{pul} and Δt_{tch} are the contributions from the chopper and the detector, respectively. The former Δt_{pul} is the width of the pulse representing the resolution in

determining the starting point of time t , and the latter Δt_{tch} is the time channel window of the detector representing the resolution in determining the ending point of time t . It can be shown that the contribution of Δt_{tch} from the detector can be in general neglected. The TOF resolution is then given by

$$\frac{(\Delta t)^2}{t^2} = \frac{(\Delta t_{pul})^2}{t^2} = 0.68^2 \left(\frac{h \Delta t_{pul}}{4\pi m L} \frac{q}{\sin \theta} \right) \quad (5.21)$$

where we used the expression

$$t = \frac{4\pi m L \sin \theta}{h q} \quad (5.22)$$

from eq. (5.4). Eq. (5.21) shows that the resolution in q becomes worse with increasing q at a fixed angle of incidence θ ($= \omega$), and becomes better in the whole q -range at an increased angle of incidence θ .

Seen from eqs. (5.19) and (5.21), both the angular resolution and the TOF resolution depend on the incident angle θ ($= \omega$) of the measurement. Now let us estimate the resolution in q at, e.g., $\theta = 1^\circ$. Using the values $d_1 = 1$ mm, $d_2 = 0.5$ mm, and $l = 709$ mm, we estimate the angular resolution as

$$\frac{\Delta \theta}{\theta} = 0.68 \left(\sqrt{\frac{d_1^2 + d_2^2}{l^2}} \right) \frac{1}{\theta} = 0.68 \left(\sqrt{\frac{1^2 + 0.5^2}{709^2}} \right) \frac{180^\circ}{3.14 \times 1^\circ} \approx 0.06 \quad (5.23)$$

The TOF resolution is estimated for the following instrumental setting conditions: the distance from the chopper to the detector $L = 7.2$ m, the rotation speed of the chopper $v_r = 1000$ rpm (rotations per minute), the angle of each sectorial window in the chopper disks $\phi_0 = 13.8^\circ$, the phase difference $\phi = +11^\circ$ between the two chopper disks, and the number of time channels $n_{tch} = 200$ at the detector. Note that these conditions are not exactly the same as those used in section 5.1.2. The time interval t_{pul} is calculated from eq. (5.11) as

$$t_{pul} = \frac{1}{2} \times \frac{1}{v_r} = \frac{1}{2} \times \frac{60 \text{ s}}{1000} = 0.03 \text{ s} \quad (5.24)$$

The width of the pulse Δt_{pul} and the time channel window Δt_{tch} are calculated as

$$\Delta t_{pul} = t_{pul} \times \frac{(\phi_0 - \phi)}{180^\circ} = 0.03 \text{ s} \times \frac{(13.8^\circ - 11^\circ)}{180^\circ} \approx 467 \mu\text{s} \quad (5.25)$$

and

$$\Delta t_{tch} = \frac{t_{pul}}{n_{tch}} = \frac{0.03 \text{ s}}{200} = 150 \mu\text{s} \quad (5.26)$$

respectively, showing that $(\Delta t_{pul})^2$ is about ten times as large as $(\Delta t_{tch})^2$ so that the contribution of Δt_{tch} to the TOF resolution can be neglected. The TOF resolution is then calculated from eq. (5.21) as

$$\frac{\Delta t}{t} = \frac{0.68 \times (6.626 \times 10^{-34} \text{ J s}) \times (467 \times 10^{-6} \text{ s})}{4 \times 3.1416 \times (1.6747 \times 10^{-27} \text{ kg}) \times 7.2 \text{ m} \times \sin 1^\circ} q \approx (0.8 \text{ \AA}) q \quad (5.27)$$

The sum of eqs. (5.23) and (5.27) gives the total resolution in q

$$\frac{\Delta q}{q} = \frac{\Delta \theta}{\theta} + \frac{\Delta t}{t} = 0.06 + (0.8 \text{ \AA}) q \quad (5.28)$$

or

$$\Delta q = \left(\frac{\Delta \theta}{\theta} + \frac{\Delta t}{t} \right) q = 0.06q + (0.8 \text{ \AA}) q^2 \quad (5.29)$$

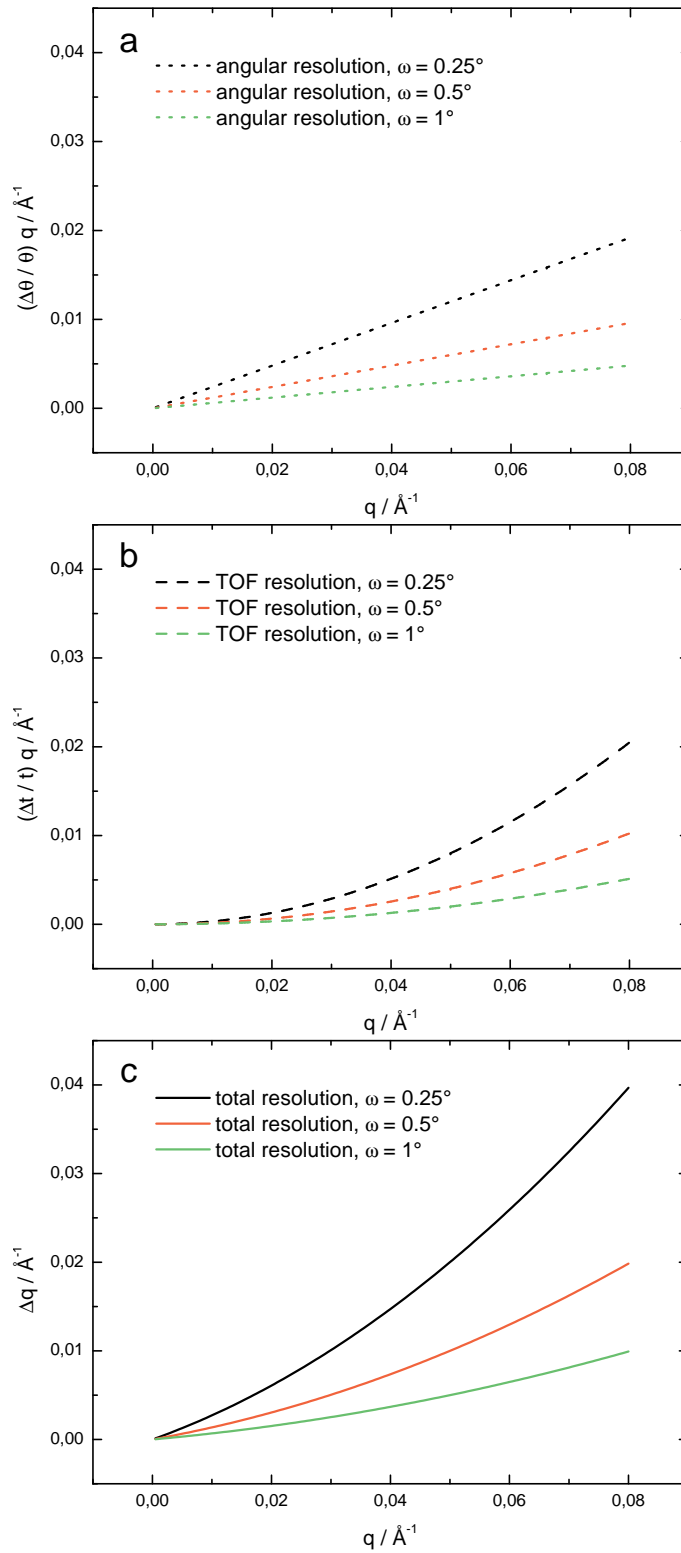


Figure 5.8: Calculated resolution for reflectivity measured at $\theta(=\omega) = 0.25^\circ, 0.5^\circ,$ and 1.0° : (a) angular resolution, (b) TOF resolution, and (c) total resolution. The total resolution Δq is the sum of the angular resolution $(\Delta\theta/\theta)q$ and the TOF resolution $(\Delta t/t)q$.

Fig. 5.8 shows the results of the calculated resolution. The total resolution Δq for reflectivity measured at $\theta(=\omega) = 1^\circ$ is increased from 0 to $\sim 0.01 \text{ \AA}$ in the q -range from 0 to $\sim 0.08 \text{ \AA}^{-1}$. On the other hand, the resolution of a measurement can be estimated from the full-width at half-maximum of the Bragg peaks shown in the data. The calculated resolution is roughly consistent with that estimated from the data e.g., shown in Fig. 5.5.

5.1.6 Refraction effect

Besides the reflectivity measured at angles of incidence $\omega = 0.25^\circ, 0.5^\circ,$ and 1° , the diffuse scattering was measured at a fixed scattering angle $2\theta = 1^\circ$. The scattering angle was fixed by fixing the directions of the incoming beam and the outgoing beam with respect to the sample. A desired angle of incidence ω can be obtained by rotating the sample by an angle $\Delta\omega = \omega - (2\theta)/2$. At each ω , the diffuse scattering was measured along the corresponding longitudinal scan shown in Fig. 3.11. A line visualization of the scans used in our experiments is shown in Fig. 5.9. The red line corresponds to

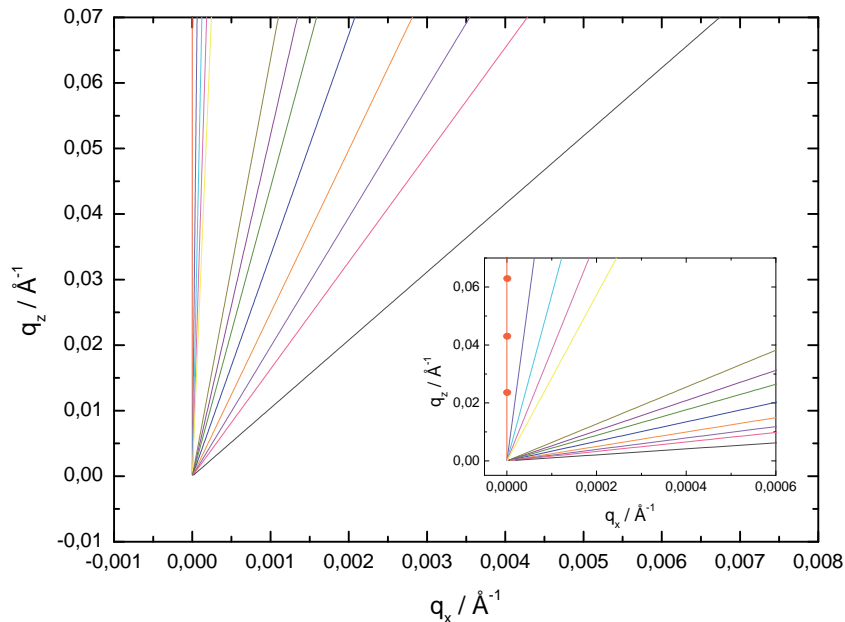


Figure 5.9: Line visualization of scans in reciprocal space. The scattering angle 2θ was fixed at 1° . The inserted figure is an enlargement of part of the main figure, showing the positions of the Bragg peaks in reflectivity indicated by the red dots.

the specular scan at $\omega = (2\theta)/2 = 0.5^\circ$. The other lines correspond to longitudinal diffuse scans at $\omega = 0.55^\circ, 0.6^\circ, 0.65^\circ, 0.7^\circ, 1.4^\circ, 1.6^\circ, 1.8^\circ, 2.2^\circ, 2.8^\circ, 3.4^\circ, 4.0^\circ,$ and 6.0° , respectively. Fig. 5.10 (a) shows such diffuse scattering obtained from the sample AUG04C (table 5.1). A shift in the peak position of the first order Bragg peaks was observed from $\omega < 2\theta = 1^\circ$ to $\omega > 2\theta = 1^\circ$. The peak position of the Bragg peaks, characterizing the lamellar period of the layered structure, should however not be dependent on the incident angle ω . Note that the above statement is valid in terms of the internal scattering vector $q_{z,i}$, which is related to the external scattering vector $q_{z,0}$ by $q_{z,i} = \sqrt{q_{z,0}^2 - q_{c,0}^2}$ in the case of reflectivity, where $q_{c,0} = 4\pi \sin \theta_{c,0} / \lambda$ with $\theta_{c,0}$ being the critical angle at the air/polymer interface. The difference between the values of $q_{z,i}$ and $q_{z,0}$ derives from the refraction at the surface of the sample. In the following section, it will be shown the calculation of $q_{z,i}$ from q_0 in the case of diffuse scattering.

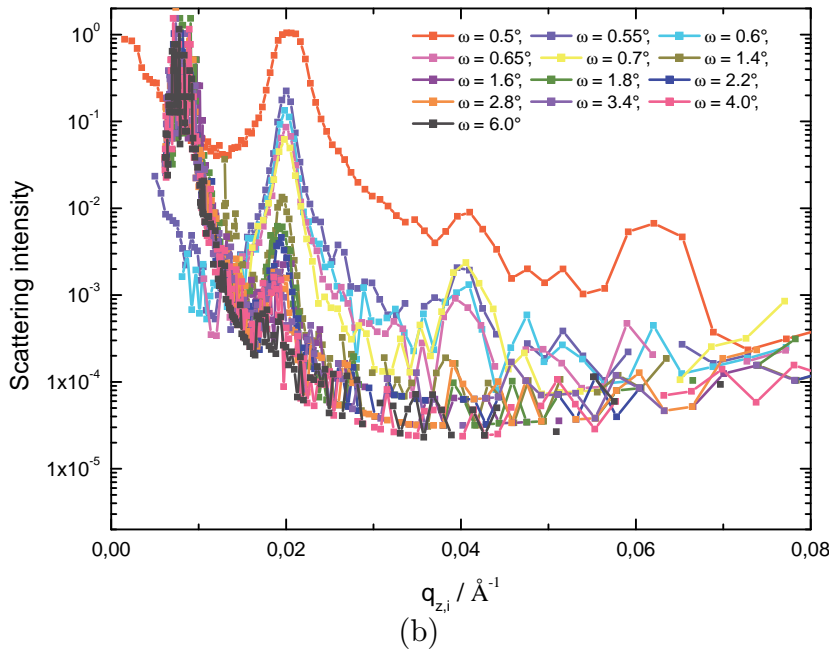
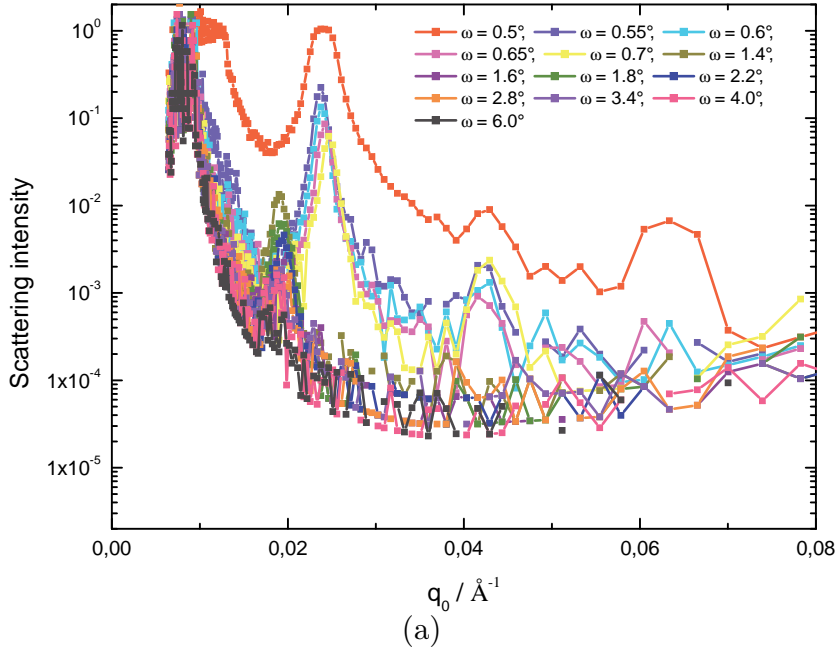


Figure 5.10: Reflectivity and diffuse scattering data obtained from the sample AUG04C ($d = 0.86 \mu\text{m}$, $E = 1 \text{ V}/\mu\text{m}$). The data are plotted versus the external q_0 in (a), showing a shift in the peak position due to the refraction effect. The data replotted versus the internal $q_{z,i}$ in (b) show the shift in the peak position vanishes after the correction of the refraction effect. The diffuse scattering data were normalized by the same factor used for normalizing the corresponding reflectivity.

In Fig. 5.10 (b), the same data as in (a) are replotted versus the internal scattering vector $q_{z,i}$, and the shift in the peak position from $\omega < 2\theta$ to $\omega > 2\theta$ vanishes after the correction of the refraction effect. The shift in the peak position can be qualitatively understood from Fig. 5.11, where three different geometries are shown. In Fig. 5.11 (a), where $\omega < 2\theta$, the beam comes in from air and goes out from air. In Fig. 5.11 (b), where $\omega > 2\theta$ and a thick silicon wafer of ~ 10 mm is used, the beam comes in from air and goes out from the side of the wafer. In Fig. 5.11 (c), where $\omega > 2\theta$ and a thin silicon wafer of ~ 500 μ m is used, the beam comes in from air and goes out from the back of the wafer. In order to insure the occurrence of geometry (b) instead of geometry (c), thick silicon wafers were always used in our experiments. The change in the geometry from (a) to (b) explains the shift in the peak position shown in Fig. 5.10.

Calculation of internal scattering vector

As shown in Fig. 5.11, the directions of the incoming beam and the outgoing beam with respect to the sample were fixed during the diffuse scattering measurements. As the incident angle increases from 0.55° to 6.0° , the z direction defined as along the surface normal of the sample will be changed correspondingly. The z - and x - components of the internal scattering vector, $q_{z,i}$ and $q_{x,i}$, can be calculated based on their definitions. In order to calculate $q_{z,i}$ and $q_{x,i}$ for different geometries, it is convenient to define variables in different media, and denote them using a subscript indicating the corresponding medium. The variables used in our calculation are listed in table 5.2. If the wavelength

	in air	in polymer	in silicon
wavelength	λ_0	λ_i	λ_s
incident wave vector	\mathbf{k}_0	\mathbf{k}_i	\mathbf{k}_s
scattered wave vector	\mathbf{k}'_0	\mathbf{k}'_i	\mathbf{k}'_s
scattering vector	\mathbf{q}_0	\mathbf{q}_i	\mathbf{q}_s
incident angle	ω_0	ω_i	ω_s
exit angle	ω'_0	ω'_i	ω'_s
scattering angle	$(2\theta)_0$	$(2\theta)_i$	$(2\theta)_s$

Table 5.2: Definitions of the variables used in the calculation of $q_{z,i}$ and $q_{x,i}$. The subscripts 0, i and s indicate the air, the polymer and the silicon medium, respectively.

in air is λ_0 , the wavelengths in polymer and in silicon are

$$\lambda_i = \frac{\lambda_0}{n_i}, \quad \lambda_s = \frac{\lambda_0}{n_s} \quad (5.30)$$

where n_i and n_s are the refractive indices of the polymer and the silicon, respectively. The z - and x - components of the incident and scattered wave vectors in air, polymer, and silicon are given by

$$|\mathbf{k}_{z,0}| = \frac{2\pi}{\lambda_0} \sin \omega_0, \quad |\mathbf{k}_{z,i}| = \frac{2\pi}{\lambda_i} \sin \omega_i, \quad |\mathbf{k}_{z,s}| = \frac{2\pi}{\lambda_s} \sin \omega_s \quad (5.31)$$

$$|\mathbf{k}'_{z,0}| = \frac{2\pi}{\lambda_0} \sin \omega'_0, \quad |\mathbf{k}'_{z,i}| = \frac{2\pi}{\lambda_i} \sin \omega'_i, \quad |\mathbf{k}'_{z,s}| = \frac{2\pi}{\lambda_s} \sin \omega'_s \quad (5.32)$$

$$|\mathbf{k}_{x,0}| = \frac{2\pi}{\lambda_0} \cos \omega_0, \quad |\mathbf{k}_{x,i}| = \frac{2\pi}{\lambda_i} \cos \omega_i, \quad |\mathbf{k}_{x,s}| = \frac{2\pi}{\lambda_s} \cos \omega_s \quad (5.33)$$

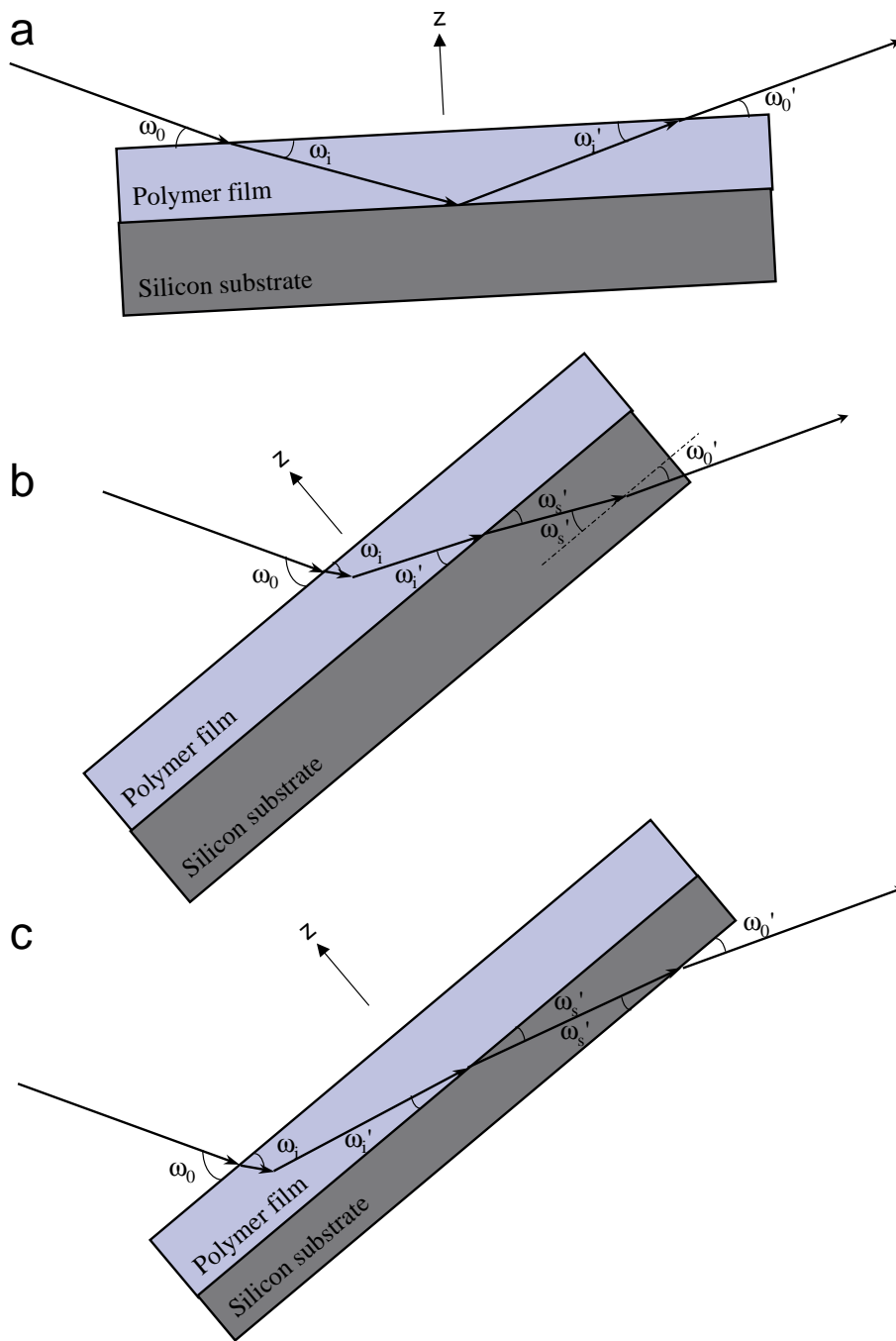


Figure 5.11: Diffuse scattering geometries: (a) $\omega < 2\theta$; (b) $\omega > 2\theta$, and a thick silicon wafer is used; (c) $\omega > 2\theta$, and a thin silicon wafer is used. In all these cases, the neutron beam comes from the air side but goes out from different sides of the sample. The z direction is always defined as along the surface normal of the sample.

$$|\mathbf{k}'_{x,0}| = \frac{2\pi}{\lambda_0} \cos \omega'_0, \quad |\mathbf{k}'_{x,i}| = \frac{2\pi}{\lambda_i} \cos \omega'_i, \quad |\mathbf{k}'_{x,s}| = \frac{2\pi}{\lambda_s} \cos \omega'_s \quad (5.34)$$

The z - and x - components of the internal scattering vector \mathbf{q}_i can be calculated as

$$|\mathbf{q}_{z,i}| = |\mathbf{k}'_{z,i} - \mathbf{k}_{z,i}| = |\mathbf{k}'_{z,i}| + |\mathbf{k}_{z,i}|, \quad \omega_0 < (2\theta)_0 \quad (5.35)$$

$$|\mathbf{q}_{z,i}| = |\mathbf{k}'_{z,i} - \mathbf{k}_{z,i}| = \left| |\mathbf{k}'_{z,i}| - |\mathbf{k}_{z,i}| \right|, \quad \omega_0 > (2\theta)_0 \quad (5.36)$$

$$|\mathbf{q}_{x,i}| = |\mathbf{k}'_{x,i} - \mathbf{k}_{x,i}| = \left| |\mathbf{k}'_{x,i}| - |\mathbf{k}_{x,i}| \right| \quad (5.37)$$

From eqs. (5.30)-(5.37), the magnitudes of $q_{z,i}$ and $q_{x,i}$ can be calculated for geometry (a) as

$$|\mathbf{q}_{z,i}| = \frac{2\pi}{\lambda_0} \left(\sqrt{\sin^2 \omega_0 - \sin^2 \theta_{c,0}} + \sqrt{\sin^2 \omega'_0 - \sin^2 \theta_{c,0}} \right) \quad (5.38)$$

$$|\mathbf{q}_{x,i}| = -\frac{2\pi}{\lambda_0} \left(\sqrt{1 - \sin^2 \omega_0} - \sqrt{1 - \sin^2 \omega'_0} \right) \quad (5.39)$$

and for geometry (b) as

$$|\mathbf{q}_{z,i}| = \frac{2\pi}{\lambda_0} \left(\sqrt{\sin^2 \omega_0 - \sin^2 \theta_{c,0}} - \sqrt{\sin^2 \omega'_0 - \left(\frac{n_s}{n_0}\right)^2 \sin^2 \theta_{c,s}} \right) \quad (5.40)$$

$$|\mathbf{q}_{x,i}| = -\frac{2\pi}{\lambda_0} \left(\sqrt{1 - \sin^2 \omega_0} - \sqrt{\left(\frac{n_s}{n_0}\right)^2 - \sin^2 \omega'_0} \right) \quad (5.41)$$

and for geometry (c) as

$$|\mathbf{q}_{z,i}| = \frac{2\pi}{\lambda_0} \left(\sqrt{\sin^2 \omega_0 - \sin^2 \theta_{c,0}} - \sqrt{\sin^2 \omega'_0 - \sin^2 \theta_{c,0}} \right) \quad (5.42)$$

$$|\mathbf{q}_{x,i}| = -\frac{2\pi}{\lambda_0} \left(\sqrt{1 - \sin^2 \omega_0} - \sqrt{1 - \sin^2 \omega'_0} \right) \quad (5.43)$$

where $\theta_{c,0}$ and $\theta_{c,s}$ are the critical angles at the air/polymer and polymer/silicon interfaces, respectively. Our calculation of $q_{z,i}$ is consistent with eq. (3) in ref [61].

Critical angle and critical wave vector

The critical angle $\theta_{c,0}$ is given by

$$\cos \theta_{c,0} = n_i \quad (5.44)$$

where n_i is the refractive index of the polymer. For $\theta_{c,0} \ll 1$, eq. (5.44) can be rewritten as $1 - \theta_{c,0}^2/2 \approx 1 - \delta_i$ with $\delta_i = \rho_i \lambda^2 / (2\pi)$. Therefore we get

$$\theta_{c,0} \approx \sqrt{2\delta_i} = \sqrt{\rho_i / \pi} \lambda \quad (5.45)$$

showing that $\theta_{c,0}$ is dependent on wavelength. Here the wavelength λ is referred to that in air. It should be noted that δ_i is on the order of 10^{-6} , thus n_i is only slightly different from 1 and the values of λ_i and λ_0 are very close to each other. We simply denote the wavelength as λ . The critical wave vector

$$|\mathbf{k}_{c,0}| = \frac{2\pi}{\lambda_0} \sin \theta_{c,0} \approx \frac{2\pi}{\lambda} \theta_{c,0} = \sqrt{4\pi\rho_i} \quad (5.46)$$

is shown to be independent of wavelength.

Similarly, the critical angle $\theta_{c,s}$ is given by

$$\cos \theta_{c,s} = \frac{n_i}{n_s} \quad (5.47)$$

where n_i and n_s are the refractive indices of the polymer and the silicon, respectively. It can be shown that

$$\theta_{c,s} \approx \sqrt{2(\delta_i - \delta_s)} = \sqrt{(\rho_i - \rho_s)/\pi \lambda} \quad (5.48)$$

and

$$|\mathbf{k}_{c,s}| = \frac{2\pi}{\lambda_s} \sin \theta_{c,s} \approx \frac{2\pi}{\lambda} \theta_{c,s} = \sqrt{4\pi(\rho_i - \rho_s)} \quad (5.49)$$

Again, $\theta_{c,s}$ is dependent on wavelength while $|\mathbf{k}_{c,s}|$ is independent of wavelength.

In a time-of-flight mode measurement where a white beam of neutrons with different wavelengths is used, it is more convenient to express the internal scattering vector in terms of wave vector (because the critical wave vectors are independent of wavelength). Eqs. (5.38)-(5.43) become then, for geometry (a)

$$|\mathbf{q}_{z,i}| = \sqrt{|\mathbf{k}_{z,0}|^2 - |\mathbf{k}_{c,0}|^2} + \sqrt{|\mathbf{k}'_{z,0}|^2 - |\mathbf{k}_{c,0}|^2} \quad (5.50)$$

$$|\mathbf{q}_{x,i}| = -\left(\sqrt{(2\pi/\lambda_0)^2 - |\mathbf{k}_{z,0}|^2} - \sqrt{(2\pi/\lambda_0)^2 - |\mathbf{k}'_{z,0}|^2}\right) \quad (5.51)$$

and for geometry (b)

$$|\mathbf{q}_{z,i}| = \sqrt{|\mathbf{k}_{z,0}|^2 - |\mathbf{k}_{c,0}|^2} - \sqrt{|\mathbf{k}'_{z,0}|^2 - |\mathbf{k}_{c,s}|^2} \quad (5.52)$$

$$|\mathbf{q}_{x,i}| = -\left(\sqrt{(2\pi/\lambda_0)^2 - |\mathbf{k}_{z,0}|^2} - \sqrt{(2\pi/\lambda_s)^2 - |\mathbf{k}'_{z,0}|^2}\right) \quad (5.53)$$

and for geometry (c)

$$|\mathbf{q}_{z,i}| = \sqrt{|\mathbf{k}_{z,0}|^2 - |\mathbf{k}_{c,0}|^2} - \sqrt{|\mathbf{k}'_{z,0}|^2 - |\mathbf{k}_{c,0}|^2} \quad (5.54)$$

$$|\mathbf{q}_{x,i}| = -\left(\sqrt{(2\pi/\lambda_0)^2 - |\mathbf{k}_{z,0}|^2} - \sqrt{(2\pi/\lambda_0)^2 - |\mathbf{k}'_{z,0}|^2}\right) \quad (5.55)$$

Calculation of critical wave vectors

From now on, we omit the subscript of λ , ω , and 2θ . All these variables will be referred to those in the air medium. Since the values of the critical wave vectors $|\mathbf{k}_{c,0}|$ and $|\mathbf{k}_{c,s}|$ are independent of wavelength, we will calculate them for a particular wavelength. At $\lambda = 1.54 \text{ \AA}$, the values of δ for deuterated-PS, PMMA and silicon are

$$\delta_{\text{d-PS}} = 2.336 \times 10^{-6}, \quad \delta_{\text{PMMA}} = 0.390 \times 10^{-6}, \quad \delta_s = 0.791 \times 10^{-6} \quad (5.56)$$

If we take an average value of deuterated-PS and PMMA for our block copolymer, the scattering length densities for the copolymer and silicon can be calculated as

$$\rho_i = \frac{2\pi\delta_i}{\lambda^2} = \frac{2\pi \times (1.363 \times 10^{-6})}{(1.54 \text{ \AA})^2} = 3.61 \times 10^{-6} \text{ \AA}^{-2} \quad (5.57)$$

$$\rho_s = \frac{2\pi\delta_s}{\lambda^2} = \frac{2\pi \times (0.791 \times 10^{-6})}{(1.54 \text{ \AA})^2} = 2.09 \times 10^{-6} \text{ \AA}^{-2} \quad (5.58)$$

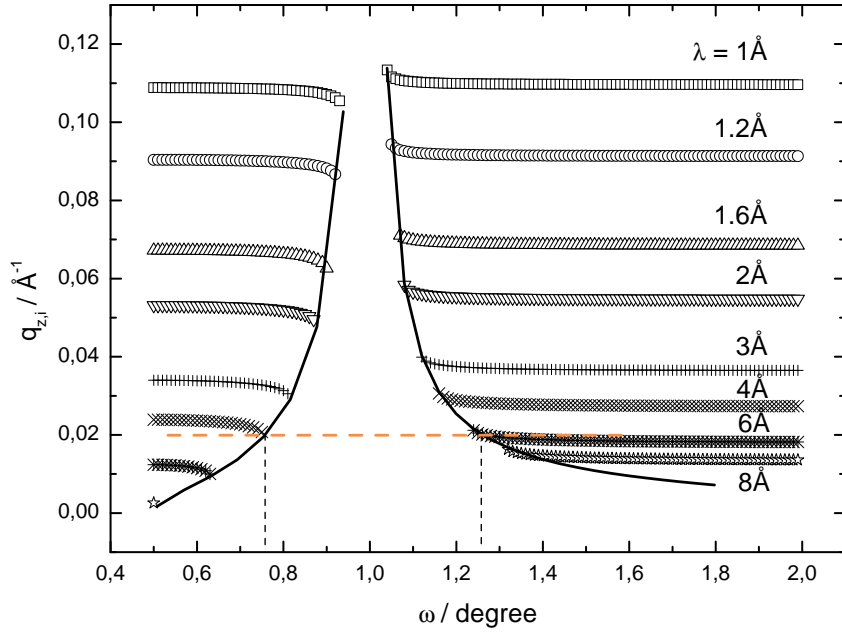


Figure 5.12: Plots of $q_{z,i}$ versus ω calculated for $2\theta = 1^\circ$ and different wavelength λ s. For a certain $q_{z,i}$, there is always an experimentally inaccessible range of ω . The boundary (indicated by the solid line) of this inaccessible region can be calculated from eqs. (5.61) and (5.62).

The values of $|\mathbf{k}_{c,0}|$ and $|\mathbf{k}_{c,s}|$ are then

$$|\mathbf{k}_{c,0}| = \sqrt{4\pi\rho_i} = 0.00673 \text{ \AA} \quad (5.59)$$

$$|\mathbf{k}_{c,s}| = \sqrt{4\pi(\rho_i - \rho_s)} = 0.00436 \text{ \AA} \quad (5.60)$$

We should mention that the values of $|\mathbf{k}_{c,0}|$ and $|\mathbf{k}_{c,s}|$ obtained from our experiments vary a little bit from sample to sample. Therefore, the averaged and optimal values $|\mathbf{k}_{c,0}| = 0.00635 \text{ \AA}$ and $|\mathbf{k}_{c,s}| = 0.00426 \text{ \AA}$ are used in our data analysis. These values are roughly consistent with the calculated ones.

Further discussion

Fig. 5.12 shows the plots of $q_{z,i}$ versus ω calculated for different wavelength λ s. The wavelengths used here cover almost the whole range of those shown in the spectrum of the primary beam [Fig. 5.4 (a)], i.e., from 1 \AA to 8 \AA . For a certain $q_{z,i}$, there is always an experimentally inaccessible range of ω (which can be converted into $q_{x,i}$). The reason for this can be seen from eqs. (5.38) and (5.40), in which the sign of square root exerts a limit on the part inside the sign. If $\omega < 2\theta$, we have geometry (a), and $q_{z,i}$ is calculated from eq. (5.38). From Fig. 5.11 (a), we see $\omega + \omega' = 2\theta$. As ω increases, ω' decreases until the condition $\omega' = \theta_{c,0}$ is fulfilled. At this condition, we have

$$\begin{aligned} \omega' &= \theta_{c,0} \\ \omega &= 2\theta - \omega' = 1^\circ - \theta_{c,0} \\ q_{z,i} &= \frac{2\pi}{\lambda} \sqrt{\sin^2 \omega - \sin^2 \theta_{c,0}} \end{aligned} \quad (5.61)$$

If $\omega > 2\theta$, we have geometry (b), and $q_{z,i}$ is calculated from eq. (5.40). From Fig. 5.11 (b), we see $\omega - \omega' = 2\theta$. As ω decreases, ω' decreases until the condition $\omega' = \theta_{c,s}$ is

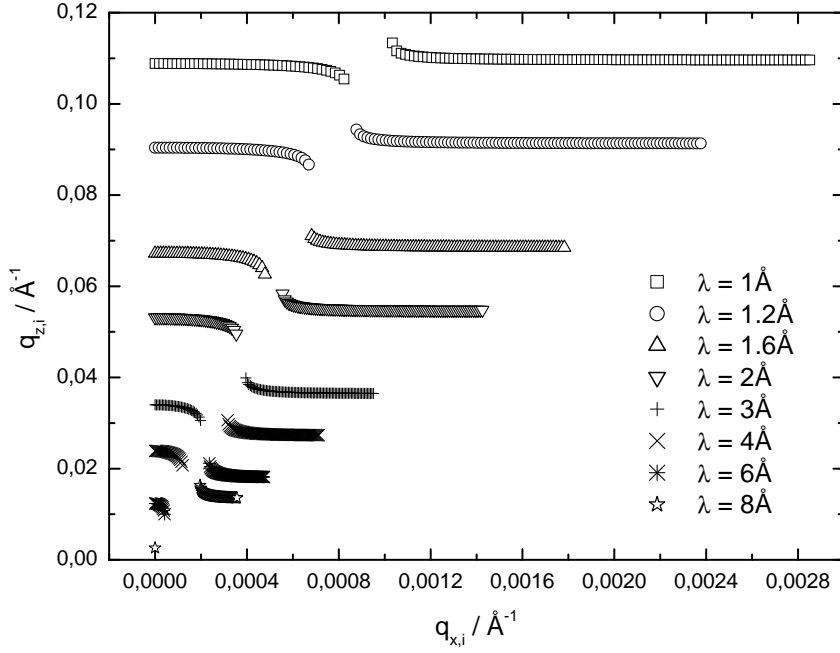


Figure 5.13: Plots of $q_{z,i}$ versus $q_{x,i}$ calculated for $2\theta = 1^\circ$ and different wavelength λ s.

fulfilled. At this condition, we have

$$\begin{aligned}
 \omega' &= \theta_{c,s} \\
 \omega &= 2\theta + \omega' = 1^\circ + \theta_{c,s} \\
 q_{z,i} &= \frac{2\pi}{\lambda} \sqrt{\sin^2 \omega - \sin^2 \theta_{c,0}}
 \end{aligned} \tag{5.62}$$

The values of $\theta_{c,0}$ and $\theta_{c,s}$ can be obtained from eqs. (5.45) and (5.48), as a function of wavelength λ . For geometries (a) and (b), the values of ω and $q_{z,i}$ can then be obtained from eqs. (5.61) and (5.62), respectively, as a function of wavelength λ . Therefore, $q_{z,i}$ can be plotted versus ω for different λ s, which is the boundary of the unaccessible range of ω . This figure is useful for us to determine the range of ω which is meaningful in the experiments. For example, at the peak position of the first order Bragg peak $q_{z,i} = 0.02 \text{ \AA}^{-1}$ (indicated by the dashed orange line), it makes no sense to measure in the range $0.76^\circ < \omega < 1.26^\circ$. This explains why there is a gap in our data between $\omega = 0.7^\circ$ and $\omega = 1.4^\circ$.

Fig. 5.13 shows the plots of $q_{z,i}$ versus $q_{x,i}$ calculated for different wavelength λ s. This figure is very similar to Fig. 2 (b) in ref [61]. In their case the external scattering vector $q_{z,0}$ is plotted versus $q_{x,0}$ for constant $q_{z,i}$, while in our case the internal scattering vector $q_{z,i}$ is plotted versus $q_{x,i}$ for constant $q_{z,0}$. Therefore, the bending tendency of the curves is contrary to each other.

5.2 Monochromatic reflectometer MORPHEUS

The reflectometer AMOR works with a vertical scattering geometry (Fig. 5.1, a side view), while the reflectometer MORPHEUS works with a horizontal scattering geometry (Fig. 5.14, a top view), i.e., ω and 2θ change in a horizontal plane. While the upper limit of ω is about 10° in the case of AMOR, the accessible ranges of ω and 2θ are greatly enlarged in the case of MORPHEUS. Basically, our experiments were performed

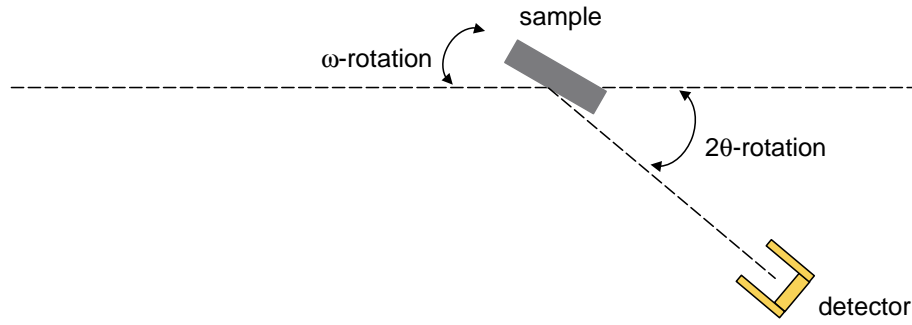


Figure 5.14: Top view of the scattering geometry of the reflectometer MORPHEUS at SINQ. The reflectometer MORPHEUS works with a horizontal scattering geometry.

at AMOR, with several measurements at higher angles of incidence performed at MORPHEUS to give complementary data to those obtained from AMOR. The reflectometer MORPHEUS works in a monochromatic mode with a selected beam wavelength 4.74 \AA by a graphite monochromator used in conjunction with a polycrystalline Be filter. The ω -rotation of the reflectometer is from -170° to $+188^\circ$, and the 2θ -rotation is from -125° to $+130^\circ$. The detector is a ^3He single detector.

5.3 Small-angle scattering SANS-II

Fig. 5.15 shows a sketch of the small-angle scattering instrument SANS-II at SINQ. The wavelength of the beam is selected to be 6.37 \AA by a neutron velocity selector.

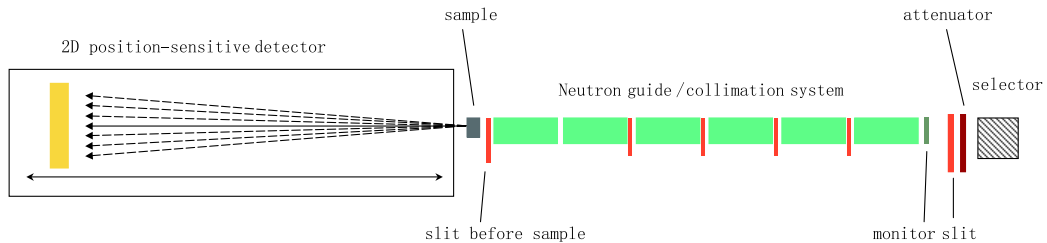


Figure 5.15: Sketch of the overall instrumental setup of the small-angle neutron scattering instrument SANS-II at SINQ.

The neutron guide consists of movable one-meter evacuated tubes and the length of the guide can be adjustable from one to six meters. Here we used five meters for the neutron guide. With a slit of diameter 16 mm installed at the end of each tube, the neutron guide serves at the same time as a beam collimator. The pinhole size before the sample is 7.32 mm in diameter. The detector is a ^3He area detector of 64 cm in diameter and 128×128 pixels. The detector can be moved continuously from one to six meters away from the sample position. In our experiments, the sample-to-detector distance is 5 m. The maximum q accessible is

$$q_{max} = \frac{4\pi}{\lambda} \sin \frac{(2\theta)_{max}}{2} \quad (5.63)$$

where $(2\theta)_{max}$ is the maximum scattering angle which is calculated as

$$(2\theta)_{max} = \arctan \frac{64 \text{ cm}}{2 \times 5 \text{ m}} \approx 3.66^\circ \quad (5.64)$$

Substituting eq. (5.64) into eq. (5.63), we obtain

$$q_{max} \approx 0.063 \text{ \AA}^{-1} \quad (5.65)$$

The lower limit of q is about 0.01 \AA^{-1} , due to the size of the primary beam. The unattenuated primary beam is so much stronger than the scattered beam that the detector is not capable to measure both under similar conditions. Therefore each measurement consists of two individual steps, i.e., to measure the primary beam with an attenuator which reduces the intensity and protects the detector, and to measure the scattered beam without an attenuator but with the help of a beamstop which blocks the primary beam. The data which are useful to us and will be shown in chapter 6 are from the second step measurement.

Chapter 6

Lamellar orientation under competing external fields

As described in chapter 4, P(dS-b-MMA) block copolymer films of $0.26\ \mu\text{m}$ or $0.86\ \mu\text{m}$ thick were prepared by spin-coating and subsequent annealing. The first annealing was done in vacuum at $200\ ^\circ\text{C}$ for 72 h. The second annealing was done in N_2 at the same temperature for 15 h, usually with the application of an electric field. During the second annealing, an upper electrode and a weight of about 0.5 kg (corresponding to a compressive stress of about 1000 Pa) were introduced to the system. The samples are listed in table 6.1, and the names of the samples will be referred to in this chapter. In this chapter, the complementary results of reflectivity and small-angle scattering

sample	$d/\mu\text{m}$	1 st annealing	2 nd annealing
NOV04A	0.26	yes	no
NOV04C	0.26	yes	yes, $E = 4\ \text{V}/\mu\text{m}$
NOV04D	0.26	yes	yes, $E = 16\ \text{V}/\mu\text{m}$
NOV04E	0.26	yes	yes, $E = 48\ \text{V}/\mu\text{m}$
AUG05B	0.26	yes	yes, $E = 2\ \text{V}/\mu\text{m}$
AUG05C	0.26	yes	yes, $E = 8\ \text{V}/\mu\text{m}$
AUG05D	0.26	yes	yes, $E = 12\ \text{V}/\mu\text{m}$
AUG04B	0.86	yes	no
AUG04C	0.86	yes	yes, $E = 1\ \text{V}/\mu\text{m}$
AUG04G	0.86	yes	yes, $E = 32\ \text{V}/\mu\text{m}$
AUG04H	0.86	yes	yes, $E = 47\ \text{V}/\mu\text{m}$
NOV05D	0.86	yes	yes, without E
NOV05C	0.86	yes	yes, $E = 0.1\ \text{V}/\mu\text{m}$
NOV05E	0.86	yes	yes, $E = 12\ \text{V}/\mu\text{m}$

Table 6.1: List of samples, where d is the film thickness and E is the strength of the applied electric field.

experiments on these samples will be shown and discussed. While reflectivity is sensitive to lamellae aligned parallel to the substrate, small-angle scattering in transmission is sensitive to lamellae aligned perpendicular to the substrate. A quantitative analysis of the internal structure of the films can be made from the combined data. We will start from the analysis of reflectivity data using the software package Parratt32 (see section 3.2.4), discussing on the effects of the first annealing, the upper electrode and the compressive stress during the second annealing, and the effects of electric fields,

respectively. The small-angle scattering data will then be shown and complement to the reflectivity data. Finally, a discussion on the formation of the film structures observed will be given based on the combined data of reflectivity and small-angle scattering.

6.1 Reflectivity

6.1.1 Pure silicon wafer

Polished silicon wafers have a typical surface roughness of about 5 Å, and a native SiO₂ layer of about 3-5 nm thick formed on the surface exposed to air ¹. The reflectivity from a pure silicon wafer used in our experiments is shown in Fig. 6.1, compared with the calculated results using Parratt32 from the models shown in the inset. Model 1 involves

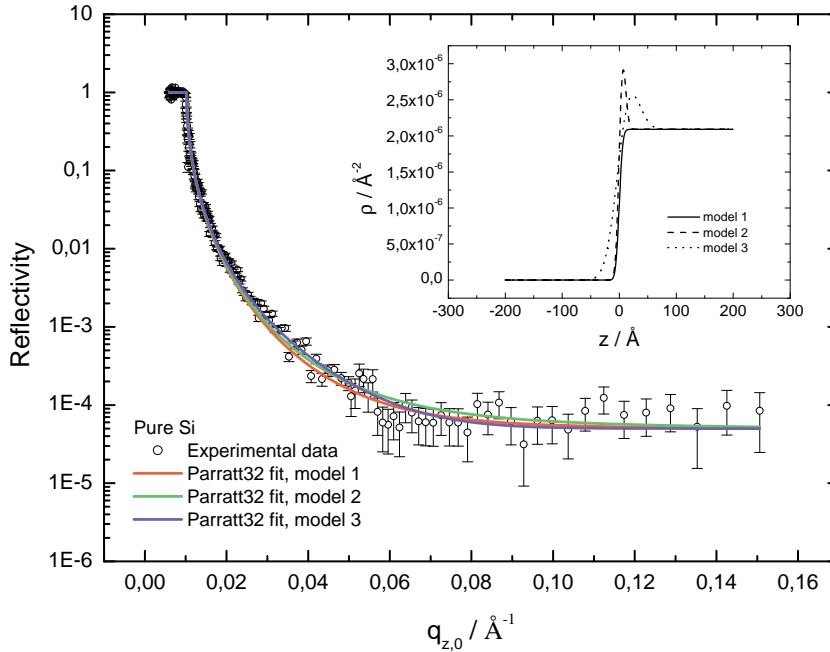


Figure 6.1: Reflectivity from a pure silicon wafer, compared with the calculated results using Parratt32 from the models shown in the inset.

a single interface between air and the silicon wafer with an interfacial roughness of 5 Å. Model 2 involves an additional SiO₂ layer of thickness 10 Å to model 1. The interfacial roughnesses at the air/SiO₂ and the SiO₂/Si interfaces are both 5 Å. The scattering length densities of the materials are given in table 6.2. A constant background of 5E-5 is

	Si	SiO ₂	(C ₈ D ₈) _n	(C ₅ H ₈ O ₂) _n
$\rho \times 10^6 / \text{Å}^{-2}$	2.09	3.63	6.186	1.033

Table 6.2: Theoretical scattering length densities ρ for the materials involved in our system.

used in the calculation. The background of the reflectivity measurements comes mostly from the general neutron background in the experimental hall, therefore it is reasonable to assume a constant background in the calculation. As can be seen, the influence of the

¹Private communication with people from CrysTec GmbH, Berlin, Germany.

SiO₂ layer on the reflectivity is not remarkable. One possible reason is that the oxide layer is so thin that the influence of this layer is only seen at $q_{z,0}$ much larger than that measured here. For $d_{\text{SiO}_2} = 10 \text{ \AA}$, the first maximum in the Kiessig fringes is expected to be at $q_{z,i} = 2\pi/d_{\text{SiO}_2} \approx 0.628 \text{ \AA}^{-1}$, where $q_{z,i}$ is the z -component of the scattering vector in the copolymer medium. The z -component of the scattering vector which is measured in the air medium is then $q_{z,0} = \sqrt{q_{z,i}^2 + q_{c,0}^2} = \sqrt{0.628^2 + 0.0102^2} \text{ \AA}^{-1} \approx 0.6281 \text{ \AA}^{-1}$, where $q_{c,0}$ has a theoretical value of 0.0102 \AA^{-1} . The estimation shows that the influence of the oxide layer on the reflectivity is only seen at $q_{z,0} > 0.6281 \text{ \AA}^{-1}$. Moreover, as the reflectivity decreases with increasing $q_{z,0}$, any change in the reflectivity at such a large $q_{z,0}$ will not be visible because of the constant background used in the calculation. If the thickness of the SiO₂ layer becomes larger, e.g., 25 \AA as used in model 3, the interfacial roughnesses at both interfaces must be increased to 18 \AA in order to fit the data. Such a large roughness is not reasonable for polished silicon wafers.

6.1.2 Parameters used in Parratt32

From the reflectivity of the pure silicon wafer, we obtained useful information for the analysis of reflectivity data from the copolymer films. In the following analysis using Parratt32, we will fix the following conditions in order to agree with the analysis of the reflectivity from the silicon wafer:

- A constant background of 5E-5 will be used in the calculation;
- A SiO₂ layer of thickness 10 \AA will be involved in the model for calculation, and the interfacial roughnesses at the polymer/SiO₂ and the SiO₂/Si interfaces will both be 5 \AA .

Since we will use Parratt32 as the main tool for the analysis of reflectivity data, it will be convenient to list all the parameters used in the model (table 6.3). In addition, we

Parameters	Meaning
ρ_{PS}	scattering length density of PS
ρ_{PMMA}	scattering length density of PMMA
ρ_{Si}	scattering length density of silicon
ρ_{SiO_2}	scattering length density of SiO ₂
n	number of lamellar periods
d_p	lamellar period of the layered structure
$d_{p,\text{PS}}$	thickness of the PS block in one lamellar period
$d_{p,\text{PMMA}}$	thickness of the PMMA block in one lamellar period
σ	roughness at the PS/PMMA interfaces
σ_{air}	roughness at the air/polymer interface
σ_{bulk}	roughness at the SiO ₂ /substrate interface
d_{SiO_2}	thickness of the SiO ₂ layer
σ_{SiO_2}	roughness at the polymer/SiO ₂ interface

Table 6.3: Definitions of the parameters used in the model for calculation of reflectivity profiles using Parratt32.

will conform to the following principles when constructing the model of calculation in Parratt32:

- Firstly, $d_{p,PS}$ and $d_{p,PMMA}$ should be the same due to the symmetric volume fraction of the copolymer;
- Secondly, σ should be the same for each PS/PMMA interface due to the conformality between the layers;
- Thirdly, σ_{SiO_2} and σ_{bulk} should be consistent with the typical roughness for polished silicon wafers;
- Finally, σ_{air} can be different from σ , and should usually be smaller than σ because the surface tension tends to smoothen the surface.

The third principle is fulfilled by using $\sigma_{SiO_2} = \sigma_{bulk} = 5 \text{ \AA}$, which has already been mentioned above.

The resolution of the reflectivity measurements should not depend on the sample. For fixed instrumental settings, the resolution should always be the same. For the instrumental settings used in our experiments (see section 5.1.5), the resolution for the reflectivity measurements at an angle of incidence $\omega = 0.25^\circ$, 0.5° and 1° has been calculated and shown in Fig. 5.8. As can be seen, the reflectivity measured at $\omega = 1^\circ$ has the best resolution among the three. For this reason, we will take these data measured at $\omega = 1^\circ$ for the analysis using Parratt32. Since in the software it is not possible to input a continuously changed resolution with respect to q , we have used a stepwise resolution as shown in table 6.4.

$q/\text{\AA}^{-1}$	$\Delta q/\text{\AA}^{-1}$
$0 \leq q < 0.036$	0.0006
$0.036 \leq q < 0.044$	0.0008
$0.044 \leq q < 0.11$	0.0025

Table 6.4: Stepwise resolution used for calculation of reflectivity profiles in Parratt32.

6.1.3 Effects of first annealing, upper electrode and compressive stress

The first annealing was done without the application of any electric field, therefore the surface effects (see section 2.2) will be the only effects to align the lamellae in the films. As we know the PS component segregates to the air surface (due to a lower surface energy than PMMA) and the PMMA component segregates to the silicon substrate (because of its preferential interactions with the SiO_2 layer), a layered structure shown in Fig. 6.2 with alternative PS and PMMA blocks oriented parallel to the substrate is expected to be induced during the first annealing. Such a layered structure can be constructed into a model of density profile, e.g., shown in Fig. 6.3 for the sample NOV04A, with the SiO_2 layer mentioned above.

The reflectivity data from two films after the first annealing are shown in Fig. 6.4. The data from the thinner one, NOV04A ($0.26 \mu\text{m}$), can be fitted using the model shown in Fig. 6.3. In this model, the lamellar period d_p is determined from the position of the first order Bragg peak to be 320 \AA . The thicknesses of the blocks $d_{p,PS}$ and $d_{p,PMMA}$ are set as $d_p/2 = 160 \text{ \AA}$, respectively. The model involves a lamellar orientation throughout the film with $n = 8$, where n is determined by fitting the positions of the Kiessig fringes in the data. The total film thickness in the model corresponds to $8.5d_p$ for the

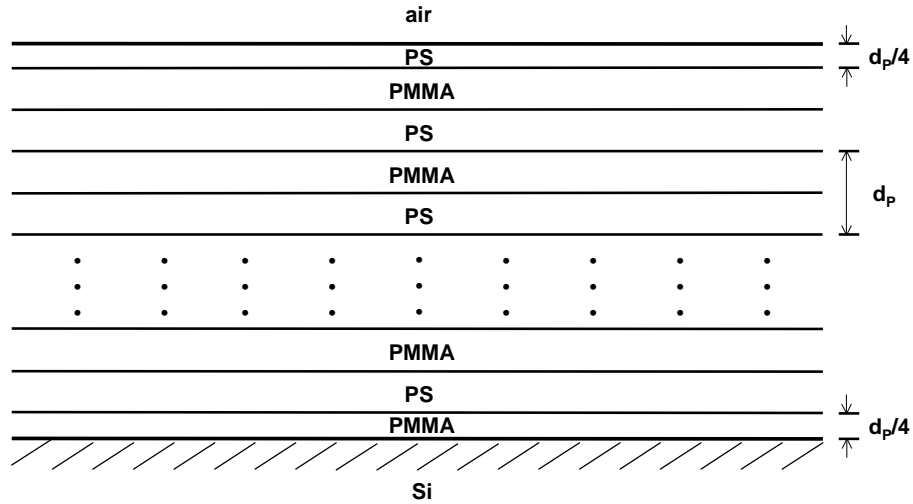


Figure 6.2: Layered structure with alternative PS and PMMA layers oriented parallel to the substrate, where d_p is the lamellar period of the structure.

antisymmetric wetting case. On the other hand, the film thickness obtained from the profile meter measurement is $0.26 \mu\text{m}$, which is consistent with the film thickness in the model. This indicates the lamellae in the film are completely oriented parallel to the substrate.

In the case of the thicker film, AUG04B ($0.86 \mu\text{m}$), n cannot be determined from the Kiessig fringes because they are not visible any more. In this case n is determined from the intensity of the higher (second and third) order Bragg peaks, because the intensity should be increased with increasing n if the interfacial roughnesses remain relatively unchanged. As can be seen, the intensity of the higher order peaks for the thicker film is comparable to that for the thinner film. Indeed, the reflectivity data from the thicker film cannot be fitted by a model with $n = 27$, which corresponds to a parallel orientation throughout the film. However, they can be roughly fitted by a model with $n = 5$, indicating a partial orientation in the film. This situation will not be changed even if the annealing time is prolonged to 168 h (Fig. 6.5).

In the previous models we have used, it is always assumed that a PS layer is adjacent to the air surface and a PMMA layer is adjacent to the silicon substrate. Although the assumption is consistent with our knowledge about the interactions between the copolymer and the surfaces, it should be checked by using different models shown in table 6.5. In addition, an upper electrode was attached to the copolymer film during

	layer adjacent to air/PDMS	layer adjacent to silicon
model 1	PS	PMMA
model 2	PMMA	PMMA
model 3	PMMA	PS
model 4	PS	PS

Table 6.5: Models with different types of layers adjacent to the surfaces.

the second annealing, so that the upper medium was changed from air to polydimethylsiloxane (PDMS). This might have influence on the interactions between the copolymer film and the upper medium, which probably leads to a different type of layer adjacent to the upper medium.

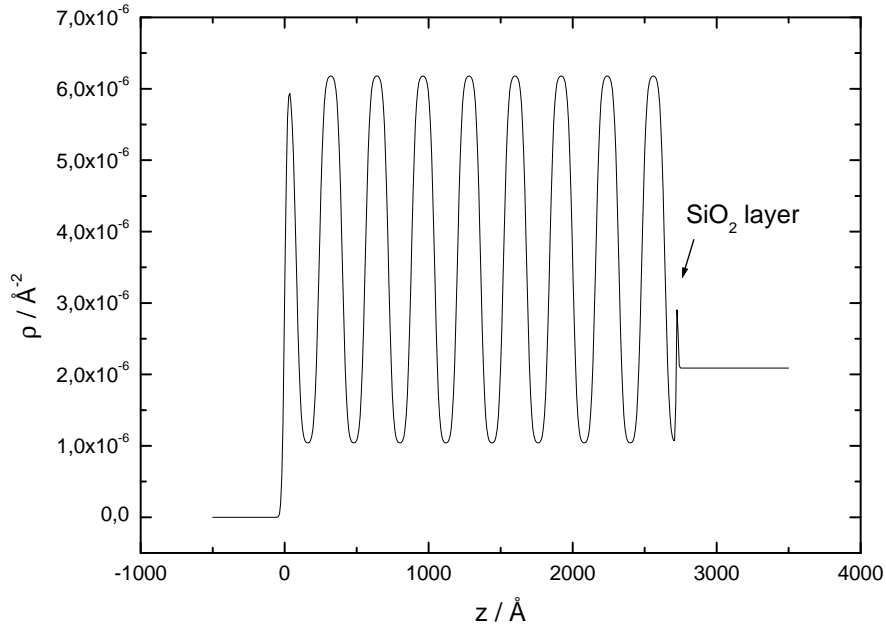


Figure 6.3: Model of density profile used for fitting the reflectivity data from the sample NOV04A ($d = 0.26 \mu\text{m}$, 1st annealing).

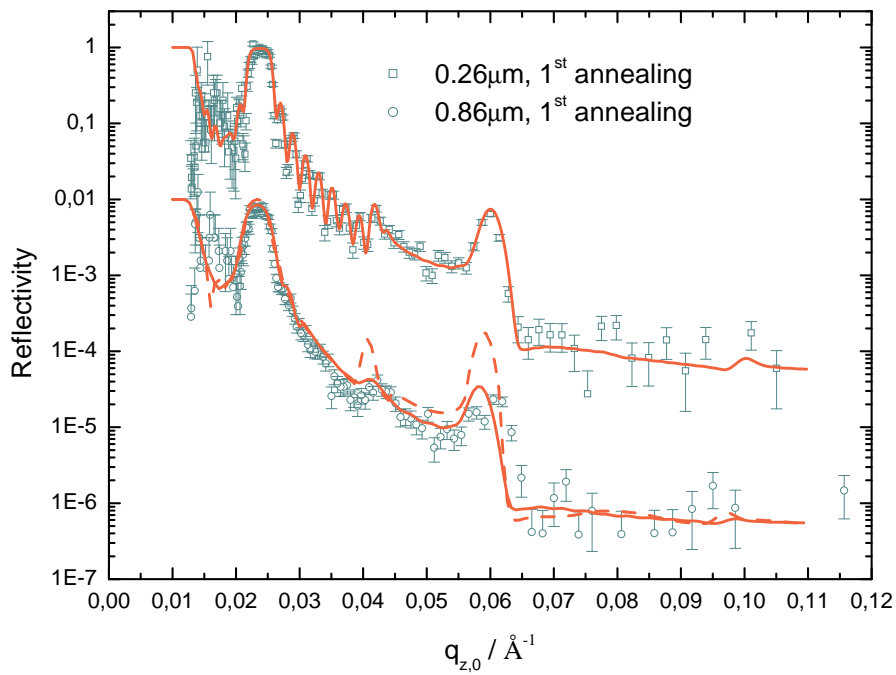


Figure 6.4: Reflectivity data obtained from the samples NOV04A ($d = 0.26 \mu\text{m}$, 1st annealing) and AUG04B ($d = 0.86 \mu\text{m}$, 1st annealing). The lines correspond to the fits to the data using Parratt32. The fit for the thinner film is obtained from the model shown in Fig. 6.3. The fits for the thicker film are obtained from a model with $n = 5$ (solid line) or $n = 27$ (dashed line), respectively. The data are offset for clarity.

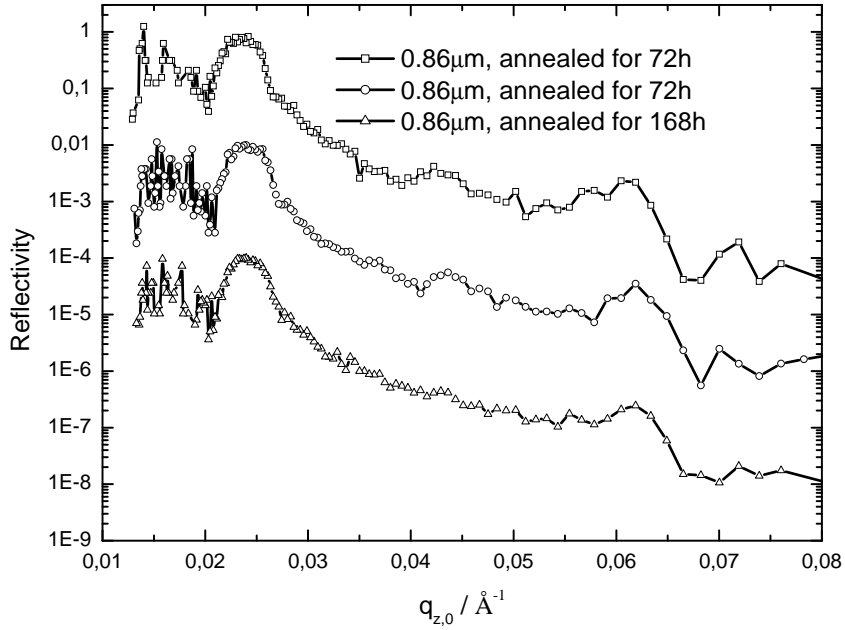


Figure 6.5: Reflectivity data obtained from films of $0.86 \mu\text{m}$: AUG04B (annealed for 72 h), JUN04F (annealed for 72 h) and JUN04A (annealed for 168 h). The data are offset for clarity.

Fig. 6.6 shows the reflectivity data obtained from the films NOV04A and NOV04C. Both films have a thickness of $0.26 \mu\text{m}$. The difference is one of them was prepared by only the first annealing while the other was prepared by a subsequently annealing with $E = 4 \text{ V}/\mu\text{m}$. Here the data are fitted using models with a parallel orientation throughout the film, with different types of adjacent layers shown in table 6.5. As can be seen, in both cases, model 1 gives the best fits, while the other models cannot give acceptable fits to the data. Especially, if models 2 or 4 (which correspond to symmetric wetting cases) is used, the positions of the Kiessig fringes cannot be fitted. This is because the total film thickness in the symmetric and antisymmetric cases corresponds to nd_p and $(n + 1/2)d_p$, respectively, while the Kiessig fringes are characteristic of the film thickness. The fact that both data can be best fitted by model 1 demonstrates the assumption about the adjacent layers in our model is correct, and the type of the layer adjacent to the upper medium (air or PDMS) is not changed by the application of the upper electrode. Since the PDMS molecules are nonpolar, as well as the air molecules, a lower surface energy is still expected for the PS component which is also nonpolar. In this way it can be understood that the application of the upper electrode has little effect on the surface interactions between the copolymer film and the upper medium. It should be mentioned that, a slightly decrease in the lamellar period was observed from the data obtained after the second annealing. However, this is only attributed to a variation within the experimental error.

During the second annealing, a weight of about 0.5 kg which produces a vertical compressive stress of about 1000 Pa was put on top of the sample in order to keep the whole setup compact and to prevent the upper electrode from deforming upon heating. The effect of the compressive stress was checked by comparing the reflectivity data from two films of $0.86 \mu\text{m}$, AUG04B and NOV05D. The sample AUG04B was prepared by only the first annealing, while the sample NOV05D was prepared by a subsequently annealing with the compressive stress but without an electric field. The

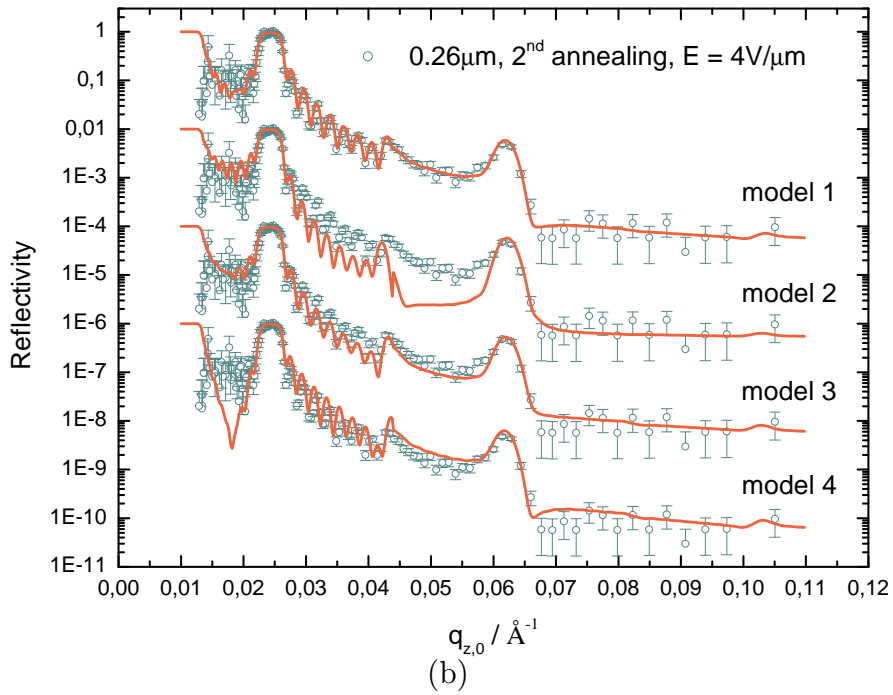
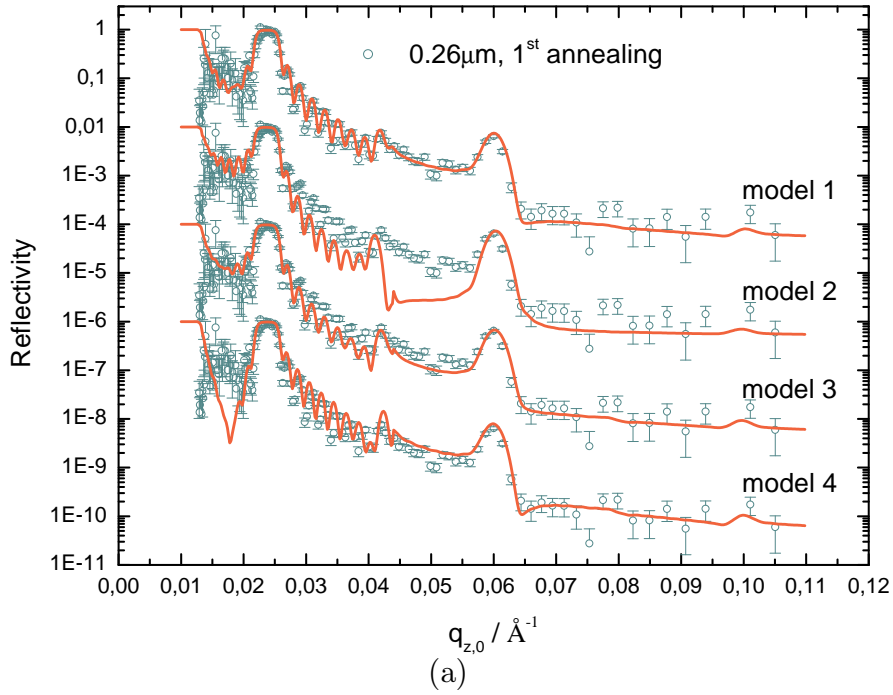


Figure 6.6: Reflectivity data obtained from the samples (a) NOV04A ($d = 0.26 \mu\text{m}$, 1st annealing) and (b) NOV04C ($d = 0.26 \mu\text{m}$, 2nd annealing, $E = 4 \text{V}/\mu\text{m}$). The data are fitted using models with different types of adjacent layers (table 6.5).

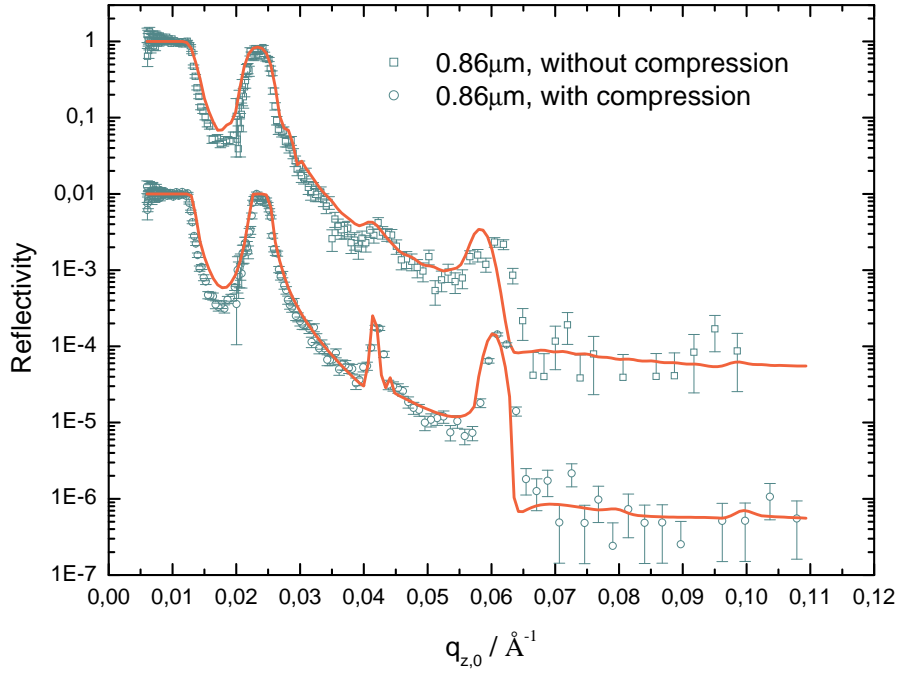


Figure 6.7: Reflectivity data obtained from the samples AUG04B ($d = 0.86 \mu\text{m}$, 1st annealing) and NOV05D ($d = 0.86 \mu\text{m}$, 2nd annealing with compressive stress only). The lines correspond to the fits to the data using Parratt32. The data from AUG04B can be fitted by a model with $n = 5$, while the data from NOV05D can be fitted by a model with $n = 27$. The data are offset for clarity.

reflectivity data from these two films are shown in Fig. 6.7. In both cases, the data are a combination of those measured at $\omega = 1^\circ$ (for $q_{z,0} > 0.02 \text{ \AA}^{-1}$) and $\omega = 0.25^\circ$ (for $q_{z,0} < 0.02 \text{ \AA}^{-1}$). The measurement at $\omega = 0.25^\circ$ enables us to see the critical edge in reflectivity. Apparently, the intensity of the higher order Bragg peaks increases after the second annealing without an electric field. As shown before, the data from AUG04B can only be roughly fitted by a model with $n = 5$, indicating a partial orientation of the lamellae. However, the data from NOV05D can be fitted by a model with $n = 27$, i.e., a parallel orientation throughout the film. Combined with the data from small-angle scattering experiments (which will be shown in section 6.2), we conclude that the mechanical stress induces an instability in the originally partially oriented structure, and favors a completely parallel orientation of the lamellae.

It should be mentioned that the model with $n = 5$ used for fitting the data from AUG04B is not correct because the total film thickness is not consistent with that obtained from the profile meter measurement. A more reasonable model should be constructed. In the simplest case, the rest of the film thickness could be compensated by a homogeneous layer with the scattering length density being the average of the two components. However, the fit to the data using such a model is not successful. A better fit to these data is not available at this point.

6.1.4 Average scattering length density and partial mixing

As we examine the details of the data shown in Fig. 6.7, we find the following discrepancies between the data and the fits: (i) the critical edge in the data occurs at a smaller $q_{c,0}$ than in the fits; (ii) the positions of the higher (second and third) order Bragg peaks

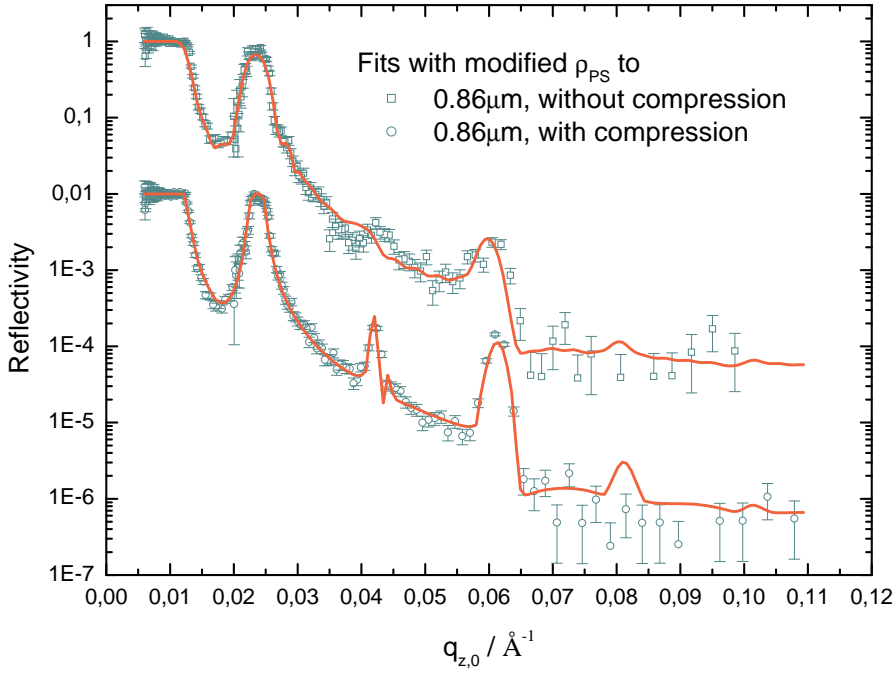


Figure 6.8: Reflectivity data obtained from the samples AUG04B and NOV05D, fitted by using the modified scattering length density of the PS block. The data are offset for clarity.

in the data occur at larger $q_{z,0}$ s than in the fits; (iii) the first order Bragg peak in the data is narrower than in the fits. Discrepancy (i) is an indication of a decrease in the average scattering length density $\bar{\rho}$ of the copolymer, although this should not happen if the copolymer is incompressible. A decrease in $\bar{\rho}$ leads to an increase in the refractive index $n_1 (= 1 - \bar{\delta} = 1 - \bar{\rho}\lambda^2/2\pi)$, and a decrease in the critical angle $\theta_c (= \arccos n_1)$, and finally a decrease in $q_{c,0} (= 4\pi \sin \theta_c / \lambda)$. Discrepancy (ii) can be regarded as a result of the decrease in $q_{c,0}$, because $q_{z,0}$ is related to $q_{z,i}$ through $q_{z,0} = \sqrt{q_{z,i}^2 + q_{c,0}^2}$, while the relative positions of the Bragg peaks should be fixed in terms of $q_{z,i}$. Discrepancy (iii) is an indication of a decrease in the scattering contrast between the two components, therefore a partial mixing of the components.

Given these hints, we tried a smaller value of ρ_{PS} , $5 \times 10^{-6} \text{ \AA}^{-2}$ instead of $6.186 \times 10^{-6} \text{ \AA}^{-2}$ predicted for pure PS, while keeping the value of ρ_{PMMA} equal to the theoretical one. The calculated reflectivity profiles for the samples AUG04B and NOV05D using this modified scattering length density of PS (or PS-rich phase) are shown in Fig. 6.8, compared with the measured data. It can be seen that discrepancies (i)-(iii) can be minimized by using the modified ρ_{PS} . As the decrease in the scattering contrast indicates a 23% mixing of PMMA in the PS-rich phase, the thickness of the PS block in the model should be correspondingly increased as shown in table 6.6.

	$\rho_{PS} \times 10^6 / \text{\AA}^{-2}$	n	$d_{p,PS} / \text{\AA}$	$d_{p,PMMA} / \text{\AA}$	$\sigma / \text{\AA}$	$\sigma_{air} / \text{\AA}$
AUG04B	6.186	5	164	164	28	20
	5	5	172	146	25	15
NOV05D	6.186	27	159	161	28	20
	5	27	172	142	24	10

Table 6.6: Parameters used in calculating the reflectivity profiles in Parratt32.

Now let us prove that the average scattering length density $\bar{\rho}$ of the copolymer should not become smaller if the copolymer is incompressible. Initially in a volume v , the PS and PMMA components have a volume fraction f_{PS} and f_{PMMA} , respectively. If after the partial mixing the volumes of the PS-rich and PMMA-rich phases become v_1 and v_2 , and the volume fractions of PS and PMMA in the two phases are denoted as $\varphi_{\text{PS},1}$, $\varphi_{\text{PS},2}$, $\varphi_{\text{PMMA},1}$, and $\varphi_{\text{PMMA},2}$, respectively, the average scattering length densities in phase 1 and phase 2 will be

$$\rho_1 = \rho_{\text{PS}} \varphi_{\text{PS},1} + \rho_{\text{PMMA}} \varphi_{\text{PMMA},1} \quad (6.1)$$

$$\rho_2 = \rho_{\text{PS}} \varphi_{\text{PS},2} + \rho_{\text{PMMA}} \varphi_{\text{PMMA},2} \quad (6.2)$$

The masses of the PS and PMMA components are conserved, thus we have

$$\varphi_{\text{PS},1} v_1 + \varphi_{\text{PS},2} v_2 = f_{\text{PS}} v \quad (6.3)$$

$$\varphi_{\text{PMMA},1} v_1 + \varphi_{\text{PMMA},2} v_2 = f_{\text{PMMA}} v \quad (6.4)$$

The average scattering length density $\bar{\rho}$ of the copolymer after the partial mixing is

$$\begin{aligned} \bar{\rho} &= \rho_1 \frac{v_1}{v} + \rho_2 \frac{v_2}{v} \\ &= \rho_{\text{PS}} \varphi_{\text{PS},1} \frac{v_1}{v} + \rho_{\text{PMMA}} \varphi_{\text{PMMA},1} \frac{v_1}{v} + \rho_{\text{PS}} \varphi_{\text{PS},2} \frac{v_2}{v} + \rho_{\text{PMMA}} \varphi_{\text{PMMA},2} \frac{v_2}{v} \\ &= \rho_{\text{PS}} \left(\varphi_{\text{PS},1} \frac{v_1}{v} + \varphi_{\text{PS},2} \frac{v_2}{v} \right) + \rho_{\text{PMMA}} \left(\varphi_{\text{PMMA},1} \frac{v_1}{v} + \varphi_{\text{PMMA},2} \frac{v_2}{v} \right) \\ &= \rho_{\text{PS}} f_{\text{PS}} + \rho_{\text{PMMA}} f_{\text{PMMA}} \end{aligned} \quad (6.5)$$

showing that $\bar{\rho}$ should be a constant. Therefore, we conclude that the decrease in $\bar{\rho}$ is not a major effect. It might be due to a small error in calculating the values of $q_{z,0}$, as in the case that e.g., the distance L from the chopper to the detector was not correctly measured. Russell et al. [62] also reported a partial mixing of the PS and PMMA component for their copolymer films. What is surprising is that the average scattering length density in their case was also changed. In spite of this, the partial mixing was not observed for our films of $0.26 \mu\text{m}$. This might be due to the fact that the surface-induced ordering [62, 63] is more dominant in the thinner films than in the thicker films, therefore a partial mixing is not easy to occur in the thinner films.

For symmetric diblock copolymers, it is predicted by the theory that even-order Bragg peaks will vanish, and the intensity of these peaks will be increased with the increasing degree of asymmetry. This indicates a deviation of the ratio $d_{p,\text{PS}}/d_{p,\text{PMMA}}$ from 1 will lead to an increase in the relative intensity of the second order peak to that of the third order peak. This can be seen from the fits shown in Fig. 6.8, using the modified ρ_{PS} and a correspondingly enlarged thickness of the PS (PS-rich) block. This is not reasonable, especially for the fourth order peak which is not seen in the measured data. Therefore, this is an additional argument for using the theoretical value of ρ_{PS} predicted for pure PS.

6.1.5 Effects of electric fields

Fig. 6.9 shows the reflectivity data obtained from the films of $0.26 \mu\text{m}$, annealed under different electric fields. The data from the film with only the first annealing are also shown for comparison. Apparently, all the films (except NOV04E) represent reflectivity data which are quite similar in terms of the intensity of the higher (second and third)

order Bragg peaks. As mentioned before, this indicates the number of layers which are parallel to the substrate is nearly the same for these films. Indeed, all the data (except those for NOV04E) can be fitted using Parratt32 by a model with a parallel orientation throughout the film. The fitting results and the parameters used in the models are shown in Fig. 6.10 and table 6.7, respectively. There is a dramatic decrease in the

	$d/\mu\text{m}$	$E/[\text{V}/\mu\text{m}]$	n	$d_{p,\text{PS}}/\text{\AA}$	$d_{p,\text{PMMA}}/\text{\AA}$	$\sigma/\text{\AA}$	$\sigma_{\text{air}}/\text{\AA}$
NOV04A	0.26	0 (1 st ann.)	8	160	160	25	15
AUG05B	0.26	2	9	154	154	27	22
NOV04C	0.26	4	8	155	155	25	15
AUG05C	0.26	8	8	157	157	27	25
AUG05D	0.26	12	8	158	158	27	30
NOV04D	0.26	16	8	162	162	27	20

Table 6.7: Parameters used in the Parratt32 calculations shown in Fig. 6.10.

intensity of the third order peak in the data from NOV04E with $E = 48 \text{ V}/\mu\text{m}$. What can be inferred from the reflectivity data is only that the number of layers parallel to the substrate in this film is much less than that for the other films. While a completely parallel orientation was achieved in the other films of $0.26 \mu\text{m}$, only a partially parallel orientation was observed in this film which is obviously due to the effect of the strong electric field. Another observation from Fig. 6.9 is an approximately 4% decrease in the lamellar period d_p from the sample NOV04A to the sample AUG05B, and a slightly increase in d_p with the increasing electric field strength. However, as will be shown in section 6.4.2, the observation cannot be attributed to the effects of the compressive stress or the electric field. Therefore, we only attribute this to a variation within the experimental error.

Fig. 6.11 shows the reflectivity data obtained from the films of $0.86 \mu\text{m}$, annealed under different electric fields. The data from the two films without an electric field (AUG04B and NOV05D) are also shown for comparison. As discussed before, the lamellae are not completely oriented parallel to the substrate after the first annealing, indicated by the weaker intensity of the higher order Bragg peaks from the sample AUG04B than from the other films. The compressive stress applied during the second annealing alone, induces an instability in the originally partially oriented structure, and favors a completely parallel orientation of the lamellae. This is inferred from the reflectivity data of the sample NOV05D, which can be fitted by a model with a parallel orientation throughout the film. This situation remains the same for the films annealed under an electric field weaker than $\sim 20 \text{ V}/\mu\text{m}$, as indicated by the Parratt32 fits to the data from these films (Fig. 6.12 and table 6.8). The intensity of the third order peak

	$d/\mu\text{m}$	$E/[\text{V}/\mu\text{m}]$	n	$d_{p,\text{PS}}/\text{\AA}$	$d_{p,\text{PMMA}}/\text{\AA}$	$\sigma/\text{\AA}$	$\sigma_{\text{air}}/\text{\AA}$
AUG04B	0.86	0 (1 st ann.)	5	164	164	28	20
NOV05D	0.86	0 (2 nd ann.)	27	159	161	28	20
NOV05C	0.86	0.1	27	159	161	28	20
AUG04C	0.86	1	27	161	159	28	20
NOV05E	0.86	12	27	159	161	28	20
AUG04G	0.86	32	12	150	166	28	20
AUG04H	0.86	47	10	148	166	28	20

Table 6.8: Parameters used in the Parratt32 calculations shown in Fig. 6.12.

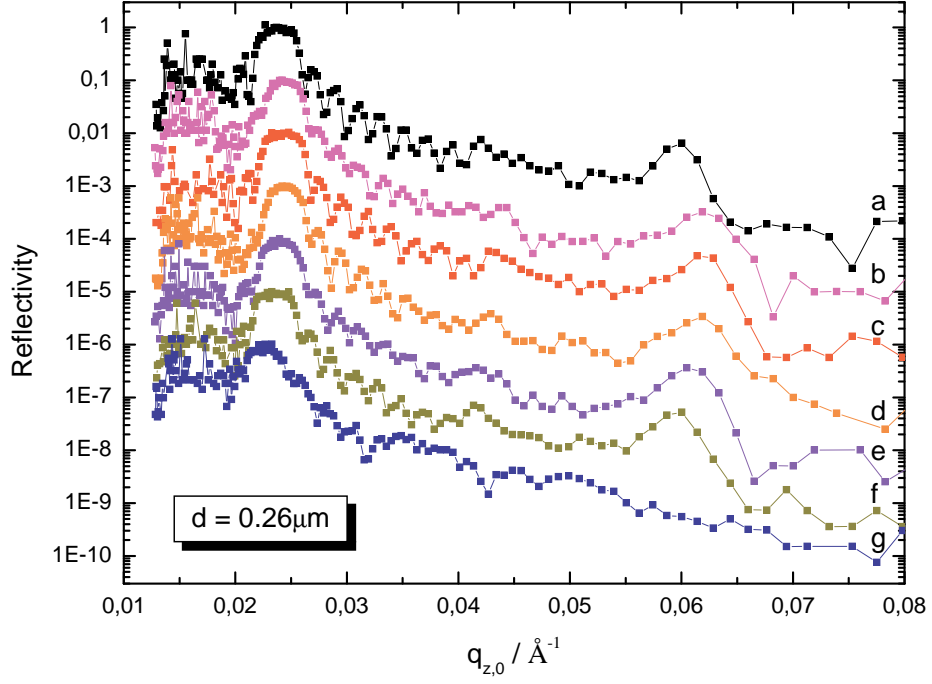


Figure 6.9: Reflectivity data obtained from films of $0.26 \mu\text{m}$: (a) NOV04A (1^{st} annealing), (b) AUG05B ($E = 2 \text{ V}/\mu\text{m}$), (c) NOV04C ($E = 4 \text{ V}/\mu\text{m}$), (d) AUG05C ($E = 8 \text{ V}/\mu\text{m}$), (e) AUG05D ($E = 12 \text{ V}/\mu\text{m}$), (f) NOV04D ($E = 16 \text{ V}/\mu\text{m}$), and (g) NOV04E ($E = 48 \text{ V}/\mu\text{m}$). The data are offset for clarity.

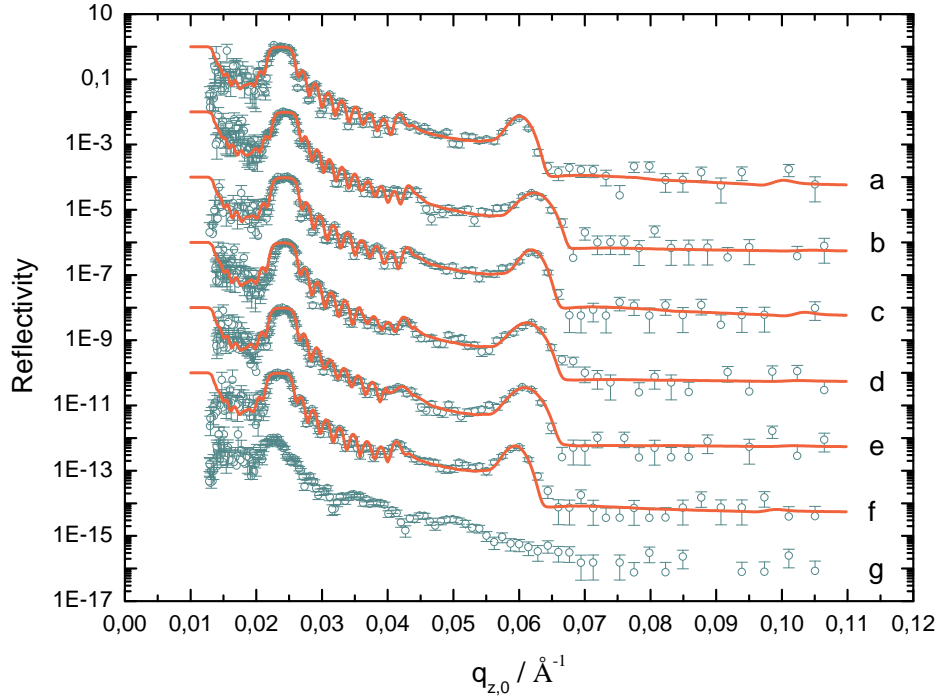


Figure 6.10: Parratt32 fits to the data shown in Fig. 6.9. The data are offset for clarity.

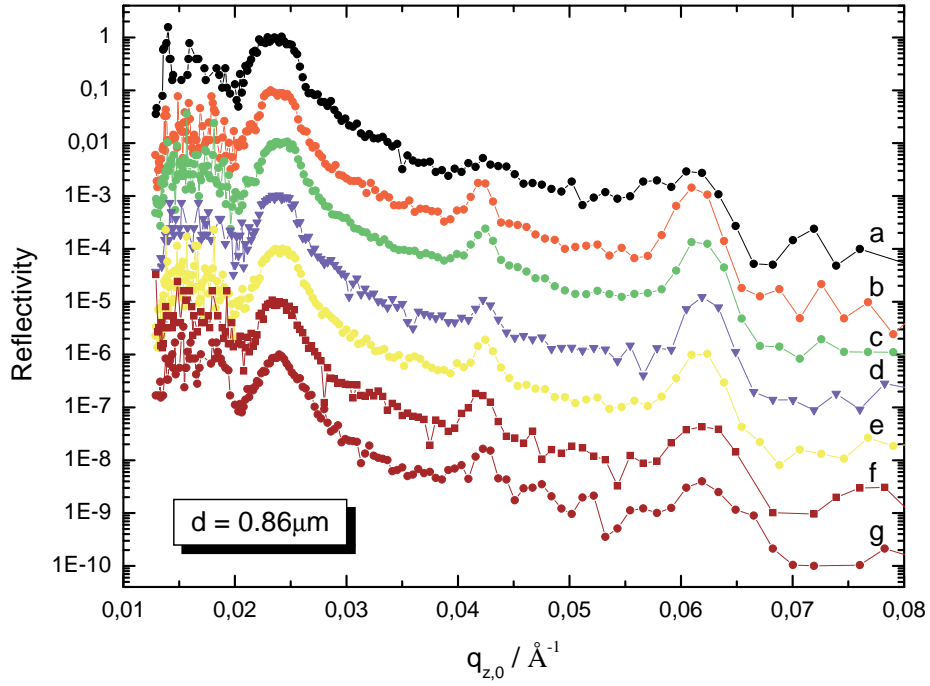


Figure 6.11: Reflectivity data obtained from films of $0.86 \mu\text{m}$: (a) AUG04B (1^{st} annealing), (b) NOV05D (2^{nd} annealing, without E), (c) NOV05C ($E = 0.1 \text{ V}/\mu\text{m}$), (d) AUG04C ($E = 1 \text{ V}/\mu\text{m}$), (e) NOV05E ($E = 12 \text{ V}/\mu\text{m}$), (f) AUG04G ($E = 32 \text{ V}/\mu\text{m}$), and (g) AUG04H ($E = 47 \text{ V}/\mu\text{m}$). The data are offset for clarity.

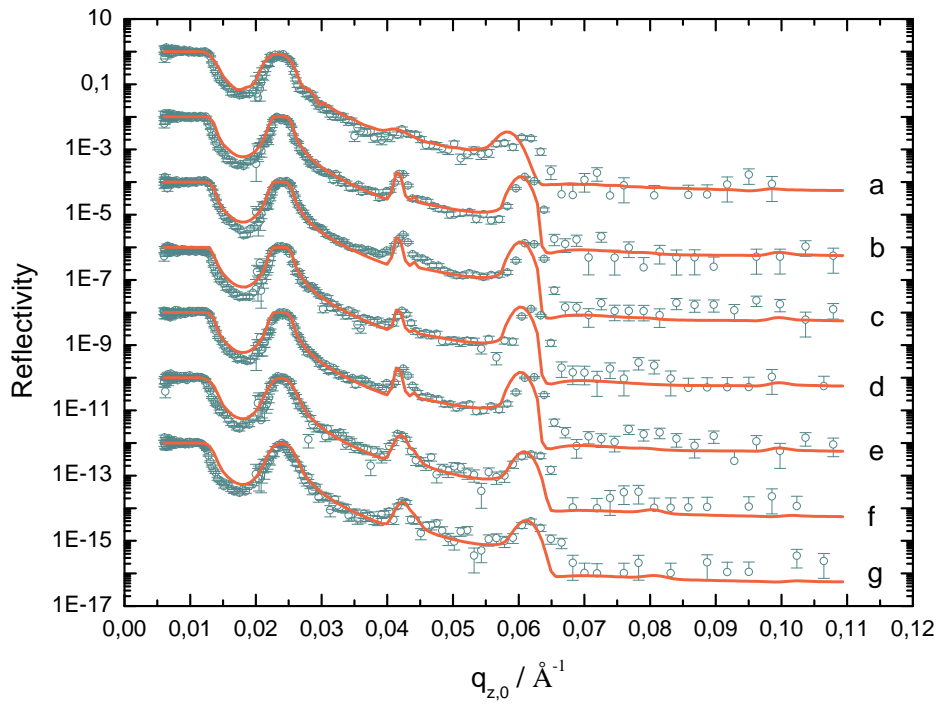


Figure 6.12: Parratt32 fits to the data shown in Fig. 6.11. The data are offset for clarity.

becomes lower if the field strength is above $\sim 30 \text{ V}/\mu\text{m}$. In this case, the reflectivity data can only be fitted by a model with $n \sim 10$, indicating the electric field induces or stabilizes the lamellar orientation perpendicular to the substrate (evidenced by the small-angle scattering experiments).

6.2 Small-angle scattering

The SANS patterns obtained from the films of $0.26 \mu\text{m}$ are shown in Fig. 6.13. At

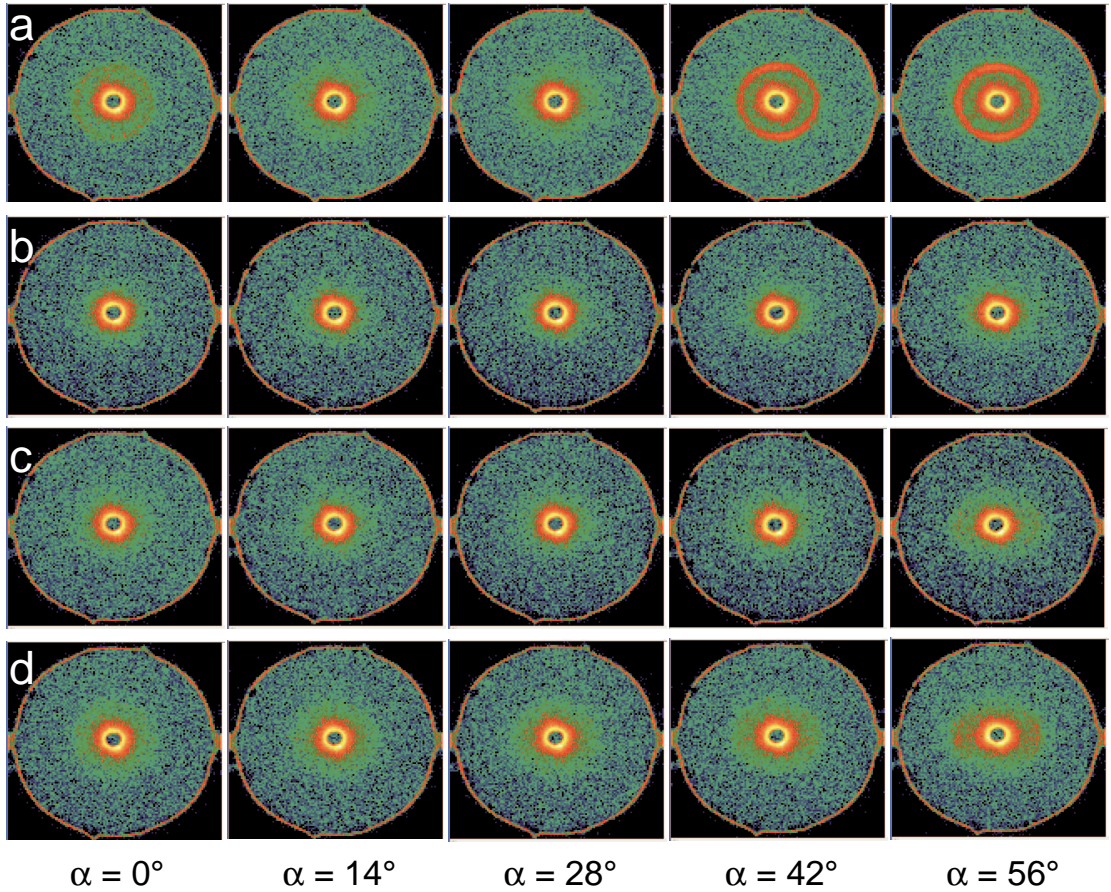


Figure 6.13: SANS patterns measured at different angles of incidence α , obtained from films of $0.26 \mu\text{m}$: (a) NOV04A (1st annealing), (b) NOV04C ($E = 4 \text{ V}/\mu\text{m}$), (c) NOV04D ($E = 16 \text{ V}/\mu\text{m}$), and (d) NOV04E ($E = 48 \text{ V}/\mu\text{m}$).

$\alpha = 0^\circ$, no or very little Bragg intensity was observed for all these films, indicating no or very little amount of lamellae are oriented perpendicular to the substrate. As α increases, lamellae with inclination angles $\gamma \geq (90^\circ - \alpha)$ will be observed (see section 3.4). The lack of Bragg intensity in the patterns up to $\alpha = 56^\circ$ is consistent with the results of reflectivity from these films (except NOV04E), i.e., the lamellae in the films are completely oriented parallel to the substrate. The Bragg intensity observed at $\alpha = 42^\circ$ and 56° from the sample NOV04A [Fig. 6.13 (a)] is most likely due to the remaining copolymer on the back of the wafer after spin-coating. It is not easy to clean completely the remaining copolymer which are usually near to the edge of the wafer and therefore will probably be detected at higher angles. For the sample NOV04E with $E = 48 \text{ V}/\mu\text{m}$, the reflectivity data indicate the lamellae are not completely parallel to the substrate, meanwhile the SANS data show no lamellae oriented perpendicular

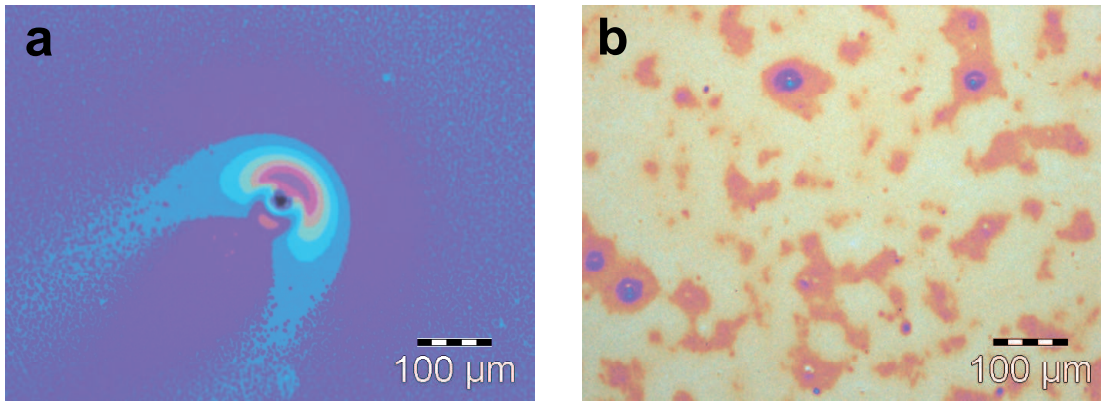


Figure 6.14: Optical micrographs obtained from the sample NOV04E ($d = 0.26 \mu\text{m}$): (a) after the first annealing, and (b) after the second annealing with the application of an electric field $E = 48 \text{ V}/\mu\text{m}$.

to the substrate. The film, observed under microscope (Fig. 6.14), shows an inhomogeneous surface structure after the application of the electric field in contrast to the homogeneous structure observed after the first annealing. This indicates the film might be partially destroyed by an instability induced by inhomogeneous electric fields similar to that described in ref [58]. Interestingly, two equatorial points of Bragg intensity were observed at $\alpha = 56^\circ$ from NOV04E. These are indications of lamellae aligned at $\gamma = (90^\circ - \alpha) \sim 30^\circ$ with respect to the substrate. In order to check the lamellar structures aligned at $\gamma < 30^\circ$, we need to go to higher angles of incidence. However, this is not possible because α is restricted to about 60° due to the size of the primary beam. As will be shown in section 6.3, test measurements (diffuse scattering) on this point have been done at the reflectometer MORPHEUS.

The SANS patterns obtained from the films of $0.86 \mu\text{m}$ are shown in Fig. 6.15. Consistent with the results of reflectivity from the samples NOV05D, NOV05C, AUG04C, and NOV05E, they show no or very little Bragg intensity in the SANS patterns [Fig. 6.15 (b)-(e)], indicating a completely parallel orientation of the lamellae. The observation of the two equatorial points of Bragg intensity at $\alpha = 56^\circ$ from NOV05E with $E = 12 \text{ V}/\mu\text{m}$ is similar to that for the thinner film with $E = 48 \text{ V}/\mu\text{m}$. For the samples AUG04B and AUG04H, with a partially parallel orientation inferred from the reflectivity data, the SANS patterns [Fig. 6.15 (a) and (f)] are consistent with those for a lamellar orientation perpendicular to the substrate but random in the plane of the film (see section 3.4). Therefore we conclude from the combined data of reflectivity and SANS that, a mixed orientation with boundary layers parallel and the central part partially perpendicular to the substrate was observed after the first annealing (AUG04B), and a strong electric field of $E = 47 \text{ V}/\mu\text{m}$ (AUG04H) is able to stabilize the perpendicular orientation formed after the first annealing. Moreover, scattering intensity at q smaller than that for the Bragg reflection was observed from AUG04H, which is attributed to the effects of the electric field. This intensity might indicate the existence of lamellar domains with lateral sizes larger than one lamellar period.

The SANS intensity shown in Figs. 6.13 and 6.15 was detected with an area detector of 128×128 pixels. Using the software GRASP², we are able to integrate the scattering intensity in each pattern over the Bragg peak with respect to q and plot the integrated intensity with respect to the azimuthal angle Ω . If the pixels are numbered from the

²Graphical Reduction and Analysis SANS Program for MatlabTM, downloaded from the website www.ill.fr/lss/grasp.

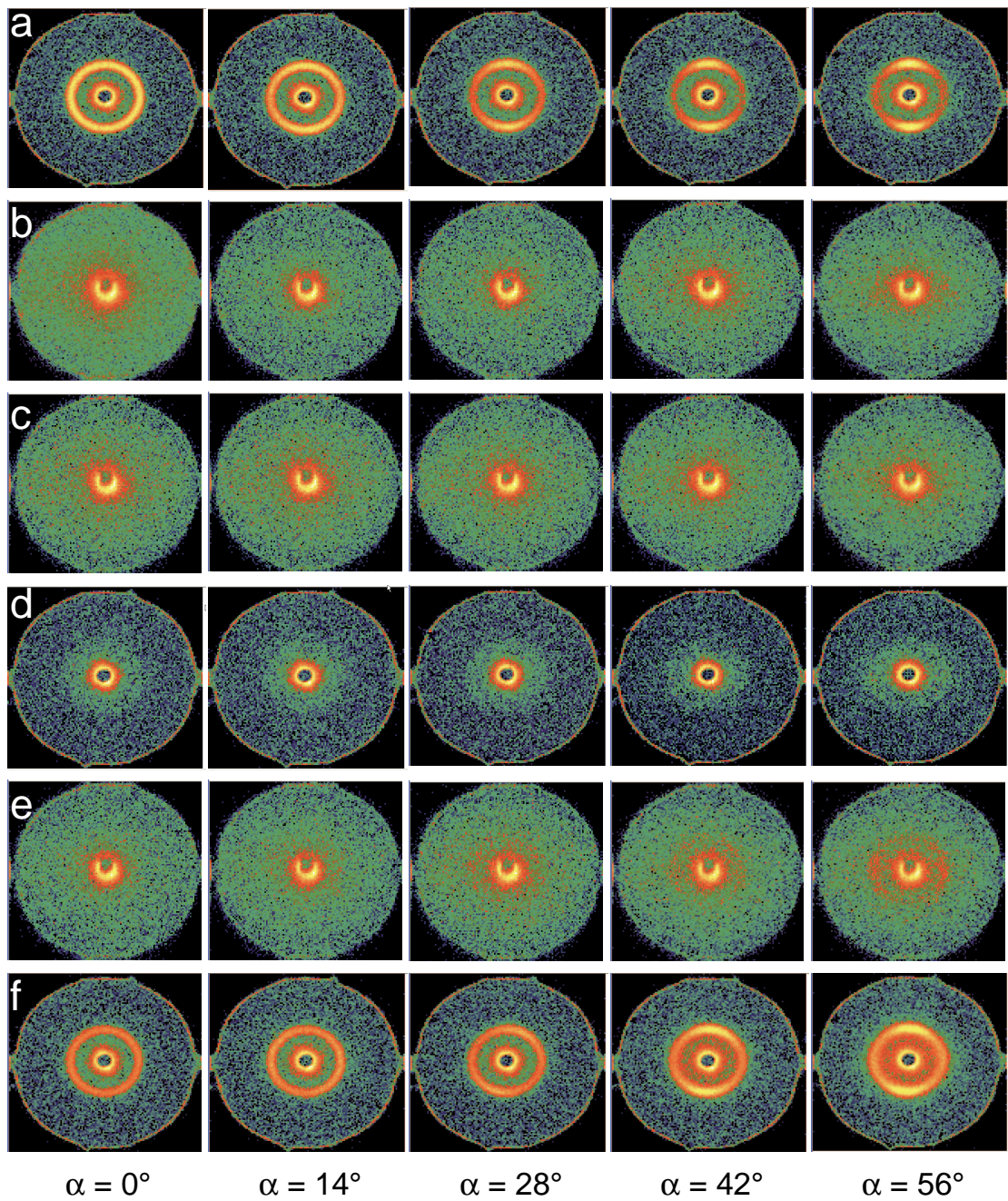


Figure 6.15: SANS patterns measured at different angles of incidence α , obtained from films of $0.86 \mu\text{m}$: (a) AUG04B (1st annealing), (b) NOV05D (2nd annealing, without E), (c) NOV05C ($E = 0.1 \text{ V}/\mu\text{m}$), (d) AUG04C ($E = 1 \text{ V}/\mu\text{m}$), (e) NOV05E ($E = 12 \text{ V}/\mu\text{m}$), and (f) AUG04H ($E = 47 \text{ V}/\mu\text{m}$).

center to the edges (maximum no. 64), the integral was done over a ring from pixel no. 12 to pixel no. 32, while the maximum intensity of the Bragg reflection occurs at about pixel no. 21. Fig. 6.16 (a) shows the azimuthal angular dependence of the Bragg intensity obtained from the sample AUG04B. The scattering intensity is corrected by a factor $\cos \alpha$ due to the difference in the illuminated area. At $\alpha = 0^\circ$, the intensity is isotropic with respect to Ω , corresponding to the homogeneous ring in Fig. 6.15 (a). As α increases, the intensity has maxima at $\Omega = 0^\circ$ and 180° , and the FWHM of the curves becomes smaller, which is consistent with an orientation distribution around the perpendicular orientation. The underlying orientation distribution is assumed to be Gaussian, such as

$$g(\gamma) = \frac{1}{\sqrt{2\pi(\Delta\Omega/2)^2}} \exp \left[\frac{-2(\gamma - \pi/2)^2}{(\Delta\Omega)^2} \right] \quad (6.6)$$

where γ is the inclination angle with respect to the substrate and $\gamma = \pi/2$ corresponds to the perpendicular orientation. The FWHM $\Delta\Omega$ can be obtained by extrapolating the FWHMs of the curves in Fig. 6.16 (a) to $\alpha = 90^\circ$, while the latter are obtained under the help of the two dashed lines. The upper line indicates the maximum intensity (about 2.9) determined by taking the average intensity of the curve measured at $\alpha = 0^\circ$, while the lower one indicates the half-maximum intensity determined from the difference between the maximum intensity and the background intensity. The background intensity (about 0.5) is determined from the lowest intensity shown in the curve measured at $\alpha = 56^\circ$. The FWHMs are then plotted in Fig. 6.16 (c) as a function of $1/\sin \alpha$. A straight line is obtained and extrapolated to $\alpha = 90^\circ$ to give $\Delta\Omega = 16^\circ$. The orientation parameter S defined by [12]

$$S \equiv \frac{3\langle \cos^2 \gamma \rangle - 1}{2} \quad (6.7)$$

with

$$\langle \cos^2 \gamma \rangle = \frac{\int_0^\pi g(\gamma) \cos^2 \gamma d\gamma}{\int_0^\pi g(\gamma) d\gamma} \quad (6.8)$$

can be calculated as -0.48 . For the sample AUG04H, the maximum intensity measured at $\alpha = 42^\circ$ and 56° is higher than that obtained at the smaller angles. This might also be due to the remaining block copolymer on the back of the silicon wafer. In Fig. 6.16 (b), the azimuthal angular dependence is only shown for the measurements at the higher angles. The FWHMs are again obtained under the help of the two dashed lined, with the upper one indicating the maximum intensity (about 3.4) and the lower one indicating the half-maximum intensity (about 2.3). Comparison between the FWHMs obtained from AUG04B and AUG04H [Fig. 6.16 (c)] shows that the orientation distributions in both films are comparable. As will be discussed in section 6.4, while the structure of AUG04B is non-equilibrium, the structure of AUG04H is regarded as the equilibrium state under the strong electric field.

For each SANS pattern measured at $\alpha = 0^\circ$ shown in Fig. 6.13 and Fig. 6.15, the scattering intensity is integrated with respect to the azimuthal angle Ω and plotted in Fig. 6.17 and Fig. 6.18, respectively, as a function of the scattering vector q . The latter two figures present essentially similarities to each other. For both thicknesses, the film prepared by only the first annealing always presents the highest Bragg intensity, and the film prepared with the strongest electric field always presents the next highest Bragg intensity. For the films prepared with electric fields not strong enough, only the background intensity was observed. However, the Bragg intensity is increased by a factor about 20 from the case of thinner films to the case of thicker films. The Bragg

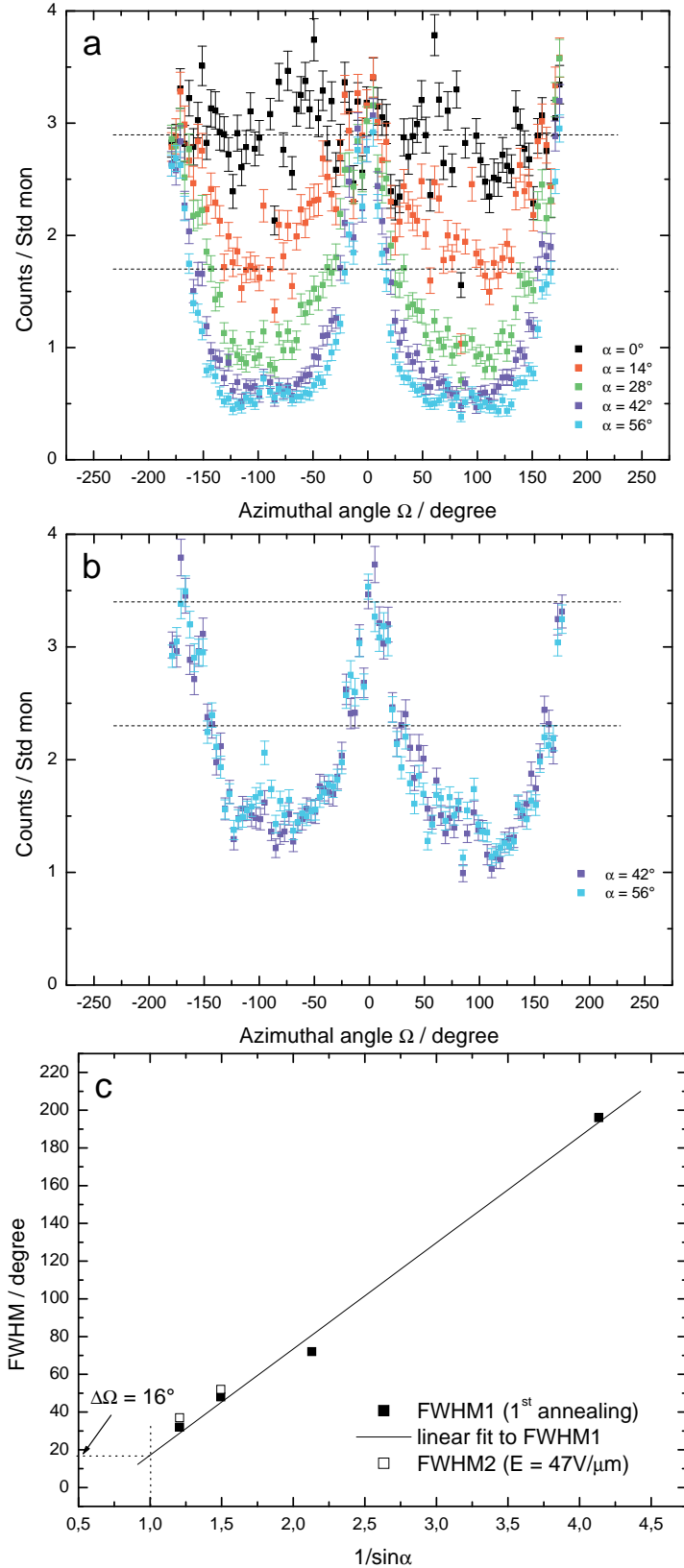


Figure 6.16: Azimuthal angular dependence of the Bragg intensity for the samples (a) AUG04B ($d = 0.86 \mu\text{m}$, 1st annealing) and (b) AUG04H ($d = 0.86 \mu\text{m}$, 2nd annealing, $E = 47 \text{V}/\mu\text{m}$), respectively. The dashed lines are assistant lines. (c) FWHMs obtained from (a) and (b) are plotted as a function of $1/\sin \alpha$.

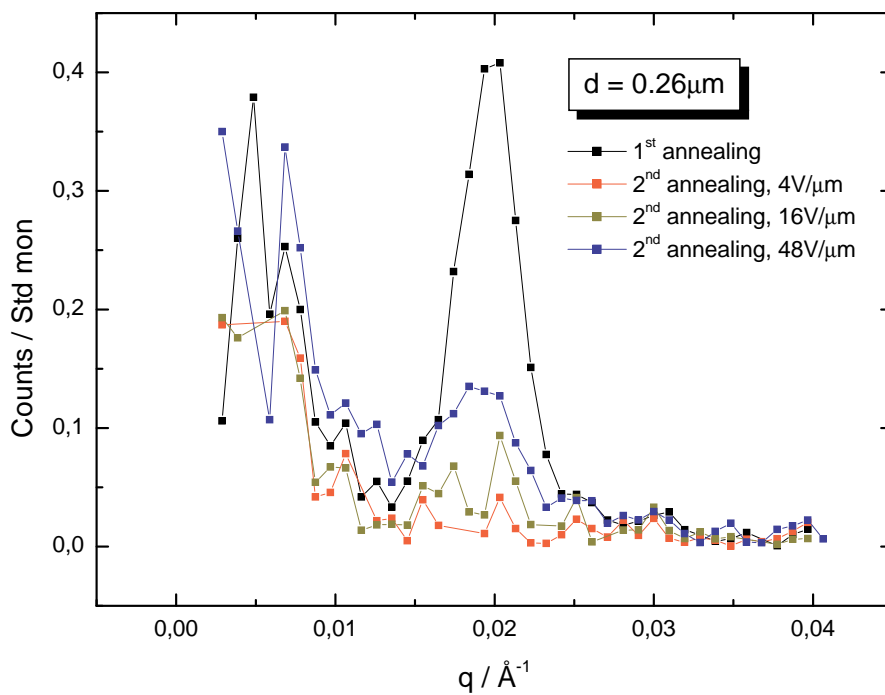


Figure 6.17: SANS intensity measured at $\alpha = 0^\circ$ from the films of $0.26 \mu\text{m}$.

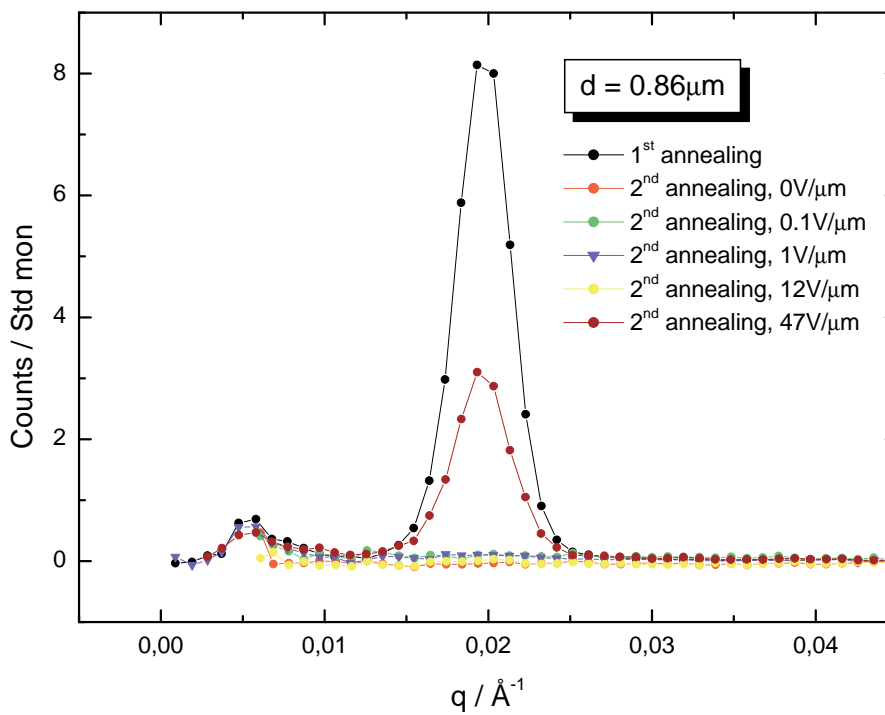


Figure 6.18: SANS intensity measured at $\alpha = 0^\circ$ from the films of $0.86 \mu\text{m}$.

intensity comes from lamellae with a perpendicular orientation in the films, indicating a misalignment of the lamellae. In the thinner films of $0.26 \mu\text{m}$, the structure has been shown by the reflectivity data to be a parallel orientation throughout the film. From the SANS data, it is shown that the degree of misalignment in these films must be very low, but does not vanish. In the thicker films of $0.86 \mu\text{m}$, the degree of misalignment becomes much higher, indicating the effects of surface interactions are not as dominant as in the case of the thinner films and the lamellae in the middle of the films can be more misaligned with respect to the substrate.

6.3 Test measurements on MORPHEUS

In Fig. 6.13 (d) and Fig. 6.15 (e), two equatorial points of Bragg intensity were observed in the SANS patterns measured at $\alpha = 56^\circ$, indicating lamellae aligned at $\gamma \sim 30^\circ$ with respect to the substrate. In order to check the lamellar structures aligned at $\gamma < 30^\circ$, we need to go to higher α s which is not possible in our SANS experiments. On the other hand, diffuse scattering measured at $\omega = (90^\circ - \alpha)$ detects the same structures which will be detected by small-angle scattering measured at α . As will be shown in chapter 7, ω is restricted to about 6° on the reflectometer AMOR because of the vertical working geometry of the instrument. The advantage of using the reflectometer MORPHEUS is that the range of ω can be greatly enlarged compared with that for AMOR. Test measurements on the lamellar structures aligned at $\gamma < 30^\circ$ were performed at the reflectometer MORPHEUS. In the test measurement shown in Fig. 6.19, the scattering angle 2θ was fixed so that the scattering vector was fixed at $q_i = q_{z,i}^*$, where $q_{z,i}^*$ corresponds to the position of the maximum intensity in the first order Bragg peak. Since

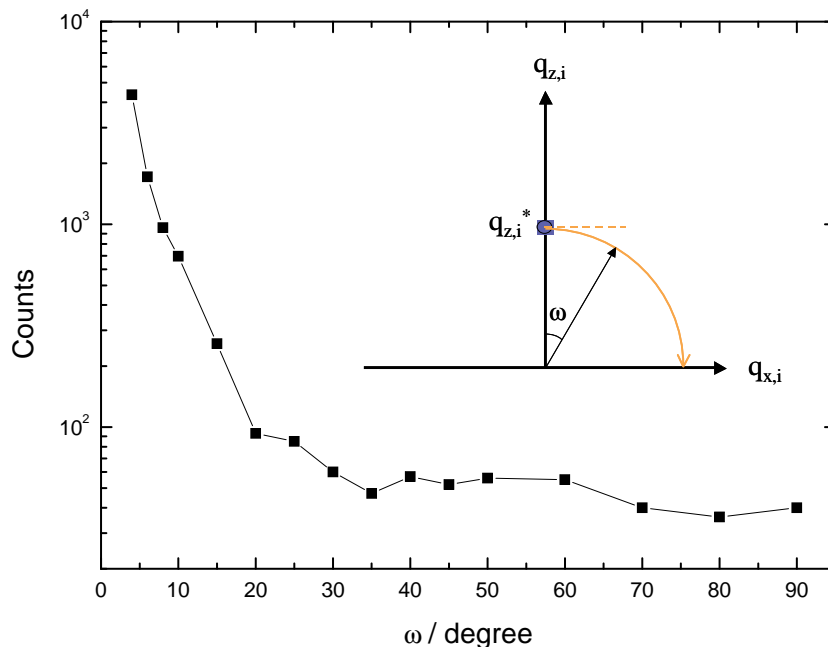


Figure 6.19: Test measurement on the sample NOV05E ($d = 0.86 \mu\text{m}$, $E = 12 \text{ V}/\mu\text{m}$), with the scan (the curve with an arrow) shown in the inset.

the reflectometer works in a monochromatic mode with a selected wavelength 4.74 \AA of the neutron beam, and $q_{z,i}^*$ is determined from the reflectivity data to be 0.02 \AA^{-1} , 2θ

can be calculated as

$$2\theta = 2 \arcsin\left(\frac{q_{z,i}^* \lambda}{4\pi}\right) = 2 \arcsin\left(\frac{0.02 \text{ \AA}^{-1} \cdot 4.74 \text{ \AA}}{4\pi}\right) \approx 0.86^\circ \quad (6.9)$$

The scan of the measurement in reciprocal space is shown in the inset of the figure. In this scan, the incident angle ω was changing from 0° to 90° while keeping the scattering angle $2\theta = 0.86^\circ$. Therefore we measured the scattering intensity along part of the circle with a radius equal to $q_{z,i}^*$. This circle coincides with the Bragg sheet (dashed line) only at very small ω or $q_{x,i}$. But the deviation of $q_{z,i}$ from $q_{z,i}^*$ can be neglected for ω smaller than 30° at which the deviation is only 13%. In this sense, the measuring range of ω was safely extended from originally 6° on AMOR to about 30° on this instrument. Fig. 6.19 shows that the diffuse scattering intensity decreases monotonically with increasing ω (for $\omega < 30^\circ$), indicating no preferred lamellar orientation at $\gamma < 30^\circ$.

6.4 Discussion

From the combined results of reflectivity and SANS, we observed: (i) a completely parallel orientation in the films of $0.26 \mu\text{m}$ even if an electric field as strong as $\sim 40 \text{ V}/\mu\text{m}$ is applied; (ii) a mixed orientation with boundary layers parallel and the central part partially perpendicular to the substrate in the films of $0.86 \mu\text{m}$ after the first annealing; (iii) the mixed orientation becomes unstable under a small compressive stress and will be converted into a completely parallel orientation; and (iv) the mixed orientation is only stabilized by an electric field as strong as $\sim 40 \text{ V}/\mu\text{m}$. In addition, a fully perpendicular orientation was never observed in our experiments, seen from the Bragg peaks indicating the presence of boundary layers parallel to the substrate. In this section, the formation of these film structures and the orientation of the lamellae will be discussed.

6.4.1 Mixed orientation

The experimental results of reflectivity and SANS from the sample AUG04B ($d = 0.86 \text{ V}/\mu\text{m}$, 1st annealing) show that a mixed orientation with boundary layers parallel and the central part partially perpendicular to the substrate was observed in this film. The orientation distribution around the perpendicular orientation is assumed to be Gaussian, and was found very narrow. The full-width at half-maximum of the Gaussian distribution is $\Delta\Omega = 16^\circ$ and the orientation parameter $S = -0.48$. This indicates the lamellae which are not aligned parallel to the substrate are preferentially aligned perpendicular to the substrate. To our knowledge, such a mixed orientation was observed and reported in the previous literature (see figure 1 in ref [64]), and was attributed to the long life-time of the ‘‘T’’-junction defects [65, 66] by the authors.

The mixed orientation inferred from our data is schematically shown in Fig. 6.20 (r. h. s.). This structure is believed to be non-equilibrium, because the surface effects which align the lamellae parallel to the substrate are the only effects in this case (in the absence of electric fields). Therefore the equilibrium structure should be a parallel orientation throughout the film. However, if the film is thick enough, the surface effects become less dominant in the middle of the film where the lamellae can be misaligned with respect to the substrate. Our explanation for the formation of the mixed orientation observed is schematically shown in Fig. 6.20. Imagine a random orientation of the lamellae (l. h. s.) is formed in the early stage of annealing. Defect structures, costing much energy, will be formed at the boundaries between domains with different orientations.

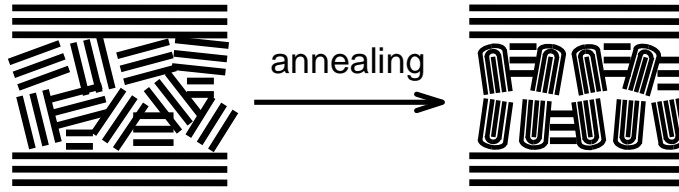


Figure 6.20: Schematic explanation for the formation of the mixed orientation observed after the first annealing.

The defect structures tend to be healed out during annealing to achieve the equilibrium state with the lowest free energy. However, if the energy barrier to heal out these defects is too high to overcome, the non-equilibrium structures can be pinned in the film. From the observation, we conjecture that the energy barrier for defect structures between boundary layers and perpendicularly aligned domains in the middle of the film might be much higher than those for other defects. That is to say, only these defect structures can survive after the long-time annealing, while other defects will be healed out. Consequently, the structure with preferentially parallel and perpendicular orientations (r. h. s.) will be observed after the annealing. It cannot be excluded that the parallel orientation exists in the middle of the film. But we know from the reflectivity data, the portion of this parallel orientation must be small. The total amount of lamellae with parallel orientation, including boundary layers and those in the middle, corresponds to about one fifth of the film thickness. From the comparison between Fig. 6.17 and Fig. 6.18, it can also be seen that the amount of lamellae which are misaligned to the substrate is about twenty times larger in the thicker films than in the thinner films, although the film thickness is only increased by a factor of 3-4.

6.4.2 Parallel orientation

The experimental results of reflectivity and SANS from the sample NOV05D ($d = 0.86 \mu\text{m}$, 2nd annealing with compressive stress only) show that the mixed orientation becomes unstable under the small mechanical stress, and will be converted into a completely parallel orientation (Fig. 6.21). As the completely parallel orientation

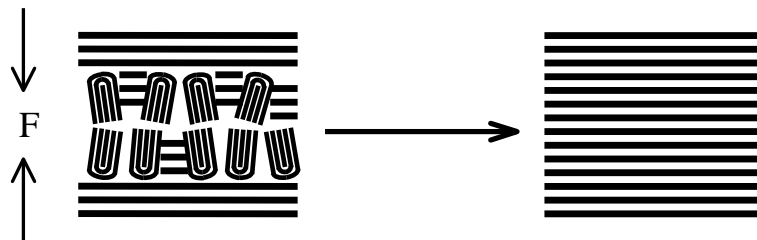


Figure 6.21: Schematic drawing of the structure transformation from a mixed orientation to a parallel orientation under a small vertical compressive stress.

is believed to be equilibrium, it seems that the compressive stress induces an instability in the structure with the mixed orientation and helps the system to reach its equilibrium state. The effect of the compressive stress might be similar to that of a lateral shear [67, 68, 69] which induces parallel orientation of the lamellae. However, here we will propose another explanation for the experimental observation based on the viscoelastic nature of block copolymers.

As shown in Fig. 6.22, the block copolymer molecules reacts in different ways under the compressive stress if they adopt different orientations (perpendicular or parallel). In

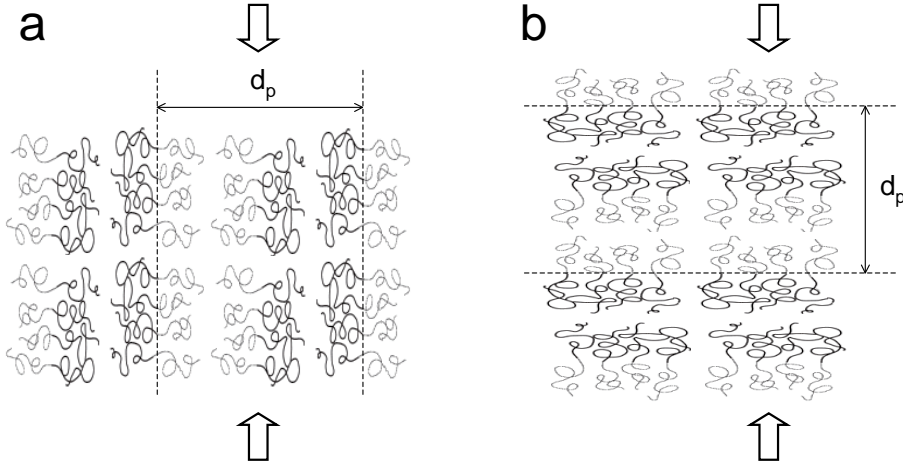


Figure 6.22: Block copolymer molecules under a vertical compressive stress in lamellae oriented (a) perpendicular and (b) parallel to the substrate.

the case of lamellae with the perpendicular orientation, the force is acted perpendicular to the chains and the copolymer may flow like a liquid in lateral dimensions. The flow may induce an instability in the originally meta-stable structure and the system will seek for its equilibrium after this disturbance. In this way the equilibrium state can be achieved. In the case of lamellae with the parallel orientation, the force is acted along the chain direction and the copolymer may deform like an elastic body. An elastic force will be generated to resist the external force because the structure deviates from its equilibrium lamellar period. The modulus of such a structure should be high enough so that the structure is stable under the external force. In the following paragraphs we will try to estimate this modulus near the equilibrium lamellar period of the structure. The result shows that the modulus is indeed high enough to enable the structure to be stable under the external force we have applied. Therefore it supports our explanation for the transformation of structure from a mixed orientation to a completely parallel orientation.

The equilibrium lamellar period in a layered diblock copolymer is determined from the balance between the enthalpic and entropic contributions to the free energy of the system. If d_i denotes the interfacial thickness between the two components A and B, the enthalpically unfavored mixing in the transition layer gives rise to a penalty in the free energy per molecule [55]

$$\Delta G_{p,h} = k_B T \left(2\chi N \frac{d_i}{d_p} \right) \quad (6.10)$$

where χ is the Flory-Huggins interaction parameter, N is the polymerization index, and d_p is the lamellar period which is related to the interfacial area o_p per molecule by

$$o_p d_p = 2Nv_c \quad (6.11)$$

with v_c the volume of the monomer (assumed the same for A- and B- monomers). The entropic contribution to the free energy per molecule can be written as [55]

$$\Delta G_{p,s} = k_B T \left(\frac{R}{R_0} \right)^2 \quad (6.12)$$

where R and R_0 are the end-to-end distance of the copolymer chain in the layers and for the ideal chains, respectively. The total free energy per molecule is obtained from

the sum of eqs. (6.10) and (6.12) as

$$\begin{aligned}\Delta G_p &= \Delta G_{p,h} + \Delta G_{p,s} \\ &= k_B T \left(2\chi N d_i d_p^{-1} + \frac{\beta^2}{4R_0^2} d_p^2 \right)\end{aligned}\quad (6.13)$$

where we used the linear relation $2R = \beta d_p$ with the coefficient β on the order of magnitude 1. The first derivative of free energy with respect to d_p is calculated as

$$\frac{\partial G_p}{\partial d_p} = k_B T \left(-2\chi N d_i d_p^{-2} + \frac{\beta^2}{2R_0^2} d_p \right)\quad (6.14)$$

The equilibrium of d_p can be determined by setting $\partial G_p / \partial d_p = 0$ in eq. (6.14), thus we obtain

$$d_{p,eq} = \sqrt[3]{\frac{4\chi N d_i R_0^2}{\beta^2}}\quad (6.15)$$

The left hand side of eq. (6.14) has dimension of force per molecule, which divided by the area o_p per molecule yields the stress σ_p

$$\sigma_p = \frac{1}{o_p} \frac{\partial G_p}{\partial d_p} = k_B T \left(-\frac{\chi d_i}{v_c} d_p^{-1} + \frac{\beta^2}{4R_0^2 N v_c} d_p^2 \right)\quad (6.16)$$

where we used the compressibility condition eq. (6.11). If d_p in eq. (6.16) is substituted by the strain $\varepsilon_p = d_p / d_{p,eq} - 1$, we obtain

$$\sigma_p = -\frac{k_B T \chi d_i}{v_c d_{p,eq}} (\varepsilon_p + 1)^{-1} + \frac{k_B T \beta^2 d_{p,eq}^2}{4R_0^2 N v_c} (\varepsilon_p + 1)^2\quad (6.17)$$

which is the relation between the stress and the strain.

For our copolymer of P(S-b-MMA), the molecular weight M is 75000 g/mol, the average density ρ of PS and PMMA is 1.12 g/cm³, and the average end-to-end distance R_0 is about 180 Å from table 6.9. The product of χN is estimated as 27 [71], and the

	PMMA	PS	copolymer
ρ (g/cm ³)	1.188 [54]	1.04-1.065 [54]	~ 1.12
R_0^2/M (Å ² mol/g)	0.425 [70]	0.434 [70]	~ 0.43

Table 6.9: Physical properties of the copolymer PS-b-PMMA.

interfacial thickness d_i was reported as 50 Å [62]. The equilibrium $d_{p,eq}$ is obtained from the experiments as 320 Å. Thus the coefficient β can be calculated from eq. (6.15) as

$$\beta = \sqrt{\frac{4\chi N d_i R_0^2}{d_{p,eq}^3}} \approx 2.31\quad (6.18)$$

The volume of the molecule Nv_c is estimated as

$$Nv_c = \frac{M}{\rho N_A} = \frac{75000 \text{ g/mol}}{1.12 \text{ g/cm}^3 \times (6.02 \times 10^{23} / \text{mol})} \approx 1.1 \times 10^5 \text{ Å}^3\quad (6.19)$$

where N_A is the Avogadro's number. The unit of energy $k_B T$ at 500 K is estimated as 6.9×10^{-21} J. Substituting the values of $k_B T$, χN , d_i , Nv_c , $d_{p,eq}$, β and R_0 into eq. (6.17) and using the SI units, we obtain

$$\sigma_p = (2.65 \times 10^5 \text{ Pa}) \cdot \left[-(\varepsilon_p + 1)^{-1} + (\varepsilon_p + 1)^2 \right]\quad (6.20)$$

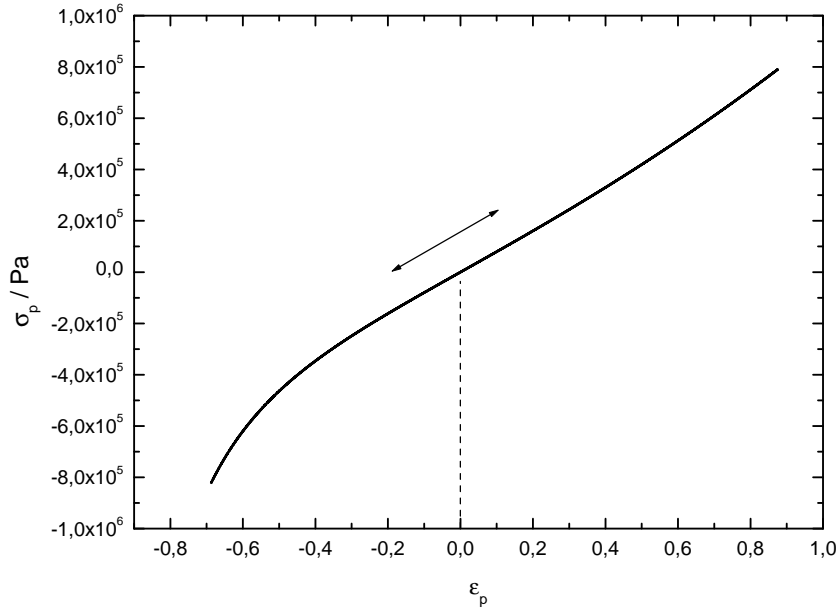


Figure 6.23: Stress-strain curve calculated from eq. (6.20). The curve is rather straight in the vicinity of $\varepsilon_p = 0$, with the slope corresponding to the modulus of the structure.

The stress-strain curve calculated from eq. (6.20) is shown in Fig. 6.23. The curve is not linear in view of the whole range of strain shown here, but rather straight in the vicinity of the equilibrium, i.e., where $\varepsilon_p = 0$. The slope of the curve around $\varepsilon_p = 0$ can be calculated from eq. (6.20) as 7.95×10^5 Pa, which corresponds to the modulus of the structure. From this modulus, the change in d_p under a stress of 1000 Pa is about 0.1%. In section 6.1.5, we mentioned that from the reflectivity data, there seems to be an approximately 4% decrease in d_p after the second annealing with the application of the compressive stress. However, this cannot be attributed to the effect of the stress, because from the calculation we know that the decrease in d_p should be much smaller. Therefore, it is only attributed to a variation within the experimental error.

6.4.3 Alignment by the electric field

The experimental results of reflectivity and SANS from the sample AUG04H ($d = 0.86 \mu\text{m}$, $E = 47 \text{V}/\mu\text{m}$) indicate that the perpendicular orientation in the middle of the film observed after the first annealing is stabilized by the electric field. The sample AUG04H should have a similar structure to that of the sample AUG04B (shown on the r. h. s. of Fig. 6.20), with boundary layers parallel and the central part partially perpendicular to the substrate. Defect structures must be formed at the boundaries between domains with different orientations. While the structure of AUG04B is non-equilibrium, the structure of AUG04H is regarded as the equilibrium state under such a strong electric field. If the structure is equilibrium, the gain in the electrostatic energy ΔF_{el} given in eq. (2.17) must overcome the energy cost ΔF_{def} by the defect structures. The lamellae in this film which are parallel to the substrate are estimated as 10 periods from the fit to the reflectivity data (Fig. 6.12) using Parratt32. Therefore the thickness of the perpendicular part is estimated as 17 (total thickness corresponds to 27) lamellar periods, i.e., $\sim 0.5 \mu\text{m}$. Using $\varepsilon_{PS} = 2.5$, $\varepsilon_{PMMA} = 6$ (at 205°C)³, $E_0 = 47 \text{V}/\mu\text{m}$, and a thickness of $0.5 \mu\text{m}$ for the perpendicular orientation, we estimate ΔF_{el} from eq.

³measured by Peter Kohn, a Ph. D student in our group

(2.17) as

$$\begin{aligned}
\Delta F_{el} &= -\frac{1}{2}\varepsilon_0 \left[\frac{(\varepsilon_A - \varepsilon_B)^2}{2(\varepsilon_A + \varepsilon_B)} \right] E_0^2 d_{\perp} \\
&= -\frac{1}{2} \cdot \left(\frac{8.8542 \times 10^{-12} \text{ C}^2}{\text{J} \cdot \text{m}} \right) \cdot \left[\frac{(6 - 2.5)^2}{2 \cdot (6 + 2.5)} \right] \cdot \left(\frac{47^2 \text{ V}^2}{\mu\text{m}^2} \right) \cdot 0.5 \mu\text{m} \\
&\approx -3.5 \times 10^{-3} \text{ J/m}^2
\end{aligned} \tag{6.21}$$

The energy cost ΔF_{def} by the defect structures is therefore estimated as $3.5 \times 10^{-3} \text{ J/m}^2$.

6.4.4 Effect of the film thickness

The film thickness was found to play a non-trivial role in determining the structure of the films. Here we examined films of thicknesses $0.26 \mu\text{m}$ and $0.86 \mu\text{m}$, in the absence or in the presence of an electric field.

In the absence of an electric field, a complete alignment by the surface effects was only achieved in the thinner films of $0.26 \mu\text{m}$, indicating the surface effects are dominant in these films. In the thicker films of $0.86 \mu\text{m}$, the surface effects become less dominant in the middle of the film, and only the boundary layers are able to be aligned by the surface effects.

In the presence of an electric field, the final structure of the film is determined by the competing effects of surface interactions and the electric field. The effects of the electric fields in films of different thicknesses were found different, but similar in a deeper sense. The difference is, the field was never able to induce a perpendicular orientation in the thinner films, even if the field strength is about $40 \text{ V}/\mu\text{m}$, while such a field was found able to stabilize the perpendicular orientation in the middle of the thicker films. The similarities can be seen from the SANS data. For example, the two equatorial points of Bragg intensity observed in Fig. 6.13 (d) were observed in Fig. 6.15 (e) again. This indicates that a weaker field of $12 \text{ V}/\mu\text{m}$ has similar effects on the thicker films to those of a stronger field of $48 \text{ V}/\mu\text{m}$ on the thinner films. The similarity between Fig. 6.17 and Fig. 6.18 also indicates that the effect of the electric field varies in a similar way with the strength of the field in films of different thicknesses.

Chapter 7

Diffuse scattering

As mentioned in chapter 3, the reflectivity provides us information about the variation in the scattering length density $\rho(z)$ (normal to the film surface), while the diffuse scattering intensity gives information about the scattering length density inhomogeneity in the lateral directions. In our experiments, the diffuse scattering was measured at a fixed scattering angle $2\theta = 1^\circ$, with the incident angle ω varying from 0.55° to 6.0° , corresponding a $q_{x,i}$ -range from $2 \times 10^{-5} \text{ \AA}^{-1}$ to $2 \times 10^{-3} \text{ \AA}^{-1}$. Here $q_{x,i}$ is the x -component of the internal scattering vector (see section 5.1.6). The details of our sample preparation have been described in chapter 4. Part of the samples are shown in table 6.1. Here we give a complete sample list in table 7.1, and the names of the samples will be referred to in this chapter. In this chapter, the results of the diffuse scattering experiments on these samples will be shown and discussed. A mosaic structure or a structure with fluctuating undulations was observed in the absence of an electric field. The electric field induces an increase in the mosaicity or the fluctuating undulations of the structure, indicated by an increase in the diffuse scattering intensity. From the diffuse scattering data in the $q_{x,i}$ -range we have measured, there seems an indication of the electric-field-induced structural undulations predicted by the Onuki's theory, but the $q_{x,i}$ -range is not large enough to make a clear statement upon this point.

7.1 Mosaicity and thermal fluctuations

In chapter 6, it has been shown that a parallel orientation throughout the film can be achieved in the films with no electric field applied. These are either the thinner films of $0.26 \mu\text{m}$ after the first annealing, or the thicker films of $0.86 \mu\text{m}$ annealed with the compressive stress. The diffuse scattering intensity from such films is shown in Fig 7.1. The scattering angle was fixed at $2\theta = 1^\circ$. The red curve corresponds to the specular scan at $\omega = (2\theta)/2 = 0.5^\circ$. The other curves correspond to longitudinal diffuse scans at $\omega = 0.55^\circ, 0.6^\circ, 0.65^\circ, 0.7^\circ, 1.4^\circ, 1.6^\circ, 1.8^\circ, 2.2^\circ, 2.8^\circ, 3.4^\circ, 4.0^\circ$, and 6.0° , respectively. Even in these films with a completely parallel orientation, considerable diffuse scattering intensity was observed within 6° off from the specular position, showing that the lamellar interfaces are not perfectly flat. This indicates that either a mosaic structure or a structure with fluctuating undulations (or both) exists in the films. Fig. 7.2 shows schematically these different structures with all of them having a parallel orientation of the lamellae. In Fig. 7.2 (a), a structure with perfectly flat interfaces is shown, which was not observed in our experiments. In Fig. 7.2 (b) and (c), a mosaic structure and a structure with fluctuating undulations are shown. The difference between (b) and (c) is that a mosaic structure is relatively static while the fluctuating undulations

sample	$d/\mu\text{m}$	1 st annealing	2 nd annealing
JUN04E	0.86	yes	yes, $E = 2 \text{ V}/\mu\text{m}$
JUN04F	0.86	yes	no
JUN04G	0.86	yes	yes, $E = 4 \text{ V}/\mu\text{m}$
JUN04H	0.26	yes	no
AUG04A	0.86	yes	yes, $E = 0.5 \text{ V}/\mu\text{m}$
AUG04B	0.86	yes	no
AUG04C	0.86	yes	yes, $E = 1 \text{ V}/\mu\text{m}$
AUG04D	0.86	yes	yes, $E = 4 \text{ V}/\mu\text{m}$
AUG04E	0.86	yes	yes, $E = 8 \text{ V}/\mu\text{m}$
AUG04F	0.86	yes	yes, $E = 16 \text{ V}/\mu\text{m}$
AUG04G	0.86	yes	yes, $E = 32 \text{ V}/\mu\text{m}$
AUG04H	0.86	yes	yes, $E = 47 \text{ V}/\mu\text{m}$
NOV04A	0.26	yes	no
NOV04C	0.26	yes	yes, $E = 4 \text{ V}/\mu\text{m}$
NOV04D	0.26	yes	yes, $E = 16 \text{ V}/\mu\text{m}$
NOV04E	0.26	yes	yes, $E = 48 \text{ V}/\mu\text{m}$
AUG05B	0.26	yes	yes, $E = 2 \text{ V}/\mu\text{m}$
AUG05C	0.26	yes	yes, $E = 8 \text{ V}/\mu\text{m}$
AUG05D	0.26	yes	yes, $E = 12 \text{ V}/\mu\text{m}$
AUG05E	0.86	yes	yes, $E = 0.25 \text{ V}/\mu\text{m}$
AUG05F	0.86	yes	yes, $E = 0.5 \text{ V}/\mu\text{m}$
AUG05H	0.86	yes	yes, $E = 0.75 \text{ V}/\mu\text{m}$
AUG05I	0.86	yes	yes, $E = 2 \text{ V}/\mu\text{m}$
NOV05A	0.86	yes	yes, $E = 0.01 \text{ V}/\mu\text{m}$
NOV05C	0.86	yes	yes, $E = 0.1 \text{ V}/\mu\text{m}$
NOV05D	0.86	yes	yes, without E
NOV05E	0.86	yes	yes, $E = 12 \text{ V}/\mu\text{m}$
NOV05F	0.86	yes	yes, $E = 1 \text{ V}/\mu\text{m}$ (AC field)

Table 7.1: List of samples, where d is the film thickness and E is the strength of the applied electric field.

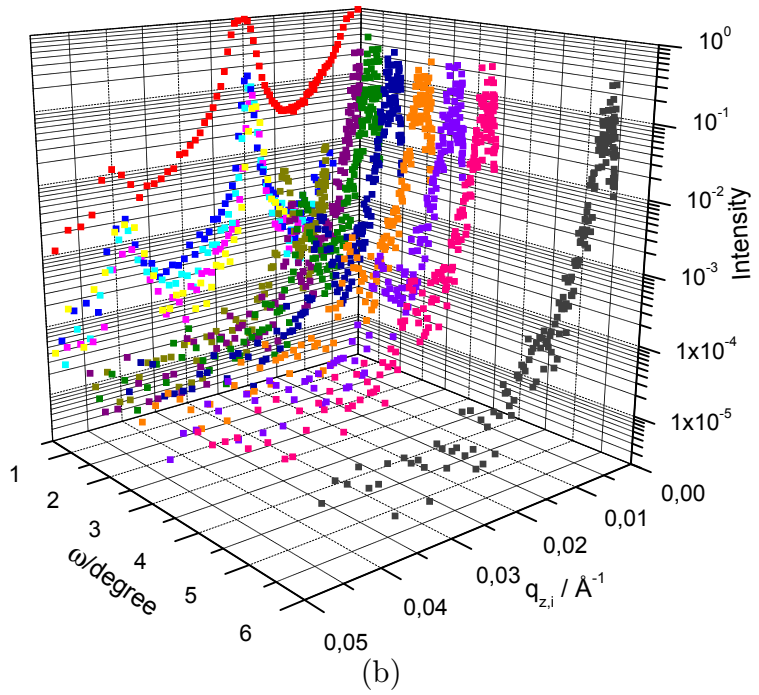
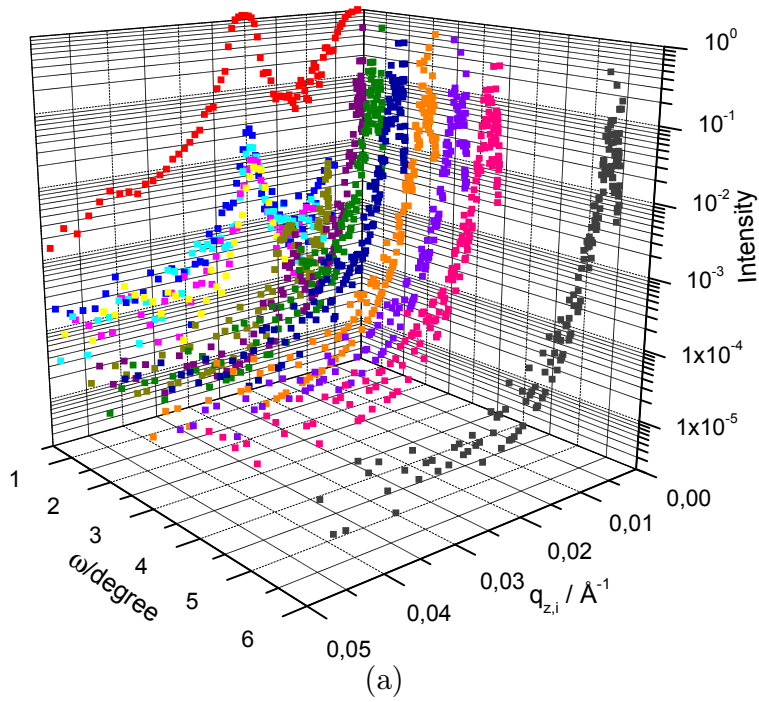


Figure 7.1: Reflectivity and diffuse scattering intensity measured at a fixed scattering angle $2\theta = 1^\circ$ from the samples without an electric field: (a) NOV04A ($d = 0.26 \mu\text{m}$), and (b) NOV05D ($d = 0.86 \mu\text{m}$).

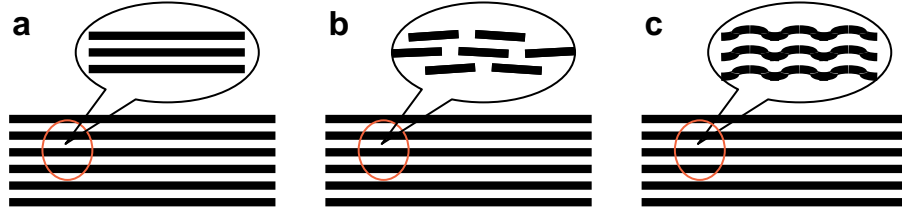


Figure 7.2: Schematic drawings of different structures with a parallel orientation: (a) a structure with perfectly flat interfaces, (b) a mosaic structure which is relatively static, and (c) a structure with fluctuating undulations which are relatively kinetic.

are regarded as kinetic phenomena. These fluctuating undulations are similar to the electric-field-induced structural undulations predicted by the Onuki's theory, but they are most likely induced thermally since there was no electric field applied. From the diffuse scattering experiments we cannot distinguish structures (b) and (c).

An electric field will induce an increase in the mosaicity or the fluctuating undulations. As shown in Fig. 7.3, two films of $0.26 \mu\text{m}$ and $0.86 \mu\text{m}$ respectively, both with a completely parallel orientation (known from reflectivity and SANS), show an increased diffuse scattering intensity compared with the films of the corresponding thicknesses shown in Fig. 7.1. This effect becomes more clear in Fig. 7.4 where the diffuse scattering intensity is plotted as a function of $q_{x,i}$. The diffuse scattering intensity as a function of $q_{x,i}$ is obtained as follows. From section 3.3.5, we know that the measured scattering intensity measured is integrated over the y direction due to the slit geometry we have used, thus a function of $q_{z,i}$ and $q_{x,i}$ (ω can be converted into $q_{x,i}$). The scattering intensity is then integrated over the first order Bragg peak with respect to $q_{z,i}$ and becomes a function of $q_{x,i}$. Here the integral is taken from $q_{z,i} = 0.014 \text{ \AA}^{-1}$ to 0.040 \AA^{-1} . It should be mentioned that the integral range is relatively large because it includes part of the second order Bragg peak. The range was taken in order to make sure that all the intensity from the first order peak is integrated, and since the second order peak is much weaker than the first one, the integral is not significantly affected by making the range slightly smaller. In Fig. 7.4, each curve is obtained from a three-dimensional plot as shown in Fig. 7.1 or 7.3. Here $q_{x,i}$ is calculated from

$$q_{x,i} = q_{z,i}^* \tan\left[\omega - \frac{(2\theta)}{2}\right] \quad (7.1)$$

where $q_{z,i}^*$ indicates the position of the maximum intensity in the first order Bragg peak and is experimentally determined as 0.02 \AA^{-1} , and 2θ is fixed at 1° . For both film thicknesses, the diffuse scattering intensity increases after the application of an electric field. (There is only one exception, i.e., the sample NOV04C with $d = 0.26 \mu\text{m}$ and $E = 4 \text{ V}/\mu\text{m}$.) The increase in the diffuse scattering intensity induced by the electric field is confirmed by a second sample (for each film thickness) prepared by only the first annealing which shows also a lower intensity than the others with an electric field. In the case of the thinner films of $0.26 \mu\text{m}$, the combined results of reflectivity and SANS show that all the lamellae are aligned parallel to the substrate, therefore the increase in the diffuse scattering intensity cannot be attributed to the increase in the number of layers which are parallel to the substrate. This indicates, instead, an increase in the mosaicity or the thermal fluctuations of the structure. This increase might be induced by the torque exerted by the electric field. In the case of the thicker films of $0.86 \mu\text{m}$, there are two contributions to the increase in the diffuse scattering intensity after the second annealing with an electric field. One is the increase in the number of layers

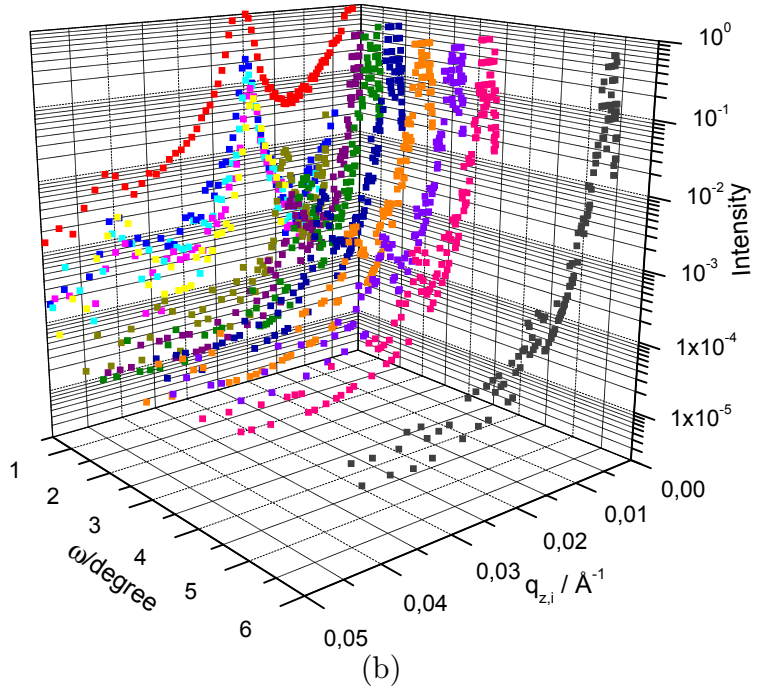
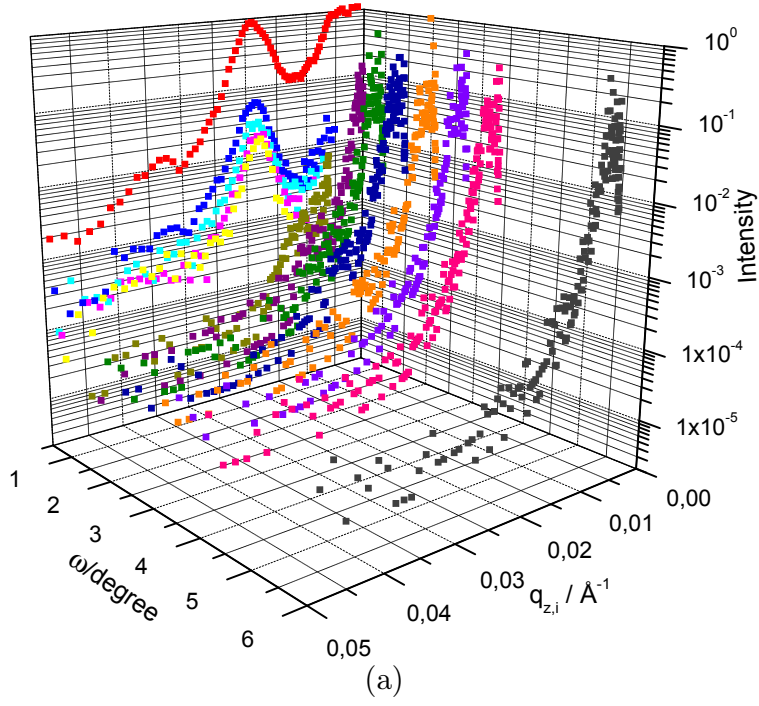


Figure 7.3: Reflectivity and diffuse scattering intensity measured at a fixed scattering angle $2\theta = 1^\circ$ from the samples with an electric field: (a) NOV04E ($d = 0.26 \mu\text{m}$, $E = 48 \text{ V}/\mu\text{m}$), and (b) AUG04C ($d = 0.86 \mu\text{m}$, $E = 1 \text{ V}/\mu\text{m}$).

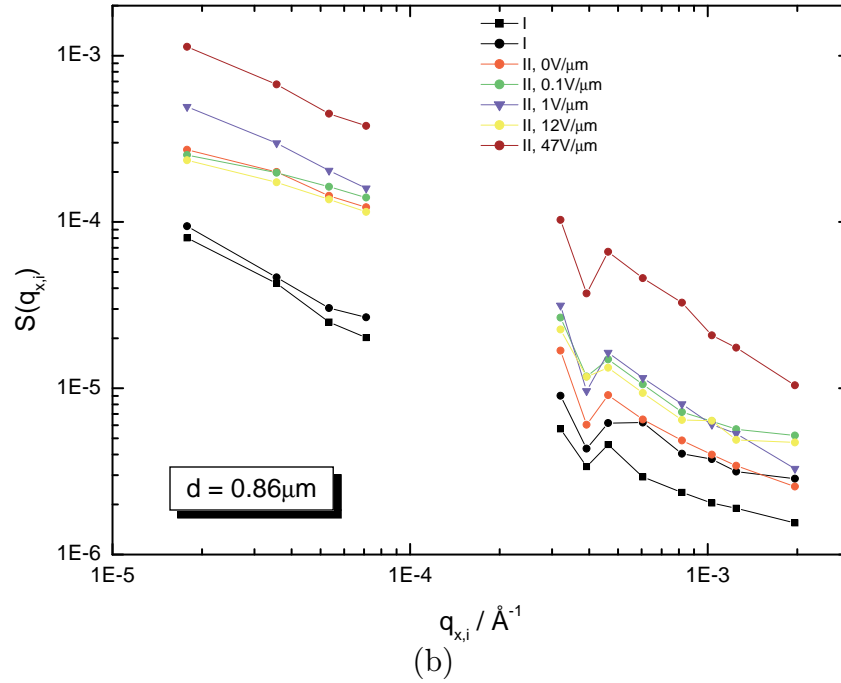
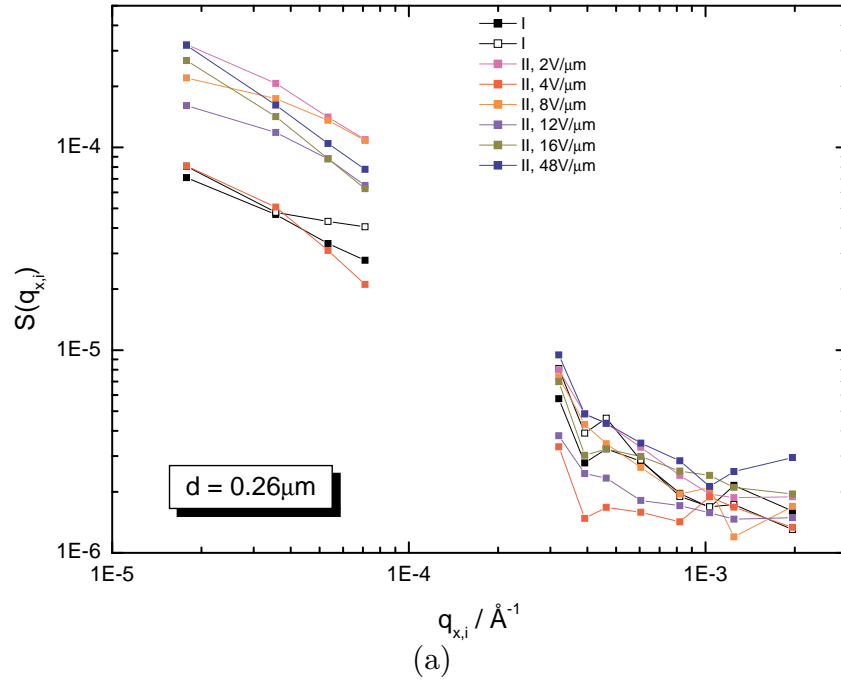


Figure 7.4: Diffuse scattering intensity $S(q_{x,i})$ as a function of $q_{x,i}$. (a) shows the results from the films of $0.26 \mu\text{m}$, NOV04A, JUN04H, AUG05B, NOV04C, AUG05C, AUG05D, NOV04D and NOV04E, respectively. (b) shows the results from the films of $0.86 \mu\text{m}$, JUN04F, AUG04B, NOV05D, NOV05C, AUG04C, NOV05E and AUG04H, respectively. “I” denotes the first annealing, and “II” denotes the second annealing.

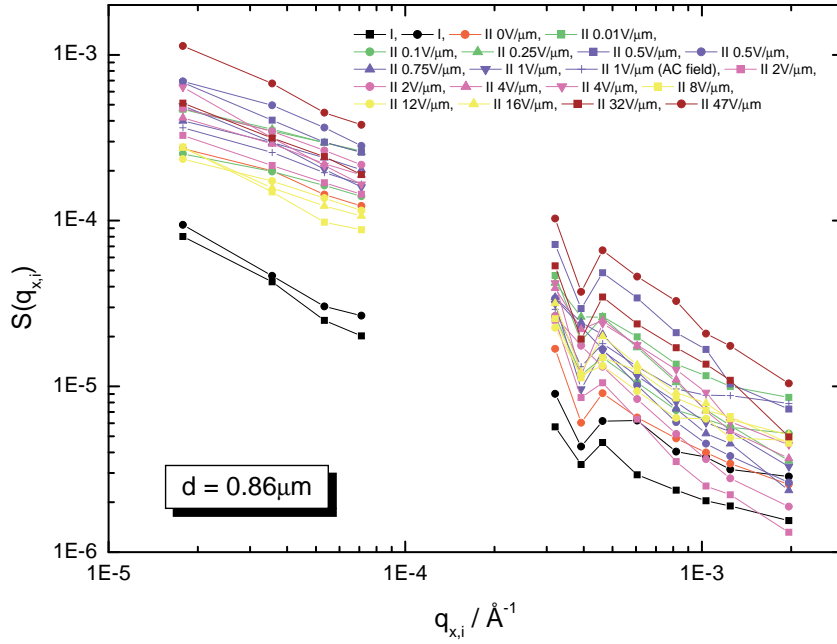


Figure 7.5: Complete data sets of the scattering intensity $S(q_{x,i})$ as a function of $q_{x,i}$, obtained from the films of $0.86 \mu\text{m}$, JUN04F, AUG04B, NOV05D, NOV05A, NOV05C, AUG05E, AUG04A, AUG05F, AUG05H, AUG04C, NOV05F, JUN04E, AUG05I, JUN04G, AUG04D, AUG04E, NOV05E, AUG04F, AUG04G and AUG04H, respectively. “I” denotes the first annealing, and “II” denotes the second annealing.

which are parallel to the substrate, and the other is the effects of the electric field. Known from the combined results of reflectivity and SANS, a mixed orientation with only boundary layers parallel to the substrate is achieved after the first annealing, and the mixed orientation is converted into a completely parallel orientation after the second annealing with the application of a small compressive stress of about 1000 Pa. Therefore the increase in the diffuse scattering intensity from the sample AUG04B (or JUN04F) to the sample NOV05D is due to the first contribution. Comparing the diffuse scattering intensity obtained from NOV05D with that from the samples annealed under an electric field, we observed an increase in the intensity which is attributed to the effects of the electric field. Similar to the case of the thinner films, this indicates an increase in the mosaicity or the thermal fluctuations of the structure induced by the electric field. In Fig. 7.5, complete data sets of the diffuse scattering intensity obtained from the thicker films are shown. These data confirm our discussion above. It is interesting to mention that one sample annealed under an AC (alternative current) field was checked and gives similar results to those obtained from the other films annealed under a DC (direct current) field. This is the sample NOV05F, with an AC field $E = 1 \text{ V}/\mu\text{m}$ having a rectangular shape with a frequency of 80 kHz generated by a TG230 2MHz SWEEP/FUNCTION generator. As we know the electrostatic energy is proportional to the square of the field strength E^2 , an AC field or a DC field should not make a difference in the electric field effects on the lamellar orientation we studied here.

7.2 Correlation length and power law exponent

In section 3.3.5, the method to analyze the diffuse scattering intensity obtained with the slit geometry used in our experiments has been shown. In this section, we will use

the method described and show the experimental results of this analysis.

At small q_ρ , the diffuse scattering function is assumed to follow the Guinier's law as given in eq. (3.73). Integrating the scattering intensity over the y direction by the slit yields the scattering function as a function of q_x given by eq. (3.80). Taking the logarithm of $S(q_x)$ we obtain

$$\log S(q_x) = \log\left(\frac{\sqrt{\pi}I_0}{\xi}\right) - \frac{\xi^2}{2.303}q_x^2 \quad (7.2)$$

showing that the correlation length ξ and the extrapolated intensity I_0 to $q_x = 0$ can be obtained from the slope and the intercept of the linear fit of the plot of $\log S(q_x)$ versus q_x^2 . In Fig. 7.6 (a), such plots of $\log S(q_{x,i})$ versus $q_{x,i}^2$ at small $q_{x,i}$ are shown. As can be seen, the data do not follow a linear relation very well. In each curve, the intensity at the first point (smallest $q_{x,i}$) is too high for a linear relation, which we attribute to the intensity tail from the reflectivity. The intensity of the fourth point (largest $q_{x,i}$) is also too high for a linear relation, which we attribute to the influence of the Yoneda's wings [72]. Therefore the linear fits are only taken for the two middle points in each curve. The correlation lengths and the extrapolated intensity obtained for these samples are shown in table 7.2. The correlation length is in the range from 1

sample	$d/\mu\text{m}$	E [V/ μm]	$\xi/\mu\text{m}$	I_0
NOV04A	0.26	0 (1 st ann.)	1.44	0.50
AUG05B	0.26	2	1.55	2.45
NOV04C	0.26	4	1.76	0.75
AUG05C	0.26	8	1.24	1.49
AUG05D	0.26	12	1.38	1.17
NOV04D	0.26	16	1.74	2.04
NOV04E	0.26	48	1.81	2.34

Table 7.2: Correlation length ξ and extrapolated intensity I_0 obtained by fitting the data to eq. (7.2).

to $2\mu\text{m}$ with or without an electric field, and does not depend on the strength of the electric field systematically. The extrapolated scattering intensity increases after the application of electric fields (with the exception of NOV04C), but does not depend on the strength of the electric field systematically.

At large q_ρ , the diffuse scattering intensity is assumed to obey a power law given by eq. (3.83). The power law exponent is given by the Caillé's theory which predicts [38]

$$S(q_x, 0, q_z^*) \sim q_x^{-(4-2\eta)} \quad (7.3)$$

with

$$\eta = \frac{k_B T (q_z^*)^2}{8\pi\sqrt{BK}} \quad (7.4)$$

where B and K are the layer compressibility and the elastic splay constant of the material, respectively, and q_z^* corresponds to the position of the maximum intensity in the first order Bragg peak. Another prediction by the Caillé' theory is

$$S(0, 0, q_z) \sim (q_z - q_z^*)^{-(2-\eta)} \quad (7.5)$$

which is related to the normal scattering vector q_z . The typical value of K for block copolymers is given in ref [73] as $\sim 10^{-6}$ dyn (or 10^{-11} N). Using $B = 4(q_z^*)^2 K$ [74], we

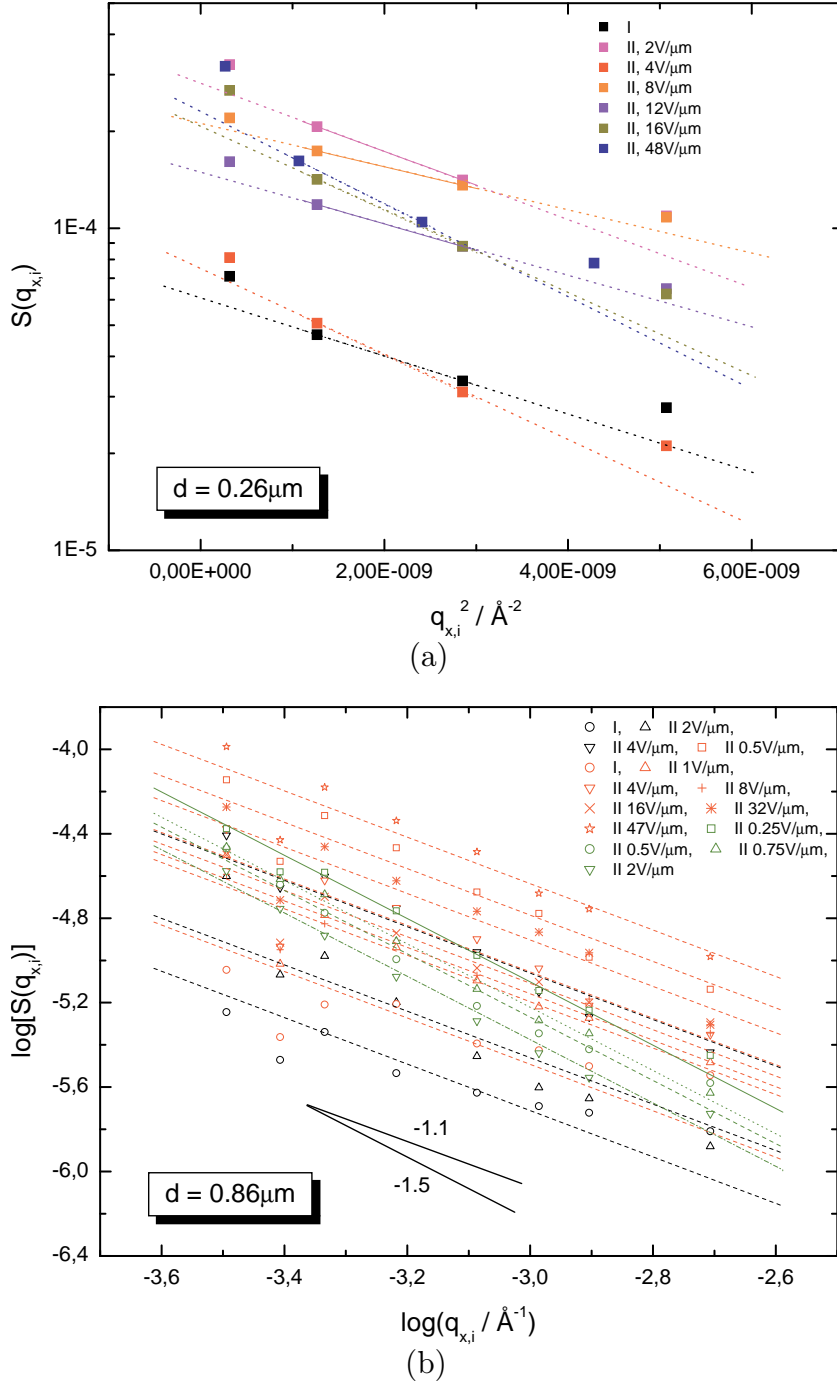


Figure 7.6: (a) Plots of $\log S(q_{x,i})$ versus $q_{x,i}^2$ at small $q_{x,i}$, obtained from the films of $0.26 \mu\text{m}$, NOV04A, JUN04H, AUG05B, NOV04C, AUG05C, AUG05D, NOV04D and NOV04E, respectively. Here small $q_{x,i}$ refers to $q_{x,i} < 10^{-4} \text{ \AA}^{-1}$. The dashed lines are the linear fits to eq. (7.2). (b) Plots of $\log S(q_{x,i})$ versus $\log q_{x,i}$ at large $q_{x,i}$, obtained from the films of $0.86 \mu\text{m}$, JUN04F, JUN04E, JUN04G, AUG04A, AUG04B, AUG04C, AUG04D, AUG04E, AUG04F, AUG04G, AUG04H, AUG05E, AUG05F, AUG05H and AUG05I, respectively. Here large $q_{x,i}$ refers to $q_{x,i} > 10^{-4} \text{ \AA}^{-1}$. The data obey a power law with an exponent about 1.1-1.5. “I” denotes the first annealing, and “II” denotes the second annealing.

can rewrite eq. (7.4) as

$$\eta = \frac{k_B T q_z^*}{16\pi K} \quad (7.6)$$

The value of η at 500 K is estimated as

$$\eta = \frac{(1.38 \times 10^{-23} \text{ JK}^{-1}) \cdot 500 \text{ K} \cdot (0.02 \times 10^{10} \text{ m}^{-1})}{16\pi \cdot (10^{-11} \text{ N})} \approx 0.0027 \quad (7.7)$$

The plots of $\log S(q_{x,i})$ versus $\log q_{x,i}$ at large $q_{x,i}$ obtained from our experiments are shown in Fig. 7.6 (b). The power law exponent obtained from the linear fits of these plots is about 1.1-1.5. The effect of the slit which integrates the scattering intensity over the y direction is to decrease the exponent by 1. Therefore the exponent corresponding to the exponent $(4 - 2\eta)$ in eq. (7.3) is obtained from our experiments as about 2.1-2.5. η is then calculated as ~ 1 , which is not in agreement with the value obtained from eq. (7.7), indicating a discrepancy between the Caillé' theory and the result of our experiments. It should be mentioned that other authors [74, 75, 76] also reported discrepancies between the calculated and observed values of the Caillé exponent in their systems of block copolymers or lipid membranes.

7.3 Structural undulations

In section 2.4, the theory by Onuki has been shown which predicts structural undulations induced by electric fields at soft, deformable lamellar interfaces in block copolymers. From Fig. 7.4, no peak intensity at a finite q_\perp given by eq. (2.31) corresponding to such structural undulations was observed. However, although we have corrected the over-illumination effect [Fig. 5.6] at $\omega < 1^\circ$, we did not consider the effect of different illuminated areas at different ω s. If the area of the cross section of the incident neutron beam is A_0 , the illuminated area A of the sample measured at ω will be

$$A = \frac{A_0}{\sin \omega} \quad (7.8)$$

indicating that the measured scattering intensity has to be corrected by a factor $\sin \omega$. The diffuse scattering intensity $S(q_{x,i})$ after the correction by a factor $\sin \omega$ (Fig. 7.7) shows that $S(q_{x,i})$ seems to be increasing with $q_{x,i}$ for $q_{x,i} > 4 \times 10^{-4} \text{ \AA}$.

Now let us estimate the length scale of the electric-field-induced structural undulations (see Fig. 2.10) if such undulations exist in our system. The Flory-Huggins interaction parameter χ between polystyrene and polymethylmethacrylate blocks were measured by Russell et al. [71], and the experiments yielded a formula $\chi = (0.028 \pm 0.002) + (3.9 \pm 0.06)/T$ with T the absolute temperature. For our samples prepared at $T = 473 \text{ K}$, χ is estimated as 0.036, and the product of χN is estimated as 27 using a polymerization index $N = 750$. This value indicates our system is not exactly in the weak segregation limit. However, here we will estimate q_\perp given by eq. (2.31) in the weak segregation limit. In the weak segregation limit, the natural length scale λ_1 defined by eq. (2.27) is given by [6]

$$\lambda_1 = \frac{d_p}{4\pi} \quad (7.9)$$

where d_p is the lamellar period of the structure. Substituting eq. (7.9) into eq. (2.31), we obtain the lateral scattering vector for the undulations

$$q_\perp = \sqrt{\frac{\pi}{d\lambda_1}} = \frac{2\pi}{\sqrt{d \cdot d_p}} \quad (7.10)$$

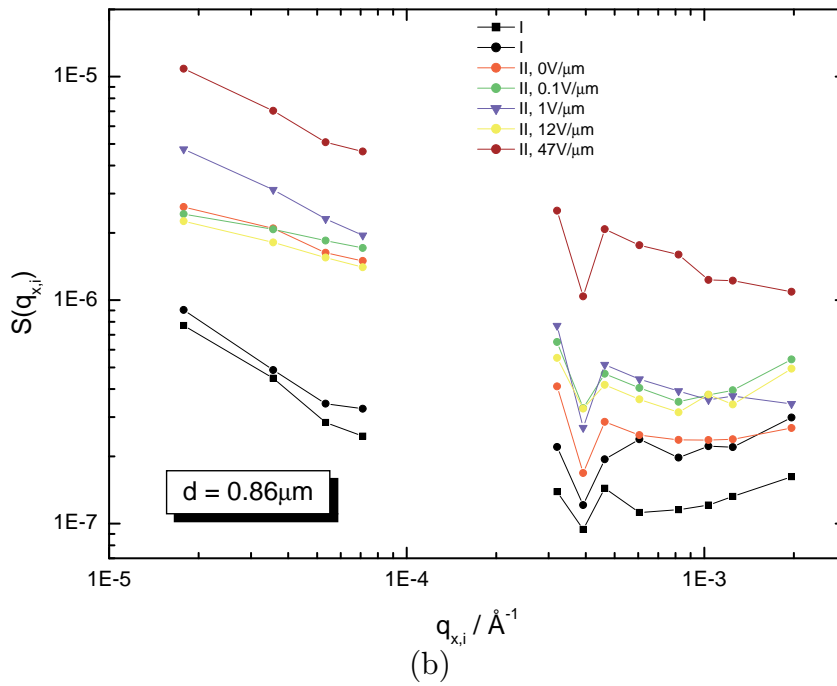
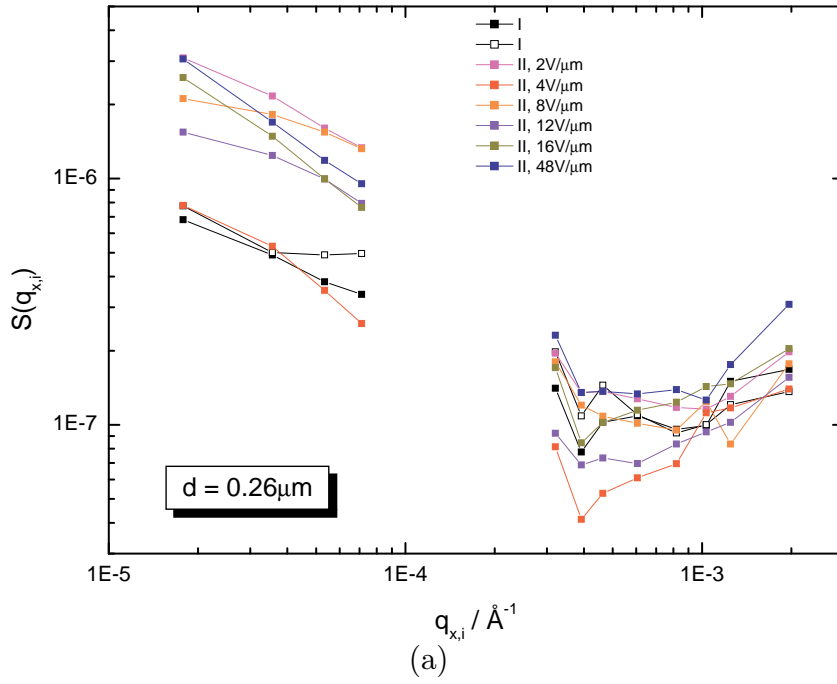


Figure 7.7: Diffuse scattering intensity $S(q_{x,i})$ as a function of $q_{x,i}$, after the correction by a factor $\sin\omega$. (a) shows the results from the films of $0.26\ \mu\text{m}$, NOV04A, JUN04H, AUG05B, NOV04C, AUG05C, AUG05D, NOV04D and NOV04E, respectively. (b) shows the results from the films of $0.86\ \mu\text{m}$, JUN04F, AUG04B, NOV05D, NOV05C, AUG04C, NOV05E and AUG04H, respectively. “I” denotes the first annealing, and “II” denotes the second annealing.

The lamellar period d_p is obtained from the experiments to be 320 \AA . For the block copolymer films of thicknesses $d = 8.5d_p$ and $d = 27.5d_p$, respectively, q_{\perp} is estimated as

$$d = 8.5d_p, \quad q_{\perp} \approx 0.0067 \text{ \AA}^{-1} \quad (7.11)$$

$$d = 27.5d_p, \quad q_{\perp} \approx 0.0037 \text{ \AA}^{-1} \quad (7.12)$$

which is in the right range where the diffuse scattering intensity in Fig. 7.7 shows an increase. The observation of this increase in intensity might be an indication of the electric-field-induced structural undulations with a length scale of about $1/q_{\perp} \sim 0.1 \mu\text{m}$. However, the maximum angle of incidence ω is restricted to about 6° in the experiments and the $q_{x,i}$ -range we have measured is too small (or the films are not thick enough) to make a clear statement on this point.

Chapter 8

Conclusion

In this thesis, we investigated the lamellar orientation in thin films of a symmetric diblock copolymer P(S-b-MMA), under competing effects of surface interactions and an electric field applied perpendicular to the film substrate. The films were annealed after spin-coating in order to induce a completely parallel orientation by the surface effects, although it turned out this is only achieved if the films are thin enough. A second annealing with the application of an electric field was then performed on these films after the first annealing. During the second annealing, an upper electrode was attached to the film surface, while it was found the upper electrode has little effect on the surface interactions. During the second annealing, a weight producing a small compressive stress was applied to hold the system compact and prevent the upper electrode from deforming upon heating. The compressive stress was found to favor the system to reach its equilibrium state with a completely parallel orientation, although the origin of this effect is not clearly known. Films of thicknesses $0.26\ \mu\text{m}$ (8 periods) and $0.86\ \mu\text{m}$ (27 periods) were prepared and measured. It was found that the film thickness plays a non-trivial role in determining the structure of the films.

In order to achieve a quantitative analysis of the internal structure of the films, neutron reflectivity, neutron diffuse scattering and neutron small-angle scattering methods were employed. The neutron scattering method is complementary to microscopy methods like TEM (transmission electron microscopy) or AFM (atomic force microscopy). Although not providing direct image information as obtained from microscopy methods (see for example [11, 13, 14, 15, 16, 64]), neutron scattering provides quantitative global statistical information about the structure. As demonstrated in our study, by fitting the reflectivity data using the software package Parratt32 we were able to determine the number of layers in the films which are parallel to the substrate. For films with a completely parallel orientation as well as those with a mixed orientation, the number of layers was estimated in this way. From the thickness of the part of the film with a perpendicular orientation in the electric-field-stabilized structure, the energy cost by the defect structures was estimated. By using small-angle scattering in transmission, the orientation distribution of the lamellae with preferentially perpendicular orientation in the middle of the film was determined. From diffuse scattering at small q_x , the lateral correlation length of the lamellar domains was obtained, and the power law behavior at large q_x was examined and compared with the theory.

From the combined results of neutron reflectivity and neutron small-angle scattering, we obtain:

- In the absence of an electric field, a complete alignment by the surface effects can be achieved in the thinner films after the first annealing. A mixed orientation

with boundary layers parallel and the central part partially perpendicular to the substrate was observed in the thicker films after the first annealing. This mixed orientation is a non-equilibrium and kinetically meta-stable structure. This state becomes unstable under a small compressive stress and will be converted into a completely parallel orientation (the equilibrium structure).

- In the presence of electric fields, the structure of the films is the result of competition between surface effects and electric field effects. In the thinner films where the surface effects are dominant throughout the film, the completely parallel orientation is maintained even if a field as strong as $40 \text{ V}/\mu\text{m}$ is applied. In the thicker films where the surface effects become less important in the middle of the film, the meta-stable mixed orientation observed after the first annealing can be stabilized by a field as strong as $40 \text{ V}/\mu\text{m}$. At a field below $\sim 20 \text{ V}/\mu\text{m}$, the completely parallel orientation induced by the compressive stress is maintained.
- A fully perpendicular orientation was never observed in our experiments. At the strongest field applied, only a mixed orientation with boundary layers parallel and the central part partially perpendicular to the substrate was observed. Defect structures must be formed at the boundaries between lamellar domains with different orientations. The energy cost of these defects is estimated from the strength of the field as about $3.5 \times 10^{-3} \text{ J}/\text{m}^2$.

From the results of neutron diffuse scattering, we obtain:

- Even in the films with a completely parallel orientation, the lamellar interfaces are not perfectly flat. The structure is most likely a mosaic one or it contains thermal fluctuations. An electric field induces an increase in the mosaicity of the structure or an enhancement of the thermal fluctuations, indicated by the increase in diffuse scattering intensity after the application of the electric field.
- From the diffuse scattering intensity at small q_x , the lateral correlation length of the mosaic structures or the thermal fluctuations is estimated as about $1\text{-}2 \mu\text{m}$. This correlation length remains as $1\text{-}2 \mu\text{m}$ after the application of an electric field, and does not depend on the strength of the field systematically. The diffuse scattering intensity does not depend on the field strength either. The diffuse scattering intensity at large q_x does not follow the power law behavior predicted by the Caillé's theory. The power law exponent found in our experiments is about 2, which is smaller than 4 predicted by the theory.
- From the diffuse scattering data in the $q_{x,i}$ -range we have measured, there seems an indication of the electric-field-induced structural undulations predicted by the Onuki's theory, but the $q_{x,i}$ -range is not large enough to make a clear statement upon this point.

However, there are still remaining questions which need to be done in the future. Firstly, a kinetically meta-stable state with a mixed orientation was observed in the thicker films after the first annealing. The state remains meta-stable even if the annealing time is prolonged to 168 h. The role of the kinetics in the structure formation is not clearly known. Secondly, it seems that a small compressive stress favors the system to reach its equilibrium state with a completely parallel orientation. The effects of this compressive stress are not exactly understood. The next step of the study would be to investigate the lamellar orientation by the electric field starting from an initial state

with a completely parallel orientation induced by a compressive stress. Thirdly, a clear statement on the existence of the electric-field-induced structural undulations predicted by the theory can still not be made from our experiments. To make it clear, a proper q_x -range has to be carefully selected, and improvements in the instrumental aspects will also be required.

Bibliography

- [1] T. P. Lodge, *Macromol. Chem. Phys.* **204**, 265 (2003).
- [2] M. Park, C. Harrison, P. M. Chaikin, R. A. Register and D. H. Adamson, *Science* **276**, 1401 (1997).
- [3] T. Thurn-Albrecht, J. Shotter, G. A. Kästle, N. Emley, T. Shibauchi, L. Krusin-Elbaum, K. Guarini, C. T. Black, M. T. Tuominen and T. P. Russell, *Science* **290**, 2126 (2000).
- [4] M. P. Stoykovich, M. Müller, S. O. Kim, H. H. Solak, E. W. Edwards, J. J. de Pablo and P. F. Nealey, *Science* **308**, 1442 (2005).
- [5] K. Amundson, E. Helfand, D. D. Davis, X. Quan, S. S. Patel and S. D. Smith, *Macromolecules* **24**, 6546 (1991).
- [6] K. Amundson and E. Helfand, *Macromolecules* **26**, 1324 (1993).
- [7] K. Amundson, E. Helfand, X. Quan and S. D. Smith, *Macromolecules* **26**, 2698 (1993).
- [8] K. Amundson, E. Helfand, X. Quan, S. D. Hudson and S. D. Smith, *Macromolecules* **27**, 6559 (1994).
- [9] T. Thurn-Albrecht, J. DeRouchey, T. P. Russell and H. M. Jaeger, *Macromolecules* **33**, 3250 (2000).
- [10] T. Thurn-Albrecht, J. DeRouchey, T. P. Russell and R. Kolb, *Macromolecules* **35**, 8106 (2002).
- [11] T. Xu, A. V. Zvelindovsky, G. J. A. Sevink, K. S. Lyakhova, H. Jinnai and T. P. Russell, *Macromolecules* **38**, 10788 (2005).
- [12] J. DeRouchey, T. Thurn-Albrecht and T. P. Russell, *Macromolecules* **37**, 2538 (2004).
- [13] T. Xu, C. J. Hawker and T. P. Russell, *Macromolecules* **36**, 6178 (2003).
- [14] T. Xu, J. T. Goldbach and T. P. Russell, *Macromolecules* **36**, 7296 (2003).
- [15] T. Xu, Y. Zhu, S. P. Gido and T. P. Russell, *Macromolecules* **37**, 2625 (2004).
- [16] J.-Y. Wang, T. Xu, J. M. Leiston-Belanger, S. Gupta and T. P. Russell, *Phys. Rev. Letts.* **96**, 128301 (2006).
- [17] A. Böker, A. Knoll, H. Elbs, V. Abetz, A. H. E. Müller and G. Krausch, *Macromolecules* **35**, 1319 (2002).

- [18] A. Böker, H. Elbs, H. Hänsel, A. Knoll, S. Ludwigs, H. Zettl, V. Urban, V. Abetz, A. H. E. Müller and G. Krausch, *Phys. Rev. Letts.* **89**, 135502 (2002).
- [19] A. Böker, V. Abetz, and G. Krausch, *Phys. Rev. Letts.* **90**, 049602 (2003).
- [20] A. Böker, H. Elbs, H. Hänsel, A. Knoll, S. Ludwigs, H. Zettl, A. V. Zvelindovsky, G. J. A. Sevink, V. Urban, V. Abetz, A. H. E. Müller and G. Krausch, *Macromolecules* **36**, 8078 (2003).
- [21] K. Schmidt, A. Böker, H. Zettl, F. Schubert, H. Hänsel, F. Fischer, T. M. Weiss, V. Abetz, A. V. Zvelindovsky, G. J. A. Sevink and G. Krausch, *Langmuir* **21**, 11974 (2005).
- [22] A. V. Zvelindovsky and G. J. A. Sevink, *Phys. Rev. Letts.* **90**, 049601 (2003).
- [23] P. Mansky, Y. Liu, E. Huang, T. P. Russell and C. Hawker, *Science* **275**, 1458 (1997).
- [24] L. Leibler, *Macromolecules* **13**, 1602 (1980).
- [25] F. S. Bates and G. H. Fredrickson, *Annu. Rev. Phys. Chem.* **41**, 525 (1990).
- [26] E. Helfand and Z. R. Wasserman, Microdomain structure and the interface in block copolymers, see ref [27], Vol. 1, p. 99 (1982).
- [27] I. Goodman, *Developments in block copolymers*, Applied Science, London, 1982.
- [28] E. Helfand, *Macromolecules* **8**, 552 (1975).
- [29] P. G. De Gennes, *J. Phys. (Paris)* **31**, 235 (1970).
- [30] T. P. Russell, *Curr. Opin. in Colloid & Int. Sci.*, **1**, 107 (1996).
- [31] E. Huang, P. Mansky, T. P. Russell, C. Harrison and P. M. Chaikin, R. A. Register, C. J. Hawker and J. Mays, *Macromolecules* **33**, 80 (2000).
- [32] C. M. Papadakis, P. Busch, D. Posselt and D.-M. Smilgies, *Adv. in Solid State Phys.* **44**, 327 (2004).
- [33] P. F. Green, T. M. Christensen, T. P. Russell and R. Jérôme, *Macromolecules* **22**, 2189 (1989).
- [34] J. D. Jackson, *Classical electrodynamics* (3rd edition), John Wiley & Sons, New York, 1999.
- [35] J. A. Osborn, *Phys. Rev.* **67**, 351 (1945).
- [36] G. G. Pereira and D. R. M. Williams, *Macromolecules* **32**, 8115 (1999).
- [37] P. G. De Gennes and J. Prost, *The Physics of Liquid Crystals*, Oxford University Press, 1993.
- [38] J. Als-Nielsen, J. D. Litster, R. J. Birgeneau, M. Kaplan, C. R. Safinya, A. Lindegaard-Andersen and S. Mathiesen, *Phys. Rev. B* **22**, 312 (1980).
- [39] J. Fukuda and A. Onuki, *J. Phys. II France* **5**, 1107 (1995).

- [40] A. Onuki and J. Fukuda, *Macromolecules* **28**, 8788 (1995).
- [41] Y. Tsori and D. Andelman, *Eur. Phys. J. E.* **5**, 605 (2001).
- [42] Y. Tsori and D. Andelman, *Macromolecules* **35**, 5161 (2002).
- [43] R.-J. Roe, *Methods of X-ray and Neutron Scattering in Polymer Science*, Oxford University Press, New York, 2000.
- [44] T. P. Russell, *Mat. Sci. Rep.* **5**, 171 (1990).
- [45] L. G. Parratt, *Phys. Rev.* **95**, 359 (1954).
- [46] J. Als-Nielsen and D. McMorrow, *Elements of Modern X-ray Physics*, John Wiley & Sons, New York, 2001.
- [47] S. K. Sinha, *J. Phys. III France* **4**, 1543 (1994).
- [48] S. K. Sinha, E. B. Sirota, S. Garoff and H. B. Stanley, *Phys. Rev. B* **38**, 2297 (1988).
- [49] F. Elsholz, *Rough surface characterization and determination of the rms roughness from coherent light scattering*, Technische Universität Berlin, April 2005.
- [50] J. Krim and J. O. Indekeu, *Phys. Rev. E* **48**, 1576 (1993).
- [51] R. Chiarello, V. Panella, J. Krim and C. Thompson, *Phys. Rev. Letts.* **67**, 3408 (1991).
- [52] J. A. Ogilvy and J. R. Foster, *J. Phys. D: Appl. Phys.* **22**, 1243 (1989).
- [53] Izrail S. Gradstejn and Iosif M. Ryzik, *Tables of series, products, and integrals*, Thun [u.a.] : Deutsch, 1981 (5th edition).
- [54] J. Brandrup and E. H. Immergut, *Polymer Handbook* (3rd edition), John Wiley & Sons, New York, 1989.
- [55] G. Strobl, *The Physics of Polymers*, Springer-Verlag Berlin Heidelberg, 1997.
- [56] K. Amundson, E. Helfand, S. S. Patel, X. Quan and S. D. Smith, *Macromolecules* **25**, 1935 (1992).
- [57] G. Coulon, T. P. Russell, V. R. Deline and P. F. Green, *Macromolecules* **22**, 2581 (1989).
- [58] E. Schäffer, T. Thurn-Albrecht, T. P. Russell and U. Steiner, *Nature* **403**, 874 (2000).
- [59] D. Clemens, *Physica B* **221**, 507 (1996).
- [60] A. A. van Well and H. Fredrikze, *Physica B* **357**, 204 (2005).
- [61] C. Münster, T. Salditt, M. Vogel, R. Siebrecht and J. Peisl, *Europhys. Letts.* **46**, 486 (1999).
- [62] S. H. Anastasiadis, T. P. Russell, S. K. Satija and C. F. Majkrzak, *Phys. Rev. Letts.* **62**, 1852 (1989).

- [63] P. Mansky, T. P. Russell, C. J. Hawker, J. Mays, D. C. Cook and S. K. Satija, *Phys. Rev. Letts.* **79**, 237 (1997).
- [64] T. Xu, C. J. Hawker and T. P. Russell, *Macromolecules* **38**, 2802 (2005).
- [65] S. P. Gido and E. L. Thomas, *Macromolecules* **27**, 6137 (1994).
- [66] E. Burgaz and S. P. Gido, *Macromolecules* **33**, 8739 (2000).
- [67] I. W. Hamley, *The Physics of Block Copolymers*, Oxford University Press, 1998.
- [68] D. E. Angelescu, J. H. Waller, D. H. Adamson, P. Deshpande, S. Y. Chou, R. A. Register and P. M. Chaikin, *Adv. Mater.* **16**, 1736 (2004).
- [69] D. E. Angelescu, J. H. Waller, R. A. Register and P. M. Chaikin, *Adv. Mater.* **17**, 1878 (2005).
- [70] L. J. Fetters, D. J. Lohse, D. Richter, T. A. Witten and A. Zirkel, *Macromolecules* **27**, 4639 (1994).
- [71] T. P. Russell, R. P. Hjelm, Jr. and P. A. Seeger, *Macromolecules* **23**, 890 (1990).
- [72] Y. Yoneda, *Phys. Rev.* **131**, 2010 (1963).
- [73] P. Štěpánek, F. Nallet and K. Almdal, *Macromolecules* **34**, 1090 (2001).
- [74] P. Štěpánek, F. Nallet, O. Diat, K. Almdal and P. Panine, *Macromolecules* **35**, 7287 (2002).
- [75] T. Salditt, C. Münster, J. Lu, M. Vogel, W. Fenzl and A. Souvorov, *Phys. Rev. E* **60**, 7285 (1999).
- [76] T. Salditt, M. Vogel and W. Fenzl, *Phys. Rev. Letts.* **90**, 178101 (2003).

Acknowledgements

Many thanks to my supervisor, Prof. Thomas Thurn-Albrecht. He has led me into the fascinating research field of block copolymers. I would not be able to finish this thesis without his guidance and many useful discussions with him.

Thanks to my collaborators in the Paul-Scherrer-Institute for their help in establishing the instrumental settings for our experiments. They are Dr. Thomas Gutberlet (for AMOR) and Dr. Mukul Gupta (for AMOR), Dr. Jochen Stahn (for MORPHEUS and AMOR), and Dr. Thomas Geue (for SANS-II).

Thanks to Ilja Gunkel for his assistance and cooperation in some of the experiments.

Thanks to my former colleagues in the Physics Department of University of Freiburg, for their friendship and help during the first year of my Ph. D.

Heartful thanks to my colleagues in the Polymer Group, Physics Department of Martin-Luther-University of Halle. They are Dr. Klaus Schröter, Dr. Elke Hempel, PD Dr. Mario Beiner, Mrs. Katrin Herfurt, the students including Peter Kohn (PhD), Gopalakrishnan Trichy R. (PhD), Nitin Shingne (PhD), Albrecht Petzold (Diplom), Thomas Henze (Diplom) and Daniel Neumann (Diplom). I would also like to thank the Huggers, Stefan and Tsvety Hugger (former group members). All these colleagues have provided me a constant friendship and help (especially from Dr. Schröter) in my work. The former and present secretariats Ms. Christiane Helmdorf and Mrs. Aline Leuchtenberger also gave me a lot of help in administrative events.

Eidesstattliche Erklärung

Ich erkläre hiermit, dass ich keine anderen als die von mir angegebenen Quellen und Hilfsmittel zur Erstellung meiner Dissertation verwendet habe. Den benutzten Werken wörtlich oder inhaltlich entnommene Stellen sind als solche gekennzeichnet.

Xiuli Jiang

Halle (Saale), Oktober 2006

Curriculum vitae

First Name	Xiuli
Family Name	Jiang
Date of Birth	May 15, 1977
Place of Birth	Jilin, China
Nationality	P. R. China
E-mail	jxl_marie@yahoo.com

EDUCATION

Sep. 1995 - Jul. 1999	Bachelor of Science Department of Macromolecular science Fudan University (Shanghai, China)
Sep. 1999 - Jul. 2002	Master of Science Department of Macromolecular science Fudan University (Shanghai, China)
Oct. 2002 - Feb. 2004	Ph. D in Physikalisches Institut Albert-Ludwigs-Universität Freiburg (Supervised by Prof. Thomas Thurn-Albrecht)
Since Feb. 2004	Ph. D in Institut für Physik Martin-Luther-Universität Halle-Wittenberg (Supervised by Prof. Thomas Thurn-Albrecht)
